**A STUDY IN SCAR20 NEUROLOGIC DISORDER REVEALS DEFECTIVE**

**CELLULAR LIPID HOMEOSTASIS**

APPROVED BY SUPERVISORY COMMITTEE

Mike Henne, Ph.D. (Supervisor)

Joel Goodman, Ph.D. (Chair)

Sandra Schmid, Ph.D.

Russell Debose-Boyd, Ph.D.

DEDICATION


I would like to thank my parents, Manashi Dutta and Subir Datta,

my fiancée, Deep Chatterjee,

and my mentor, Mike Henne

**A STUDY IN SCAR20 NEUROLOGIC DISORDER REVEALS DEFECTIVE**

**CELLULAR LIPID HOMEOSTASIS**

by

SANCHARI DATTA

DISSERTATION

Presented to the Faculty of the Graduate School of Biomedical Sciences

The University of Texas Southwestern Medical Center at Dallas

In Partial Fulfillment of the Requirements

For the Degree of

DOCTOR OF PHILOSOPHY

The University of Texas Southwestern Medical Center at Dallas

Dallas, Texas

December, 2020

A STUDY IN SCAR20 NEUROLOGIC DISORDER REVEALS DEFECTIVE CELLULAR

LIPID HOMEOSTASIS


Sanchari Datta

The University of Texas Southwestern Medical Center at Dallas, 2020


Supervising Professor: Mike Henne, Ph.D.

## PREFACE

Fatty acids (FAs) are important cellular metabolites which are utilized by the cells to perform important functions such as the generation of ATP, membrane biosynthesis, and cell signaling. Dysregulation in FA processing and storage causes toxic FA accumulation which alters membrane compositions and contributes to metabolic and neurological disorders. Excess lipids are stored as lipid droplets (LDs) which sequester toxic FAs and serve as metabolic buffers to maintain lipid and energy homeostasis. LDs emerge from the endoplasmic reticulum (ER) but how their formation is regulated is not completely understood. Recently, we identified sorting nexin family protein Snx14, implicated in cerebellar ataxia disease SCAR20, as a novel factor which enriches at ER-LD contacts following exogenous FA treatment independently of Seipin and promotes FA-induced LD growth. Loss of Snx14 perturbs LD morphology whereas Snx14 overexpression extends ER-LD contacts and promotes LD biogenesis. Proximity-based APEX2 labeling revealed the enrichment of Snx14 at ER-LD contacts during LD biogenesis.

Capitalizing on this APEX technology, we also utilize Snx14-APEX2 localization to dissect the protein composition of ER-LD contact sites. We identify proteins involved in fatty acid activation, desaturation, and triacylglycerol synthesis as being enriched at ER-LD contacts, indicating these contact sites serve as lipogenic sub-domains of the ER network. Furthermore, we identify the major delta-9 FA desaturase SCD1 as a key interacting partner of Snx14. Consistent with this, Snx14-deficient cells are hypersensitive to saturated fatty acid (SFA)-mediated lipotoxic cell death that compromises ER integrity. We show that SCD1 is upregulated in *SNX14-KO* cells, and Snx14-associated SFA hypersensitivity can be rescued by ectopic SCD1 overexpression. The lipid-associated PXA domain of Snx14 and its interaction with SCD1 are required for Snx14-mediated SFA protection function. Snx14 loss mimics SCD1 inhibition and causes accumulation of free FAs and increased membrane lipid saturation. Altogether these mechanistic insights reveal a role for ER-LD contacts as lipogenic ER sub-domains, and Snx14 as an ER-LD tether with a key role in maintaining cellular FA homeostasis through a functional interaction with SCD1, defects in which may underlie the neuropathology of SCAR20.

# ACKNOWLEDGEMENTS

*'I ought to know by this time that when a fact appears to be opposed to a long train of deductions it invariably proves to be capable of bearing some other interpretation ~ Sherlock Holmes'*

*-Sir Arthur Conan Doyle, A Study in Scarlet*

# TABLE OF CONTENTS

# PRIOR PUBLICATIONS

Datta, S., Bowerman, J., Hariri, H., Ugrankar, R., Eckert, K.M., Corley, C., Vale, G., McDonald, J.G. and W. M. Henne. 2020. 'Snx14 proximity labeling reveals a role in saturated fatty acid metabolism and ER homeostasis defective in SCAR20 disease', *bioRxiv*. doi: https://doi.org/10.1101/2020.05.31.126441 (Accepted for publication in *PNAS*)

Datta, S., Y. Liu, H. Hariri, J. Bowerman, and W. M. Henne. 2019. 'Cerebellar ataxia disease-associated Snx14 promotes lipid droplet growth at ER-droplet contacts', *J Cell Biol*, 218: 1335-51.

Bryant, D., Y. Liu, S. Datta, H. Hariri, M. Seda, G. Anderson, E. Peskett, C. Demetriou, S. Sousa, D. Jenkins, P. Clayton, M. Bitner-Glindzicz, G. E. Moore, W. M. Henne, and P. Stanier. 2018. 'SNX14 mutations affect endoplasmic reticulum-associated neutral lipid metabolism in autosomal recessive spinocerebellar ataxia 20', *Hum Mol Genet*, 27: 1927-40.

Bryant, D., M. Seda, E. Peskett, C. Maurer, G. Pomeranz, M. Ghosh, T. A. Hawkins, J. Cleak, S. Datta, H. Hariri, K. M. Eckert, D. J. Jafree, C. Walsh, C. Demetriou, M. Ishida, C. Aleman-Charlet, L. Vestito, R. Seselgyte, J. G. McDonald, M. Bitner-Glindzicz, M. Hemberger, J. Rihel, L. Teboul, W. M. Henne, D. Jenkins, G. E. Moore, and P. Stanier. 2020. 'Diverse species-specific phenotypic consequences of loss of function sorting nexin 14 mutations', *Sci Rep*, 10: 13763.

Hariri, H., N. Speer, J. Bowerman, S. Rogers, G. Fu, E. Reetz, S. Datta, J. R. Feathers, R. Ugrankar, D. Nicastro, and W. M. Henne. 2019. 'Mdm1 maintains endoplasmic reticulum homeostasis by spatially regulating lipid droplet biogenesis', *J Cell Biol*, 218: 1319-34.

Ugrankar, R., J. Bowerman, H. Hariri, M. Chandra, K. Chen, M. F. Bossanyi, S. Datta, S. Rogers, K. M. Eckert, G. Vale, A. Victoria, J. Fresquez, J. G. McDonald, S. Jean, B. M. Collins, and W. M. Henne. 2019. '*Drosophila* Snazarus Regulates a Lipid Droplet Population at Plasma Membrane-Droplet Contacts in Adipocytes', *Dev Cell*, 50: 557-72 e5.

Chandra, M., Y. K. Chin, C. Mas, J. R. Feathers, B. Paul, S. Datta, K. E. Chen, X. Jia, Z. Yang, S. J. Norwood, B. Mohanty, A. Bugarcic, R. D. Teasdale, W. M. Henne, M. Mobli, and B. M. Collins. 2019. 'Classification of the human phox homology (PX) domains based on their phosphoinositide binding specificities', *Nat Commun*, 10: 1528.

# LIST OF FIGURES

# LIST OF SUPPLEMENTARY FIGURES

# LIST OF APPENDICES

xx

# LIST OF DEFINITIONS

ER                              Endoplasmic Reticulum

LD                              Lipid droplet

Snx                             Sorting nexin

FA                              Fatty acid

FFA                             Free Fatty acid

OA                              Oleic acid / Oleate

TAG.                            Triacylglycerol

DAG                             Diacylglycerol

ACSL                            Acyl-CoA Synthetase Long Chain Family Member

DGAT                            DAG O-acyltransferase

FATP                            Fatty Acid Transport Protein

NVJ                             Nuclear ER-Vacuole junction

SCAR                            Spinocerebellar Ataxia Autosomal Recessive

APEX                            Ascorbate peroxidase

TEM                             Transmission electron microscopy

DAB                             Diaminobenzidine

EGFP                            Enhanced green fluorescent protein

$H_2O_2$                        Hydrogen peroxide

WT                              Wildtype

AHs                             Amphipathic helices

KO                              Knockout

| | |
|---|---|
| MDH | Monodansylpentane |
| TLC | Thin layer chromatography |
| O/E | Overexpressed |
| UPR | unfolded protein response |
| NBD | N-[(7-nitro-2-1,3-benzoxadiazol-4-yl)-methyl]amino |
| siRNA | small interfering RNA |
| Snz | Snazarus |
| PX | Phox homology |
| PI3P. | Phosphatidylinositol 3-phosphate |
| SCD1 | Stearoyl-CoA desaturase 1 |
| SFA | Saturated fatty acid |
| MUFA | Mono-unsaturated fatty acid |
| MS | Mass Spectrometry |

# CHAPTER ONE

## Introduction

**Background and Significance**

Lipids are major energy yielding biomolecules which are also utilized to provide structural integrity to our organs, tissues, cells and organelles. In addition, lipids co-ordinate signal transmission in response to changing environmental conditions. Almost 5% of all human genes contribute towards lipid synthesis, underscoring lipids role in cellular function. The human body generates thousands of complex lipid species, usually composed of a backbone of one or more fatty acids (FAs). The production of these FAs and their complex lipid derivatives involves highly regulated multi-step reactions. Ultimately, the combinations of these complex lipids in specific proportions constitutes the lipid bilayer of cellular organelles in eukaryotes.

Based on their FA structure and head group, acyl chain-containing complex lipids can be divided into the following major lipid classes: sterol lipids, sphingolipids, phospholipids, and neutral lipids. Lipids are either derived from the diet or are *de novo* synthesized intracellularly. Lipid biosynthesis occurs primarily in the most extensive cellular organelle, the endoplasmic reticulum (ER) which is the primary anabolic organelle of eukaryotes. Apart from providing membrane identity and integrity, lipids are utilized by other organelles for many important cellular functions including energy production via FA oxidation in mitochondria and peroxisomes, lipid recycling in the lysosomes and vesicular trafficking by the Golgi apparatus. Lipids also perform signaling roles and co-ordinate information flow from the cellular exterior to the interior and between the organelles to respond to changing environmental cues. How do the cells manage excess lipids when exposed to nutrients overload? Studies (Walther, Chung, and Farese 2017; Jarc and Petan 2019; Pol, Gross, and Parton 2014; Henne, Reese, and Goodman 2019) have shown that cells are equipped with the ability to convert excess lipids into neutral lipids which are packaged and stored as future energy reserves into specialized cytoplasmic organelles called lipid droplets (LDs). Under nutrient deficiencies, how cells signal to strategically utilize their lipid stores for energy, and to maintain organelle lipid composition and membrane identity, is still extensively studied. Recent

research shows spatial organization of lipid synthesis enzymes and associated factors, vesicular and non-vesicular modes of lipid transport, cell signaling, and regulation of lipid metabolizing genes all as major contributors of organelle lipid homeostasis. Regulation of each step of lipid processing, transport and utilization is crucial for cellular and organismal health. Genetic mutations associated with defective lipid metabolism can cause aberrant accumulation of cytotoxic species – a phenomenon known as lipotoxicity which underlie the cause of many metabolic disorders, cardiovascular diseases, and neurological diseases (Ertunc and Hotamisligil 2016; Schaffer 2016).

My research investigates the mechanisms underlying the cause of the autosomal recessive neuropathology SCAR20, which is associated with loss-of-function mutations in the gene encoding a sorting nexin family protein called Snx14. In an attempt to understand whether Snx14 functions in lipid metabolism to maintain neuronal homeostasis, this brief introductory review of literature provides background on recent developments and the understanding in the field of FA processing in the context of human neurological disorders as well as on Snx14 and its role in SCAR20 disease. Based on the emerging knowledge, we collectively propose that Snx14 functions as a scaffold in the ER network that spatially organizes lipid metabolic reactions to promote LD and FA homeostasis. My studies provide evidence on the mechanisms by which Snx14 maintains ER lipid homeostasis necessary for cellular and neuronal health.

**Lipid synthesis and transport**

*Free Fatty Acids (FFAs) synthesis and transport*

As the brain is highly enriched with lipids like many other organs such as liver, heart and adipose tissue, it is important to understand the source of lipids and the nature of their intracellular distribution. A common constituent of many acyl lipids is the free fatty acid (FFA) which is a hydrocarbon tail attached to a carboxyl group (-COOH) at one end. *De novo* FFA synthesis occurs when acetyl-CoA acquired from glucose metabolism or other sources is first converted into malonyl-CoA by acetyl-CoA carboxylases (Wakil, Stoops, and Joshi 1983), both of which then serve as substrates to the FAS (fatty acid synthase) complex (Chirala et al. 2001; Smith 1994). The

majority of FAs are derived from the diet, which either passively diffuses through the cell membrane or are transported by FATPs (fatty acid transport proteins), FA translocase, FABPs (FA binding proteins), or caveolae at the plasma membrane (PM) (Mitchell and Hatch 2011). Following internalization, FAs are metabolized into complex lipid species.

*Phospholipid synthesis and transport*

Among the FA-derived complex lipids, phospholipids mainly form building blocks of cellular membranes. The glycerophospholipids are amphipathic molecules formed of a FA tail with a phosphate group and a hydrophilic head group which can include choline, ethanolamine, serine, inositol or glycerol group conjugated to a glycerol backbone. Phosphatidylcholine (PC) and phosphatidylethanolamine (PE) are synthesized via collaboration between the ER and mitochondria primarily by the Kennedy pathway (Kennedy and Weiss 1956; Wright and McMaster 2002) which is further used to synthesize phosphatidylserine (PS) (Kuge, Nishijima, and Akamatsu 1986). Similarly, phosphatidylinositol (PI) (Antonsson 1997; Kim, Guzman-Hernandez, and Balla 2011), phosphatidylglycerol (PG) (Kawasaki et al. 1999; Kawasaki and Nishijima 2003) and cardiolipin synthesis (Schlame, Brody, and Hostetler 1993) occurs by ER-resident enzymes. Based on their structure and amphipathic nature, phospholipids are trafficked following their synthesis, to specific organelles where they help define the organelle's membrane architecture (Vance 2015). For example, PC and PI largely localize at the ER whereas PS, PG and PE localize to mitochondria and its associated membranes. A few characterized soluble transfer proteins that enable this lipid trafficking are well defined. These include the phosphatidylcholine specific transfer protein (PCTP) (Kanno et al. 2007), and phosphatidylinositol transfer protein (PITP) (Helmkamp et al. 1974).

While vesicular modes of lipid transport, such as mediated by COPII vesicles from the ER, are well established, lipid flux still occurs in the absence of vesicular trafficking (Vance 2015). This can be explained by an alternative form of transport, the non-vesicular mode of inter-organelle crosstalk mediated by molecular tethers (Levine and Loewen 2006; Elbaz and Schuldiner 2011). Some examples of such tethers are PI transfer protein (PITP) and Nir2 at ER-PM contact sites,

oxysterol binding protein (OSBP) related proteins 5 and 8 (ORP5/8) which mediates PS exchange, or mitochondria associated membranes (MAMs) at ER-mitochondria contact sites. This non-vesicular transport mechanism will be elaborated further in the latter part of this dissertation's discussion.

*Cholesterol synthesis and transport*

The brain is particularly rich in cholesterol which provides neuronal insulation important for rapid electronic signal transduction. The sterol moiety in steryl lipids is usually cholesterol in mammals and is primarily synthesized in the liver (Bloch 1965; Blom, Somerharju, and Ikonen 2011). Cholesterol is amphipathic and consists of a hydroxylated tetracyclic ring attached to a hydrocarbon tail. Intracellular biosynthesis of cholesterol occurs at the ER by a multi-step complex reaction pathway, called the mevalonate pathway in which acetyl-CoA is the starting substrate, and the rate-limiting reaction is the conversion of HMG-CoA to mevalonate by HMG-CoA reductase (Bloch 1965; Ye and DeBose-Boyd 2011; Langdon and Bloch 1953). From cholesterol, steroid hormones, bile acid and vitamin D are produced. Cholesterol can also be derived from diet and is transported in the form of Low Density Lipoproteins (LDLs) (Segrest et al. 2001) from the liver to other peripheral tissues including the central nervous system (CNS). Binding to plasma membrane receptors leads to LDL endocytosis, which subsequently gets delivered to the endo-lysosomal system via vesicular trafficking (Brown and Goldstein 1986). Following its liberation from LDL particles by the lysosome, cholesterol is delivered to plasma membrane, mitochondria and ER, but how the sterol is transported to these different destinations is still not clear. Previous studies proposed the role of non-vesicular transport proteins such as sterol carrier protein (SCP-2) (Puglielli et al. 1995; Gallegos et al. 2001), oxysterol binding protein (ORPs) (Zhao and Ridgway 2017) and steroidogenic acute regulatory protein-related lipid transfer (START) family proteins (Gatta et al. 2015) in sterol transport pathways. At the ER, the cholesterol level is highly controlled and maintained at ~5 mol% (Brown and Goldstein 2009). The excess cholesterol can be either recycled to other organelles or esterified and stored in LDs as cholesterol-esters (CE) (Chang et al. 2009).

*Sphingolipid synthesis and transport*

Another lipid class called the sphingolipids are formed of a FA chain attached to a sphingosine backbone. Sphingolipid species can vary depending on long chain base modifications, branching, and hydroxyl group additions. Ceramides, sphingomyelins, and glycosphingolipids are some common forms of sphingolipids. Initially synthesized as ceramide at the ER, ceramide is transported to the Golgi and further matured, then ultimately delivered to the plasma membrane (Tidhar and Futerman 2013) where it is known to provide membrane stability and resistance to toxic environments, as well as act as cell signaling mediators. A well characterized sphingolipid/ceramide transport protein is the ceramide transfer protein (CERT) which is known to transport ceramides from ER to Golgi in an ATP-dependent manner (Hanada et al. 2003). Additionally, FAPP2 mediated transport (D'Angelo et al. 2013) and vesicular transport of sphingolipids, though not well defined, is also shown to exist.


*Triacylglycerol (TAG) synthesis and transport*

The storage lipids are the neutral lipids which mainly consist of triacylglycerol (TAG). Mainly synthesized by the adipose tissue and liver, the skeletal muscles, heart, and brain can also induce TAG formation. TAGs are a very high source of energy for cells, as consumption of one TAG molecule generates ~400 ATP molecules. Structurally, these hydrophobic TAG molecules are comprised of 3 fatty acyl chains conjugated to a glycerol backbone and are synthesized at the ER by a stepwise process. To form TAG, glycerol-3-phosphate (G3P) derived from glucose undergoes the following consecutive reactions (Lehner and Kuksis 1996; Weiss, Kennedy, and Kiyasu 1960; Coleman and Lee 2004) – G3P is converted to lysophosphatidic acid (LPA) and phosphatidic acid (PA) sequentially by G3P acyltransferase (GPAT) and 1-acylglycerol-3-phosphate acyltransferase (AGPAT), which involves addition of two successive FA chains to the glycerol phosphate backbone. Then PA is dephosphorylated by phosphatidic acid phosphatase (PAP) to form 1,2-diacylglycerol (DAG). Finally, another FA chain is added to DAG by diacylglycerol acyltransferase (DGAT) to form TAG.

The TAGs along with CEs are packaged together at the ER to the core of the lipid droplets (LDs) which bud from the cytosolic leaflets of the ER (Walther, Chung, and Farese 2017). As LDs store high energy-yielding lipids such as TAG, these organelles form the cellular energy reservoir. Besides their primary job as energy storage organelles, LDs maintain lipid homeostasis and promote organismal health. These important cellular functions of LDs have only recently been recognized and discussed in detail in the later part of this chapter.

**ER homeostasis in neuronal health and disease**

*Lipid synthesis in ER homeostasis*

The cell's lipid metabolic reactions primarily occur in the ER as it houses most of the lipid metabolic enzymes, the functions of which are highly co-ordinated to maintain a balance between levels of complex lipids. ER network organization and structure are also largely determined by the fatty acyl chain composition of its lipids, but how the cell maintains ER lipid homeostasis still remains under-explored. Fatty acyl structure involving its chain length and saturation degree influence the ordering pattern and fluidity of the ER membrane. These properties can be regulated by ER resident enzymes such as the elongases and desaturases. Specifically, members of the elongation of very long chain FAs (Elovl) (Guillou et al. 2010; Jump 2009) protein family regulate FA elongation, and desaturases such as stearoyl-CoA desaturase (SCD1/2) (Paton and Ntambi 2009) introduce one double bond in a saturated FA (SFA) to convert it into a mono-unsaturated FA (MUFA). Other desaturases such as the FA desaturase (FADS1/2) introduces multiple double bonds in the hydrocarbon chain to form polyunsaturated FAs (PUFAs) (Glaser, Heinrich, and Koletzko 2010; Ralston et al. 2015).

Saturated FAs (SFAs) are well-known to be toxic to cells for several reasons. When cells are exposed to excessive saturated FFAs such as palmitate, glycerophospholipid production is upregulated, leading to increased incorporation of SFAs into diacyl phospholipids (Piccolis et al. 2019) and affecting TAG or LD synthesis (Listenberger et al. 2003; Lee et al. 2010). This lipid saturation imbalance can induce membrane solidification and stiffening, causing ER stress (Borradaile, Harp, and Schaffer 2006; Borradaile et al. 2006b; Ariyama et al. 2010). Palmitate also

induces production of ceramides (Turpin et al. 2006) and reactive oxygen species (Gao et al. 2010), all of which together contributes to cellular lipotoxicity. High concentration of SFAs has been implicated in insulin resistance (Xiao et al. 2006) and many metabolic disorders such as diabetes (Hu, van Dam, and Liu 2001) and coronary heart disease (Wang, Folsom, and Eckfeldt 2003). Similarly, the ER cholesterol level also impacts membrane properties by rendering a strong ordered phase formation through its hydrophobic interaction with phospholipid FAs (Fu, Watkins, and Hotamisligil 2012), and hence its level in the ER is highly controlled by the SCAP/SREBP pathway (Brown and Goldstein 2009). As a response to cope with ER stress and elevated lipid levels, cells produce LDs which can scavenge toxic lipid species and ultimately protect the ER membrane by sequestering the lipids (Olzmann and Carvalho 2019). However, with increases in LD formation, there is a proportional increase in PC synthesis, which is the major component of the LD phospholipid monolayer (Krahmer et al. 2011). This disrupts the phospholipid balance, particularly the PC/PE ratio, which can further contribute to metabolic dysfunction and ER stress. The imbalance in PC/PE ratio or even increases in cholesterol level is tightly linked to the Sarco/Endoplasmic Reticulum calcium ATPase protein (SERCA) function in maintaining calcium homeostasis at the ER that can affect downstream chaperone activity and induce ER stress (Fu et al. 2011).

*Protein synthesis in ER homeostasis*

Given that the ER is involved in both *de novo* protein and lipid synthesis, lipid dysregulation can be either the cause or consequence of perturbed protein homeostasis, which together can contribute to ER-associated dysfunction, linked to a myriad of neurological disorders. The ER is a highly dynamic organelle which continuously changes its structure and volume to adapt to cellular stresses induced by changing environmental conditions. As such, alterations in ER membrane shape, protein misfolding and aggregation contribute towards ER stress as a response to which UPR is activated. Failure to cope with ER stress is associated with various neurodegenerative disorders. For example, patients with hereditary spastic paraplegia (HSP), which compromises motor neuron integrity, are characterized by loss of function mutations in ER tubule regulators such as atlastin-1 (SPG3A), spastin (SPG4) or REEP1(SPG31). Reticulons and Lunapark are other

proteins which induce membrane curvature and determine membrane shape. This list of ER tubule forming regulators also include Rab GTPases (Rab10 and Rab 18) the mutations of which cause neuronal differentiation defects affecting brain functions. Another process that is required to maintain ER homeostasis is autophagosomal degradation of ER membranes, called ER-phagy, and is facilitated by ER membrane proteins FAM134B or Rtn3 which are linked to neuropathies such as hereditary sensory and autonomic neuropathies (HSAN). Reduced syntaxin expression perturbs vesicle transport and ER network organization. Vesicle-associated VAPB overexpression causes aggregation in the ER and Golgi fragmentation, and is associated with neurodegeneration (Yamanaka and Nukina 2018). These are some examples of ER-associated proteins that can disrupt ER function and overall cellular homeostasis. Such ER dysregulation can also be caused by changes in membrane lipid composition or aberrant accumulation of toxic lipids which in turn can cause ER protein misfolding and aggregation. On the other hand, ER stress can be associated with generation of toxic lipid species which further affects ER function resulting in a feedback loop, ultimately inducing cellular death. Thus, the integrity and proper functioning of the ER, the most extensive organelle and source of *de novo* synthesis of lipids and proteins, is very important for neuronal health.

**Lipid flux via inter-organelle contacts**

Besides the need for maintenance of the ER lipidome and proteome for cell homeostasis, *information exchange* between the ER and other cellular organelles also has to be highly coordinated for overall cellular and organismal homeostasis. As each organelle is demarcated by a unique lipid bilayer composition and equipped with performing unique metabolic reactions, organelles should communicate with each other to respond to changing environmental cues. Part of this inter-organelle communication can be achieved by classical vesicular trafficking which is well characterized. However, the timescale of this vesicular transport differs significantly from the rapid exchange of metabolites, such as PE and PC exchange among organelles(Vance 2015), suggesting the existence of alternative non-vesicular modes of transport. This non-vesicular transport is also indicated by sterol transport occurring between ER and PM (Baumann et al. 2005).

The vast extension of the ER allows it to communicate with other cellular organelles such as mitochondria, Golgi, lysosomes by creating zones of contact which enable crosstalk important for lipid trafficking, cell signaling, and ion transport. These physical contacts are called membrane contact sites (MCSs), where the membranes between organelles are closely apposed and tethered by multiprotein complexes, but do not undergo fusion. Such appositions were observed much earlier in the 1950's in electron micrographs by George Palade and Keith Porter, but whether these contacts were simply an artifact of the crowded cellular environment or bore functional relevance was, at the time, unknown. Since MCSs contains compact spaces linking organelles, enzymes can facilitate concentrating substrates here and new products synthesized can be rapidly trafficked and utilized by the acceptor organelles. Thus, these MCSs form hubs of organizing lipid metabolism. Interestingly, many MCSs are dynamic in nature as the protein and lipid compositions at these sites continuously change based on cellular conditions like nutrient availability (Bohnert 2020). The ER-PM MCS (Saheki and De Camilli 2017)is the most characterized contact site with roles in lipid exchange such as between PM-derived PI4P and ER-derived PS by Osh/ Sac1/ VAP (Lev et al. 2008; Raychaudhuri et al. 2006), or calcium signaling by STIM1 (Liou et al. 2007) and Esyts (Giordano et al. 2013).

**Inter-organelle contacts in yeast**

Yeast has been an important genetic and visual model system to study inter-organelle contacts due to its simplified organelle architecture and conservation of mammalian transport mechanisms. Usually there is one lysosome in yeast called the vacuole which forms a singular large contact with the ER surrounding the nucleus, denoted as the nuclear ER. This MCS in yeast is called the nucleus-vacuole junction (NVJ), which has been extensively studied since its first observation in 2000 (Pan et al. 2000). The first molecular tether identified at the NVJ is the heterodimer between the ER resident NVJ1 and Vac8, localized on the vacuole surface. Although the NVJ is a stable structure, under nutrient stress it can expand and simultaneously undergo changes in protein and lipid composition. NVJ expansion is due to the transcriptionally regulated increase in the NVJ1-Vac8 protein complex, which enriches at the nucleus-vacuole junction as a circular disc. Lipid metabolism is also spatially reorganized at the NVJ, as LDs are observed to bud and cluster along

the edges of the NVJ when yeast transition into stationary phase growth, a phase of its life cycle associated with upregulated LD biogenesis.

There are several inter-organelle tethers and enzymes that localize to the NVJ and co-ordinate lipid metabolism at this site. Recently, the LD budding at the NVJ is defined by the molecular tether Mdm1 (Hariri et al. 2018). Moreover, under nutrient starvation, many proteins are recruited to the NVJ which include PA synthesis enzyme Pah1(Barbosa et al. 2015), ceramide synthesis enzyme Tsc13 (Kohlwein et al. 2001), sterol synthesis enzymes HMG1 and HMG2, and the lipid transport proteins (LTPs) Osh1, Nvj2, Vps13, and Lam6 (Bohnert 2020). Most of these LTPs possess a hydrophobic cavity, such as the synaptotagmin-like mitochondrial lipid binding protein (SMP) domain in Nvj2 (Toulmay and Prinz 2012). There is also a sterol-binding StART domain in Lam6 (Elbaz-Alon et al. 2015), and a hydrophobic tunnel domain in Vps13 (Kumar et al. 2018). All these domains have the potential of binding lipids and shuttling them between two closely apposed membranes, though the mechanism still needs to be further dissected.

Some of these MCS proteins re-localize at other contact sites under different metabolic stresses, an example of how different MCSs cross communicate. Vps13 localizes at NVJ under nonfermentable carbon sources and relocalizes to the vacuole-mitochondria tether vClamp in the presence of glucose. Different MCSs can change in response to other MCSs. For example, when proteins of the ERMES complex at ER-Mitochondria contacts are deleted, the vClamp contact site expands and recruits Vps13 and Lam6 to maintain cell viability (Lang et al. 2015; Murley et al. 2015). The ER resident protein Nvj2 localizes at NVJ upon glucose depletion and localizes at ER-Golgi contacts under ER stress and upregulated ceramide synthesis to facilitate ceramide export from the ER (Liu et al. 2017). Similarly, Osh1 is also found at both NVJ and ER-Golgi sites under active cell division (Levine and Munro 2001).

**Mammalian inter-organelle contacts in neurodegeneration**

As cells of SCAR20 patients suffering from cerebellar ataxia contain perturbed lysosome structures, we hypothesized that ER-lysosome crosstalk similar to yeast might be important to

maintain lysosome integrity. However, there are no Nvj1 or Vac8 homologs in mammals, and unlike the single distinct stable ER-vacuole/lysosome junction NVJ in yeast, ER-endosome/lysosome contacts in mammalian cells are highly dynamic and short-lived (Friedman et al. 2013). However, many other yeast MCS proteins are conserved in mammals, and there exists evidence that they play roles in lipid exchange and lipid metabolism. The yeast Vps13 has four homologs in humans Vps13A-D, among which three are associated with progressive neurodegeneration associated with muscle dystonia, developmental delay, and epilepsy. Vps13A is implicated in chorea-acanthocytosis (CHAC), Vps13B in Cohen syndrome (COH) and VPS13C in Parkinson's Disease (Ueno et al. 2001; Kondo et al. 2005; Lesage et al. 2016). Vps13A localizes at ER-mitochondria contacts, Vps13C at ER-late endosome/lysosome contacts, and both are also found at ER-LDs interfaces. Recent studies proposed the existence of a hydrophobic cavity at the N-terminal region of Vps13 which solubilizes and transport glycerolipids between membranes, defects in which causes toxic lipid accumulation (Kumar et al. 2018). Another ER-resident protein is protrudin, containing a PI3P binding FYVE domain that tethers the ER to lysosomes in mammals and mediates endosomal positioning based on sterol availability (Raiborg, Wenzel, and Stenmark 2015). Mutations in protrudin are linked to HSP (Hashimoto et al. 2014). Similar to protrudin, ORP1L senses endosomal sterol levels and regulates endolysosomal positioning and localizes to ER-LE MCS in a VAP-dependent manner (Rocha et al. 2009). VAP-A and VAP-B are two VAP proteins which was initially implicated in maintaining ER-PM MCSs and are linked to amyotropic lateral sclerosis (ALS) (Teuling et al. 2007). Mutations in VAPs or protrudin appear to induce protein aggregation, and consequently ER stress and cytotoxicity. The yeast NVJ-resident protein Tsc13 has a homolog in humans called TECR which is linked to autosomal recessive non-syndromic intellectual disability. Osh1 proteins in yeast NVJ are also conserved in humans as OSBPs (oxysterol binding protein) which localize at several MCSs – ORP5/8 at ER-PM (Chung et al. 2015) and ER-mitochondria (Galmes et al. 2016); ORP5 goes to ER-LD under oleate treatment (Du et al. 2020). The OSBPs and ORPs are proposed to sense sterol levels and function in sterol transfer. They are implicated in cholesterol-related metabolic dysregulations such as hypertension, and high blood pressure (Ngo and Ridgway 2009; Bouchard et al. 2009). No doubt continuing investigations to understand how lipid anabolism at the ER is co-ordinated with

catabolism at the lysosomes will uncover the mysteries of rapid lipid transport in an aqueous environment and will help develop novel therapeutic strategies.

**Lipid droplets in health and diseases**

While adapting to metabolically challenging conditions, cells store excess energy as reserve lipids in LDs. LD biogenesis is upregulated either under nutrient starvation, or to store excess lipids during oleic treatment, or to adapt to ER stress. Additionally, LDs have functions in cell signaling, membrane synthesis, energy supply, insulin and inflammation signaling and can serve as sinks for toxic lipid species.

*Lipid droplet synthesis and turnover*

As TAG levels at the ER increase, it can coalesce to form lipid lenses in the cytosolic ER leaflet (Walther, Chung, and Farese 2017). These lenses, also called a pre-LDs or nascent LDs (Kassan et al. 2013) form at specific ER subdomains which are marked by the enzyme acyl-CoA synthase long chain family member 3, ACSL3 (Kassan et al. 2013). The pre-LDs grow in size with more TAG synthesis and emerges from the ER to form the spherical shaped LDs coated by phospholipid monolayer which mostly contains PC. This LD core also contains the other hydrophobic molecule cholesterol ester (CE). The LD phospholipid coat is embedded with many LD proteins such as perilipins (PLINs) (Brown 2001), lipid synthesizing enzymes like DGATs, ACSLs, GPATs (Pol, Gross, and Parton 2014), and lipases such as adipose triglyceride lipase (ATGL) and hormone sensitive lipase (HSL). Lipases can act on the LD surface to supply FAs from LDs by breaking down TAG via a series of catabolic reactions called lipolysis (Zimmermann et al. 2004). PLIN family proteins control LD consumption by regulating lipolysis. LDs can also be harvested via autophagosomal / lysosomal degradation called lipophagy. Alternatively, TAGs can also be packaged as lipoproteins called chylomicrons and secreted out of the cell to be transported to other tissues and cell types (Jackson, Morrisett, and Gotto 1976; Zilversmit 1967).

*ER-LD contacts*

In response to an influx of exogenous fatty acid such as oleic acid, neutral lipid synthesis is upregulated, which either forms new nascent LDs or conjugates with the existing ones causing them to grow in size and emerge as mature LDs. As LDs bud from ER, they remain closely apposed making contacts and promote lipid flux from ER to LDs. In addition to lipid synthesizing enzymes such as DGATs, LD biogenesis and growth is co-ordinated by factors maintaining ER-LD crosstalk such as FATP1-DGAT complex (Xu et al. 2012) or Seipin (Salo et al. 2019; Szymanski et al. 2007). All these factors are proposed to mediate lipid flux from the ER to the growing LDs and consequently promote proper LD maturation from the ER important for maintaining cellular lipid balance.

Many questions remain on the basic biology of LDs. Whether mature LDs leave the ER surface or undergo fusion with other LDs is still debated. Whether there exists distinct subpopulation of LDs based on size, shape, protein or lipid composition and spatial organization, and whether they have distinct functions is also currently under study (Walther, Chung, and Farese 2017).

**Lipids in neuron functioning**

The preceding discussion suggests how defects in either lipid synthesis at the ER, or lipid transport between organelles via vesicular or inter-organelle contacts manifest in compromising organelle integrity. Overall any defects in intracellular lipid distribution, particularly failure in response to external stimuli, disrupts cellular functioning and signals for apoptosis. These defects are associated with mutations in either lipid synthesis enzymes at ER, or LTPs at MCSs, or lipid scaffolding/organizing factors. Neurons are highly hyperactive cells which use FAs as primary energy sources. This demands rapid and highly efficient lipid processing to adapt to constant environment stresses. Hence, even a slight deficiency in lipid processing could lead to a large consequence impacting neuron function. This underscores the role of lipid in maintaining neuronal health and homeostasis.

FA oxidation contributes ~20% of the energy demand of the brain, with the other major contribution from glucose metabolism (Spitzer 1973). Interestingly, FA oxidation occurs almost entirely in the astrocytes, which provide metabolic and structural support for neurons. Importantly, FAs in the brain also provide membrane building material for neurons, ultimately providing structural support to organelle membranes. Additional roles for lipid and FAs are as signal transduction molecules, which promote protection from inflammation. The lipid compositions of the pre- and post-synaptic membranes of neurons greatly impact functions of synaptic transmission such as vesicle fusion and receptor mobility. Dysregulation in lipid metabolism causes excitotoxicity, mitochondrial dysfunction, denervation of neuromuscular junctions, and impaired neurotransmission (Hayashi 2011).

Proper neuronal function is largely dependent upon the lipid composition in the CNS, as lipid metabolism is severely impacted in numerous acquired and genetic diseases including neuropathologies such as Alzheimer's disease (AD) and Parkinson's disease (PD). In particular, the accumulation of oxidated or peroxidated lipid species underlies symptoms related to many neuronal pathologies including ALS. Additionally, the neuronal PM harbors a high concentration of cholesterol and sphingolipids, which influence membrane fluidity and homeostasis, alterations of which can cause defects in neuronal function. Cholesterol also provides neuronal insulation required for rapid signal transduction. Conversely, PE and PUFAs such as arachidonic acid increase membrane fluidity for vesicular budding and membrane fusion at the synaptic region. PS is used to produce another essential PUFA, docosahexanoic acid, necessary for brain development and inflammatory signaling. PC in the ER is an abundant phospholipid and can also provide choline required for neurotransmission.

Paradoxically, LDs are not commonly found in neurons, but they nonetheless have important links to neurological diseases. Neurodegeneration and brain trauma are often associated with functions attributable to LDs such as serving as the cellular energy reservoir, provision of signaling molecules and inflammatory factors, and sequestration of toxic lipid species (Farmer et al. 2020). In fact, defective ER morphology, loss of chaperone activity, and protein misfolding and aggregation are found in multiple neuropathologies including HSP. Other examples include alpha-

synuclein aggregation in PD, and oligomerization of mutated hungtingtin protein in Hungtingtin's disease. All of these disorders correlate with enhanced LD accumulation and LD production in brain cells, although it is unclear if this is the cause or consequence of neurotoxicity. In the brain, the major LD-producing cells are the glial cells and astrocytes. In fact, patient suffering from AD, the most common form of dementia, exhibits fatty deposits or adipose-like inclusions in the glial cells. Since LDs are important contributors in cellular metabolism, their study in this context is emerging and becoming essential for the understanding of brain diseases, as LDs may serve as new therapeutic targets. Although the brain is rich in lipids, mechanisms related to LDs production, regulation, and function in this organ is under-explored unlike the vast knowledge we have with respect to LD function in liver, adipose tissue, and the heart.

Lipid crosstalk between neurons and neighboring glial cells has to be highly coordinated to facilitate proper neuronal function. In fact, during prolonged neuronal activity, toxic lipids from ROS-driven lipid oxidation can accumulate, and must be transported out of neurons to be stored in surrounding glial cells (Ioannou et al. 2019). This lipid transport is facilitated by lipid packaging into ApoE-containing lipoproteins, which traffic from neurons to the astrocytes. Following the consumption of these neuronal toxic lipid particles, the astrocytes process and store them as LDs. This lipid storage leads to increased LD biogenesis, which subsequently signals upregulation of FA detoxifying genes, and promotes mitochondrial FA oxidation. LD storage in astrocytes is thus essential for general lipid homeostasis in the brain. Besides the contribution by tau or amyloid deposits, the lipoprotein ApoE has also been implicated in progression of AD. Proper channeling of toxic FAs, thus, is critical for maintenance of neuronal health.

In recent years, there has been an attempt to study FA trafficking in brain between different tissue types which has provided us valuable insights regarding how deficiencies in intracellular lipid distribution can affect neuronal health. However, such studies have been very challenging; to dissect the molecular mechanisms of proteins involved in lipid metabolism, yeast, *Drosophila*, zebrafish, and C. elegans have been very useful model systems. These models share well conserved functions in lipid metabolism and allow easier genetic manipulation, monitor inter-tissue crosstalk,

tissue specific lipidomic profiling, and study metabolic pathways which often involve redundant elements in higher organisms.

**The yeast ER-vacuole tether Mdm1, a model protein for Snx14 function**

In a recent investigation conducted in yeast, Mdm1 was discovered as a novel ER-vacuole tether implicated initially in endo-lysosomal trafficking (Henne et al. 2015). Mdm1 emerged as an important protein of study for the Henne lab because of its conservation in humans in form of four homologs, called Snx13, Snx14, Snx19 and Snx25, among which Snx14 is implicated in a recently identified pediatric neurological disorder called SCAR20. Not much was known about Snx14 and its function when SCAR20 was first described, but its shared architecture with yeast Mdm1 made Mdm1 an ideal model protein for understanding Snx14 function. Yeast Mdm1 and its four human homologs all feature a Phox homology (PX) domain making them members of the SNX protein family. The conserved domains, starting from the N-terminal end of the proteins, include two transmembrane domains, the PX-Associated (PXA) domain, the regulator of G protein signaling (RGS) domain, the PX domain, and the C-Nexin domain. Among the mammalian orthologs, Snx19 is missing the RGS domain (**Figure 1.1A**).

In yeast, Mdm1 localizes to the NVJ by anchoring the ER via its N-terminal transmembrane domains and interacting with lysosomal phosphatidylinositol 3-phosphate (PI3P) via its PX (Phox homology) domain (**Figure 1.1B**). Mdm1 overexpression can induce hyper-tethering of these two organelles and expansion of NVJ. As mentioned above, the NVJ serves as a metabolically active zone of the ER network as NVJ also expands and serves as a "hotspot" for LD biogenesis under nutrient starvation.

The LD budding sites at the NVJ are determined by the molecular tether Mdm1, as Mdm1 variants that localize to other contacts such as the ER-PM contact can relocalize these sites (Hariri et al. 2019). Consistent with this, the hydrophobic N-terminal transmembrane region of Mdm1 is sufficient to associate with LDs and promote LD clustering at the NVJ. Given that Mdm1 can interact simultaneously with the ER, vacuole, and LDs, it localizes to unique tri-organelle contact

sites. The LD formation is shown to be mediated by interaction of Mdm1 with fatty acyl-coenzyme A ligase enzyme Faa1, which binds FFAs and converts into FA-CoA. Additionally, Mdm1 binds to FAs directly via its PX-Associated (PXA) domain. In line with this, Mdm1 loss affects FA activation and causes FFA accumulation similar to Faa1 deletion. This can lead to disruption of ER morphology and ultimately FA-induced lipotoxic cell death in yeast when treated with exogenous FAs (Hariri et al. 2019). Notably, Mdm1 truncated alleles which mimic Snx14 disease-associated mutations fail to localize at NVJ and shows perturbed sphingolipid metabolism, implying Snx14 mutants may have defects in cellular lipid metabolism (Henne et al. 2015).
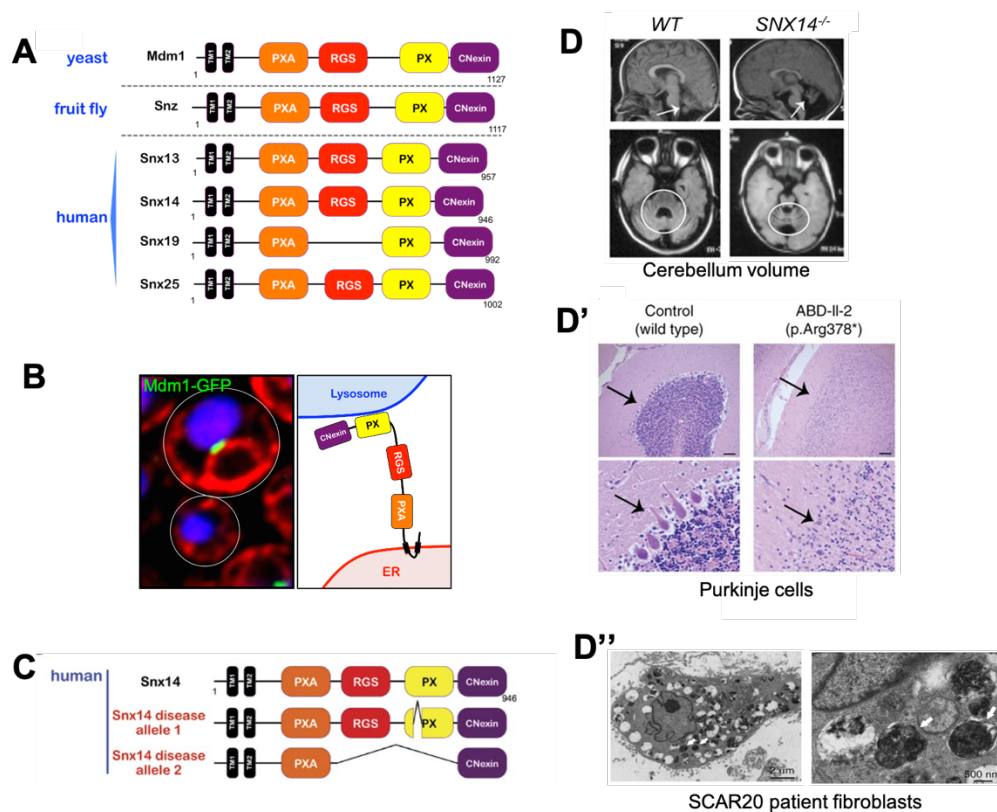


**Figure 1.1. Snx14 and SCAR20 disease**
- **A.** Protein architecture of yeast Mdm1, fly Snz and human Snx13, Snx14, Snx19 and Snx25 depicting the conserved domains.
- **B.** Localization of yeast Mdm1 (green) at NVJ (nucleus-vacuole junction). Mdm1 transmembrane (TM) domain anchors ER membrane and PX domain binds lysosome surface.
- **C.** Snx14 disease alleles showing mutations in PX domain in SCAR20 disease.
- **D.** Reduced cerebellar volume, Purkinje neuron cell death (D') and electron dense autolysosomal structure and increased vacuolation (D"). Adapted from (Thomas et al. 2014)

**Snx14 homolog Snazarus (Snz) in *Drosophila***

Based on domain conservation, there have been parallel studies of Snx14 family homologs in flies and zebrafish as well in addition to yeast Mdm1. The Mdm1 homolog in *Drosophila*, called Snazarus (Snz), was discovered in a genetic screen which explored genes involved in organismal aging. Compared to the mammalian homologs, Snz exhibits closest homology to Snx25. Further studies indicated that Snz mutations are associated with longevity, fatty acid regulation and fat storage as lipid droplets in fly adipose tissue (Suh et al. 2008). The fly adipose tissue stores lipids, and is the major lipid metabolizing tissue linked to lifespan extension and age-related diseases. In line with this, fat pads extracted from genetically obese mice shows a significant upregulation in the transcript levels of Snx13, Snx14 and Snx25.

Detailed investigation of Snz function in *Drosophila* larval fat body cells showed that Snz localizes at tri-organelle junctions where LDs form near ER-PM contact sites (Ugrankar et al. 2019). Intriguingly, this suggested Snz, a homolog of both Mdm1 and Snx14, could localize near organelles other than lysosomes. The molecular basis for this re-localization to ER-PM sites has been supported by liposome pelleting assays, which revealed a non-canonical lipid binding site on the Snz PX domain. Here, the Snz PX domain binds to multiple negatively charged phospholipids like PI4P and PI4,5P2 that are enriched at the PM, and does not interact with PI3Ps like yeast Mdm1. During the course of the Snz investigation, we also learned that *Drosophila* adipose tissue exhibits two spatially distinct LD subpopulations – the peripheral LDs (pLDs) regulated by lipophorin in hemolymph lipid trafficking, and the larger medial LDs (mLDs) which are maintained by *de novo* lipogenesis in the fat body. Though the exact mechanism of function of these two LD subpopulations are yet to be dissected, a model is that they help adipocytes balance extracellular and intracellular derived lipid pools. This example exhibits how LD sub-populations differing in size and protein composition are formed and maintained. Over-expression of Snz in the fat body alone has been shown to promote TAG synthesis and LD biogenesis in the adipocytes, and also induces starvation-resistance and prolonged organismal lifespan. In line with this, GFP-tagged Snz localizes at pLD subpopulation at ER-PM contacts, and possibly promotes extracellular

lipid uptake and packaging into LDs to maintain organismal homeostasis during chronic calorie overload.

**Snx14 and Snx13 in mouse and zebrafish studies**

To understand why loss of Snx14 causes SCAR20 disease in humans, there has been an attempt to generate a Snx14 global knockout mouse. However, a recent study showed that loss of Snx14 in mice is embryonic lethal at E12.5 (Bryant et al. 2020). Pathology analysis of the embryos revealed that this embryonic death was due to defects in placental development. Interestingly, similar pathology was observed in the absence of Snx14 paralog Snx13, which was embryonically lethal during E8.5 to E13.5 and showed defects in neural tube closure and vascularization (Zheng et al. 2006). As an alternative model system, zebrafish have been used to study the effects of Snx14 mutations. Snx14 knockdown in zebrafish is not lethal, but cause altered lipid metabolism and an altered lipid profile (Bryant et al. 2020). Specifically, we observe an increase in phospholipids and neutral lipids when Snx14 orthologs are deleted. Loss of Snx14 in zebrafish was also associated with hindbrain pathologies, accumulation of autophagic vesicles and Purkinje cell degeneration (Akizu et al. 2015), suggesting zebrafish may be a model system for human SCAR20 disease. Surprisingly, another study on dogs revealed that canine Snx14 mutations cause symptoms of progressive ataxia and Purkinje neuron loss in the Hungarian Vizsla dog (Fenn et al. 2016).

**Mammalian homolog Snx14 in SCAR20**

The cell biology studies of Snx14 homologs in all the aforementioned model systems were important and helpful to create a working hypothesis behind the underlying mechanism of function of Snx14 and its associated disease SCAR20. SCAR20 is an autosomal recessive disorder and is characterized by cerebellum ataxia and atrophy (**Figure 1.1D**), intellectual disability, coarse facial features, delayed motor development, relative macrocephaly, and speech defects. This disorder has been reported in 45 individuals from 24 families to date, and is caused by homozygous recessive mutations in the Snx14 gene, which shows ubiquitous expression in all human tissues. In one study, exome sequencing results from ~81 families with cerebellar atrophy revealed that approximately 10% of them was attributed by mutations in Snx14, suggesting this may be a

prominent cerebellar ataxia associated genetic disease. The SCAR20 patients suffered Purkinje neuron cell loss (**Figure 1.1D'**), and their cell-based studies revealed that fibroblasts of SCAR20 patients were demarcated with increased intracellular vacuolation, accumulation of lipid degenerative byproducts and dense granular deposits consistent with impaired autophagosomal and lysosomal clearance (**Figure 1.1D"**)(Thomas et al. 2014).

Initial investigation on the function of Snx14 linked its role to lysosomal function due to similar characteristics the SCAR20 patients shared with other lysosomal storage disorders such as Niemann-Pick type C disease. The homozygous recessive pediatric neurological disease Niemann-Pick type C is linked to the NPC1 and NPC2 protein complex which promote cholesterol export out of the lysosomes. Loss of function of NPC1/2 results in aberrant lysosomal lipid or sterol accumulation and disrupted autophagy. Following LDL receptor mediated endocytosis and after being trafficked to the lysosomes, how cholesterol is effluxed to other organelles is not known. Consistent with a potential role in lysosome cholesterol metabolism, Snx14 was identified as a gene linked to cholesterol transport out of the endolysosomal pathway in a screening study designed to identify regulators of low-density lipoprotein (LDL)-cholesterol transport (Chu et al. 2015). Additionally, SCAR20 patient fibroblasts reprogrammed into neuronal precursor cells through induced pluripotent stem cell (iPSCs) generation revealed enlarged lysosomes and increased levels of the autophagosome marker lipidated LC3II (Akizu et al. 2015). Collectively, these data provide preliminary evidence that Snx14 may play a role in lysosome lipid homeostasis, and may regulate lipid metabolism and/or transport similar to yeast Mdm1.

**Hypothesis**

Although several questions remained unclear from these studies: 1) although all studies indicate that Snx14 orthologs play roles in lipid metabolism and LD biology, the precise role of Snx14 in lipid and/or cholesterol metabolism is unclear. 2) Whether Snx14 functions as an ER-lysosome tether similar to Mdm1 remains to be determined. Not to mention that Snz also functions as an interorganelle tether but it tethers at ER-PM contacts and not ER-lysosome contacts. **We hypothesize that similar to Mdm1 and Snz, Snx14 is also a molecular tether involved in lipid metabolism.** Using mammalian tissue culture, the subcellular distribution of Snx14, and whether

it is a *bone vide* MCS tether that functions in lipid metabolism or transport, will be dissected in Chapter 2. 3) Whether Snx14 function was related to LD biology remained unexplored in previous literature. Given that Mdm1 in yeast and Snz in *Drosophila* play a significant role in modulating LD biogenesis, **we propose that Snx14 also functions in LD biogenesis.** This aspect of Snx14 function is described in Chapter 3. 4) How the absence of Snx14 caused defects in cellular homeostasis and defects such as delayed autophagosomal clearance, accumulation of lipofusion granular deposit and ultimately Purkinje neuron loss was not clear. Genetic manipulation of Mdm1 or Snz affects lipid storage in LDs and organismal homeostasis, implying that Snx14-deficiency alters lipid metabolism, which may underlie SCAR20 disease pathology. Here, we demonstrate that cells lacking Snx14 are sensitive to high dosage of exogenous FAs and scaffold lipid processing factors at specific ER microdomains to promote efficient downstream lipid processing. To understand this role, we conducted global proteomic and lipidomic analysis to determine the molecular mechanism of Snx14, which will be discussed in Chapter 4.

Collectively, all current studies on Snx14 homologs in different model system share common observations that indicate a role for Snx14 in lipid metabolism. As a graduate student, the purpose of my thesis research has been two-fold: 1) to utilize human tissue culture cells combined with cell biology, biochemistry, and genetics tools to dissect the cellular and molecular features of Snx14 function, and 2) to dissect how Snx14 loss in human cells impacts cellular lipid homeostasis and ultimately cell function.

My research on human Snx14 has shown that Snx14 is involved in FA-induced LD maturation. I find that the ER-resident Snx14 relocalizes from throughout the ER network to ER-LD contacts during oleate-induced LD biogenesis. Under oleate-treated conditions, Snx14 promotes LD biogenesis and modulates ER-LD contacts. In line with this, loss of Snx14 perturbs LD morphology and alters the lipid profile following oleate feeding. My studies have also utilized state-of-the-art APEX2 proximity-based technologies to examine the localization of Snx14 and its interacting proteins. APEX2-assisted proteomic studies of Snx14 associated ER-LD contacts revealed the presence of key LD factors such as perilipins (PLINs), lipid synthesizing enzymes such as DGATs, ACSL4, FASN and lipid transport factors such as Vps13. Interestingly, my work

has also revealed that *SNX14-KO* cells are hypersensitive to high dosages of saturated FAs (SFAs) such as palmitate. This is attributed to the functional interaction of Snx14 with a key FA delta-9-desaturase SCD1. Altogether, I propose that Snx14 plays an important role in FA processing and storage in LDs, the loss of which contributes to general cellular dysfunction of lipid metabolism underlying SCAR20 disease in humans.

# CHAPTER TWO

# Snx14 is not an ER-endolysosome tether, but its loss affects neutral lipid metabolism at the ER

**Abstract**

The pediatric neurological disorder SCAR20 has been associated with mutations in the protein encoded by the gene SNX14. The Snx14 yeast homolog Mdm1 is an ER-lysosome tether which functions in the nutritional stress response. Snx14 shares similar protein architecture with Mdm1 but whether these two proteins are functionally similar has been unclear. Based on the fact that SCAR20 patients exhibit loss-of-function Snx14 mutations in their endolysosomal-binding PX domain, and that patient skin biopsies manifest perturbed autophagy, we studied whether Snx14 is required for endolysosome function. We showed that the Snx14 PX domain exhibits negligible binding affinity for PI3P phospholipids, unlike yeast Mdm1 which binds PI3P with high affinity. Subcellularly we show that Snx14 is an ER-resident transmembrane protein and does not appear to be detectably enriched at ER-lysosome interfaces. In line with this, ER-lysosome/late endosome contact sites are still preserved in the absence of Snx14. Also, loss of Snx14 does not disrupt autophagosome-lysosome fusion, and in fact, the autophagic response is enhanced in Snx14-deficient cells. Since SCAR20 patients manifest electron dense granular lysosomal deposits similar to Nieman-Pick type C patients, in which lysosome cholesterol export is blocked, we also tested if Snx14 is involved in intracellular cholesterol transport. We did not observe defects in cholesterol export from lysosomes in Snx14-deficient cells, but we observed differences in neutral lipid levels including cholesterol-ester levels in Snx14-deficient cells. To test whether Snx14 functions as a lysosome "sensing" protein in response to nutrient starvation, we conducted a global RNAseq screen. Interestingly, we found that expression of FGF21, a major nutrient stress-response hormone, is altered by changing Snx14 expression. Whether Snx14 functions as a lysosome nutrient sensor, or whether Snx14 regulates lipid metabolism mediated through FGF21 signaling still remains unclear. Overall, our results indicate that *SNX14-KO* cells manifest defects in neutral

lipid metabolism including cholesterol homeostasis, characterized by decreases in cholesterol-ester and lysosomal cholesterol accumulation. We also characterize Snx14 as an ER-resident protein that localizes uniformly throughout the ER network via its N-terminal transmembrane domain, and relocalizes at ER-LD contacts following oleate induced LD biogenesis, which altogether provides evidence towards its function in cellular lipid homeostasis.

**Introduction**

Cells sense and respond to stress such as nutrient starvation by remodeling their metabolic pathways. Organelles such as lysosomes, mitochondria, and the endoplasmic reticulum (ER) serve as metabolic platforms to adapt to metabolic stress. Lysosomes degrade proteins, lipids, and carbohydrates to simpler forms such as amino acids, fatty acids, and pyruvate respectively and recycle them to other organelles either for *de novo* synthesis or to produce ATP. Nutrient deprivation modulates important regulatory pathways to enable the cells to adapt to stress. One such example is the inhibition of mTOR, associated with the lysosomes which drives autophagy during amino acid starvation (Settembre et al. 2012). Simultaneously, studies have shown that under nutrient stress other transcriptional regulators such as PPARα and ATF4 are activated, which via FGF21 signaling induce β-oxidation of fatty acids in mitochondria to provide cellular energy (Settembre and Ballabio 2014). On the other hand, the resulting metabolites from breakdown of macromolecules by lysosomes may be utilized by the ER for anabolic processes. Defects in the synthesizing machinery within the ER results in protein misfolding or accumulation of unfolded proteins causing ER stress, thus activating major components of the UPR stress response pathway (Walter and Ron 2011). To maintain cellular homeostasis under starvation stress, the metabolic pathways associated with different organelles must coordinate to balance the anabolic and catabolic processes. Failure to tolerate stress is the underlying cause of several disorders such as diabetes, obesity, and cardiovascular, and neurodegenerative diseases. How metabolic pathways associated with different organelles, mainly the ER, lysosomes, and mitochondria, communicate to adapt to starvation is not known.

Several studies in the past have shown that organelles communicate through membrane contact

sites (MCS), which have important roles in signaling, ion exchange, and metabolism as reviewed in (Hariri et al. 2016). One such inter-organelle MCS in yeast is the nucleus-vacuole junction (NVJ), which forms the bridge between the lipid synthesizing organelle, the nuclear ER, and the lipid degrading organelle, the vacuole (lysosome in mammals) (Pan et al. 2000). The NVJ is maintained by a cohort of regulatory proteins. Nutrient deprivation causes Nvj1, the most abundant protein localized at the NVJ, to be transcriptionally up-regulated which contributes to the expansion of the NVJ. Simultaneously, the NVJ recruits and organizes key enzymes such as fatty acyl-CoA synthases and HMG-CoA reductases which promotes upregulation of LD biogenesis. Mdm1 is another recently recognized molecular tether at the NVJ which plays a significant role in the regulation of lipid metabolism (Henne et al. 2015; Hariri et al. 2018). However, mammalian ER-lysosome tethers are less defined to date.

Humans encode an Mdm1 homolog called Snx14. Snx14 deficiency causes the neurological disorder SCAR20, a cerebellar ataxia characterized by intellectual disability, absent speech and accumulation of lipofusion granular like deposits. The electron dense lysosomal structures manifested in SCAR20 patient cells are strikingly similar to Niemann-Pick type C disease (Thomas et al. 2014). Such lysosomal storage diseases (LSDs) are associated with defects in lipid trafficking and accumulation of lipids like cholesterol and sphingolipids in the lysosome. Apart from Snx14, yeast Mdm1 has three other homologs in humans denoted as Snx13, Snx19, and Snx25. Mdm1 and its mammalian homologs feature four conserved domains including an N-terminal membrane-span domain and a C-terminal Phox homology (PX) domain (*Figure 1.1A*). SCAR20 patients show either complete Snx14 loss or loss-of-function truncations of Snx14 that perturb the PX domain (*Figure 1.1C*). Most proteins of the SNX family, by virtue of their PX domain, can localize on membranes such as the lysosomes that contain phosphoinositide phospholipids (PIPs). This is consistent with yeast Mdm1 which binds ER via its transmembrane domain and binds PI3P lipids enriched on vacuoles/lysosomes via its PX domain, thus tethering the nuclear ER to lysosomes (*Figure 1.1B*). Thus, Mdm1 overexpression hyper-tethers the NVJ. However, when Snx14-associated mutations were introduced into the Mdm1 PX domain, Mdm1 failed to localize at the NVJ and distributed throughout the ER. Notably, when these mutant Mdm1 constructs were over-

expressed they perturbed sphingolipid metabolism in yeast, indicating a role for Mdm1 in some aspect of lipid metabolism (Henne et al. 2015). However, *in vitro* biochemical and structural studies on the PX domains of the four mammalian Mdm1 homologs indicate reduced affinity of Snx14 to PI3P and other lipids (Mas et al. 2014). Lipid-binding assays have also shown the enrichment of most PX domains, but notably not the Snx14 PX domain, with PI3P lipids. This was supported by nuclear magnetic resonance (NMR) spectroscopic studies which showed that key residues within the canonical Snx14 PX PIP binding pocket, including an arginine required for PI3P binding, are naturally altered to lysine in the Snx14 PX domain, which provide the structural basis for its attenuated lipid binding. So, whether Snx14 functions as an ER-lysosome tether in cells is not known, but biochemical and structural data suggests it does not function directly in ER-lysosome tethering via a protein:lipid interaction.

Preliminary analysis of Snx14 and its role in lipid metabolism provide clues to Snx14 function, but also some confusing contradictions. SCAR20 patient fibroblasts exhibit the accumulation of electron dense autophagic structures. Similar autophagosome-lysosome accumulation was also reported in neural precursor cells generated from SCAR20 patient-induced pluripotent stem cells (Akizu et al. 2015). In line with this, Snx14 was detected in a siRNA knockdown screen targeting PX domain proteins designed to identify autophagy regulators under nutrient starvation (Knaevelsrud et al. 2013; Holland et al. 2016). However, the role of Snx14 in regulating autophagy could not be validated in a subsequent secondary screen, unlike other PX domain containing proteins including SNX18 and HS1BP3 (Knaevelsrud et al. 2013; Holland et al. 2016). To add confusion to Snx14's function, Snx14 has been reported to be involved in 5-HT6R (5-hydroxytryptamine subtype 6 receptor) mediated serotonin endocytic trafficking and signaling, possibly due to the fact that SNX proteins are traditionally thought to be soluble membrane binding proteins that function in vesicular trafficking (Ha et al. 2015). Intriguingly, Snx14 and its paralogs are the only known transmembrane domain-containing SNX proteins encoded in the mammalian genome, suggested they may function differently than other SNX proteins. Additionally, Snx14 was identified as one of the candidates involved in cholesterol transport out of the lysosomes in a global screen conducted by (Chu et al. 2015) to identify cholesterol transport regulators. All of this

evidence indicates Snx14 connection to lysosomal homeostasis, which I further investigated in this study.

To fully dissect Snx14 and its role(s) in lipid metabolism, we tested several hypotheses and interrogated several questions including: (1) Is Snx14 an ER-lysosome tether and does it facilitate cholesterol transport? (2) Does Snx14 function in intracellular lipid distribution or homeostasis? (3) Does Snx14 expression or sub-cellular distribution respond to nutritional stress and metabolic cues, and if so how? To answer this, we combined cell biology and biochemistry with global unbiased RNAseq to determine how Snx14 expression changes and affects metabolic signaling pathways in adaptive metabolic stress responses.

**Results**

**Snx14 mammalian homologs have differential binding affinity to lysosomes**

The PX domain is conserved structurally across eukaryotes and generally interacts with PIP lipids including PI3P, which is enriched on endolysosomal membranes. Unlike Mdm1 whose PX domain has been shown to interact with PI3P lipids, thus playing the role of a tether connecting the lysosomes to ER, it is not known whether the mammalian homologs also act as interorganelle tethers. We tested whether the Snx14 PX domain as well as other human paralog PX domain bind to the PI3P-containing yeast vacuole membranes *in vivo*. We expressed GFP-tagged PX domains of all four human Mdm1 orthologs (Snx13, Snx14, Snx19 and Snx25) in yeast and determined their sub-cellular localization. Interestingly, among all four of them, only Snx19 PX domain exhibited vacuolar surface localization similar to Mdm1 PX domain (**Figure 2.1A**). The others were localized only throughout the cytoplasm. This is consistent with a biochemical lipid:protein co-pelleting assay showing the Snx19 PX domain exhibited very high affinity for PI3P containing liposomes surface whereas such affinity was negligible for the PX domains of other three homologs (Mas et al. 2014).

Altogether, this suggests the possibility that Snx14 may require other factors in order to bind to endolysosomal membranes or that it does not interact with lysosomes directly. To determine Snx14 interactors, we expressed Flag-tagged Snx14 in U2OS cells and immunoprecipitated (IPed) with

Flag antibody conjugated beads. We used GFP-Flag as a control and similarly IPed them. Next we detected co-purifying proteins in both samples by mass spectrometry (MS) based proteomics. Intriguingly, we detected Snx13 whose interaction with Snx14 was validated by co-IP (**Figure 2.1B**). This appears similar to yeast Mdm1, which forms a complex with an Mdm1 paralog called Nvj3 (Henne et al. 2015). Nvj3 lacks a PX domain, and hence requires Mdm1 to function and properly localize to ER-lysosome contact sites in yeast (Henne et al. 2015). This may indicate that mammalian Snx13 and Snx14 may function together as a heterodimeric pair, where Snx13 might function as a "tether" and help to recruit Snx14 to ER-lysosome contacts or other sub-cellular regions, although more experiments are needed to test this.

Next we tested the subcellular distribution of both Snx14 and Snx13 in the human osteosarcoma U2OS cells. We did immunofluorescent staining of cells mildly over-expressing untagged Snx14 with Snx14 antibody. We observe that Snx14 distributes along the ER network of tubules and sheets, and co-localizes with ER marker Hsp90B1(**Figure 2.1C**). From these fluorescent micrographs it is not clear whether Snx14 enriches at ER-endolysosome contacts like yeast Mdm1. To determine whether Snx14 can associate with endosomes or lysosomes, we conducted immuno-fluorescent labeling of Snx14 with endosomal and lysosomal organelle markers. Strikingly, ~60% of Lamp2 positive organelles colocalize with Snx14 foci along the ER network when Snx14 is overexpressed in mammalian cells (**Figure 2.1C**). In contrast only ~10% of EEA1-positive endosomes co-localize with Snx14 (**Figure 2.1C**). This ER network distribution and Lamp2 association suggests that, although Snx14 may associate with endolysosomal compartments, its endolysosomal "affinity" is likely distinct from yeast Mdm1. A possible model is that the Snx13 PX domain enables Snx14's indirect interaction with lysosomes. In support of this, Snx13 co-localizes with Snx14 and shows similar ER localization and partial Lamp2 colocalization like Snx14, although more experiments need to be done to fully dissect if these two proteins form a hetero-multimer and co-localize at inter-organelle contacts (**Figure 2.1D**). This combined with the observed reduced affinity of the Snx14 PX domain for PI3P lipids on vacuolar surface, we conclude that the mammalian Snx14 protein is not a strong ER-lysosome tether similar to yeast Mdm1.
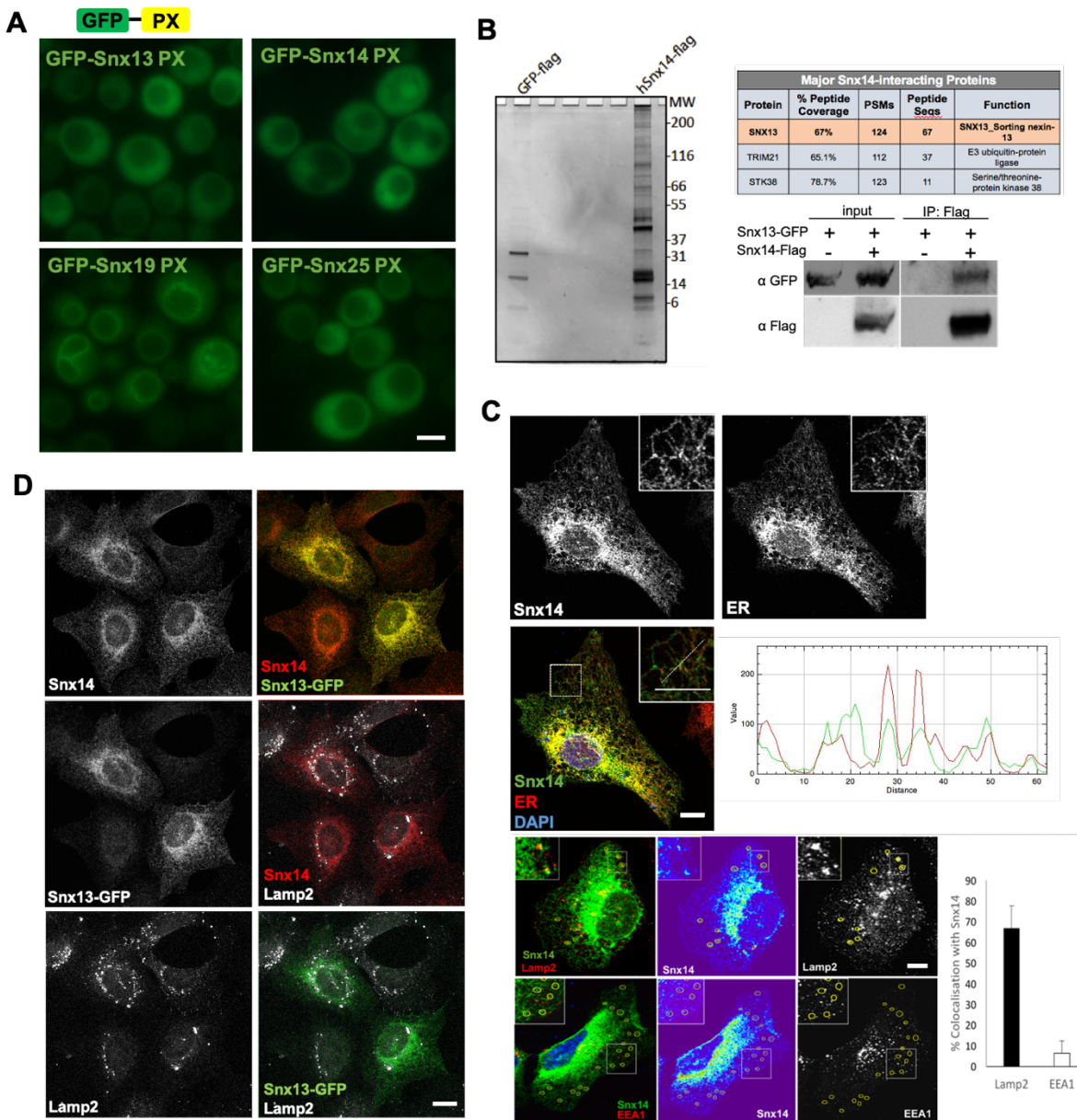
**Figure 2.1. Snx14 mammalian homologs have differential binding affinity to lysosomes**

**A.** Fluorescence micrographs of living yeast expressing GFP-tagged Phox homology (PX) domains from human Snx13, Snx14, Snx19, Snx25 in a pBP73A vector using an ADH expression promoter. Scale bar = 1μm.

**B.** Snx14-Flag and GFP-Flag (control) was immunoprecipitated with anti-Flag beads. Among the proteins pulled down, Snx13 and STK38 were found as the major Snx14 interactors from Mass Spectrometry (MS). Snx14-Flag co-IPs with Snx13-EGFP.

**C.** Overexpressed SNX14 (green) in U2OS cells colocalize with ER marker HSP90B1 (red). Scale bar = 10 μm. Line plot of the region in the inset showing that SNX14 (green) colocalize with HSP90B1 (red). ~60% Snx14 colocalizes with Lamp2 and ~10% Snx14 colocalizes with EEA1.

**D.** Immunofluorescent imaging of Snx14 (green) and Snx13 (red) shows that they colocalize at the ER. Snx14 (green) partially colocalizes with Lamp2 (gray). Same is the case with Snx13 (red). Scale bar = 5 μm.

To determine how Snx14 interacts with the ER membrane, we generated stable cell lines expressing either full length Snx14 (Snx14$^{Fl}$), an N-terminal fragment containing the transmembrane (TM) domain, PXA domain, and RGS domain (Snx14$^{N}$) and a C-terminal construct expressing the PX and C-Nexin domains (Snx14$^{PXCN}$), all tagged with 3XFlag (**Figure 2.2 A**) . Immunofluorescent imaging of these Snx14 constructs revealed ER localization of Snx14$^{N}$ like Snx14$^{FL}$ whereas Snx14$^{C}$ showed cytosolic localization (**Figure 2.2 B**). Subsequently biochemical subcellular fractionation showed enrichment of Snx14$^{N}$ with the microsomes similar to Snx14$^{FL}$ and that of Snx14$^{PXCN}$ in the cytosol (**Figure 2.2 C**). Additionally, density gradient subcellular fractionation studies of Snx14$^{Fl}$ and Snx14 with PX domain deletions (Snx14$^{\Delta PX}$) from a parent heterozygous for Snx14 mutation of a SCAR20 patient, indicated the association of both with the ER protein Calnexin, indicating removing functional PX domain does not affect Snx14 subcellular localization (**Figure 2.2 D,E,F**).
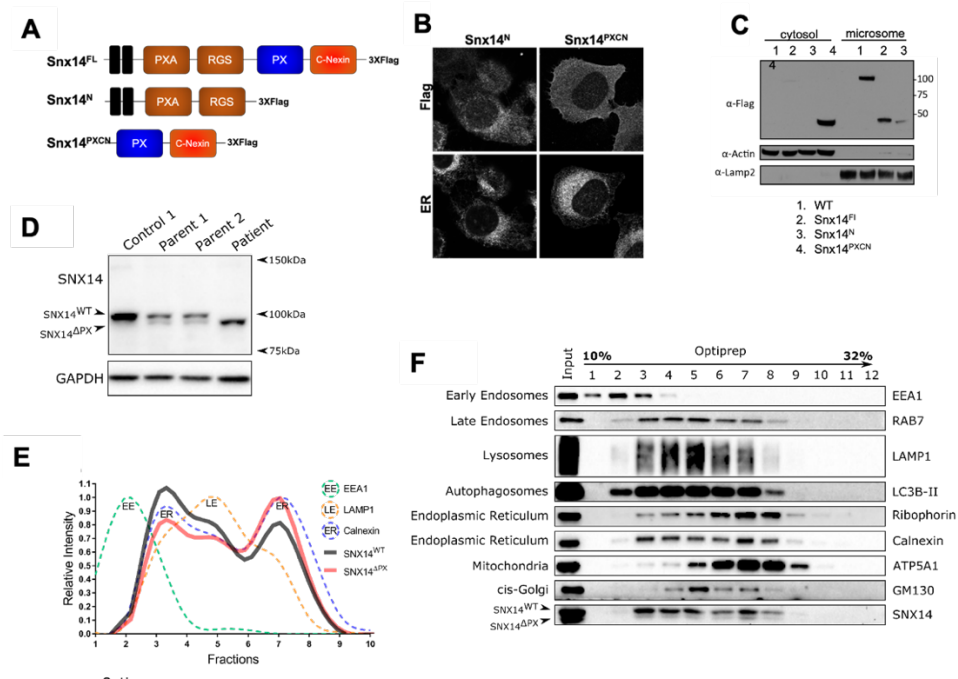


**Figure 2. 2 Snx14 is enriched in ER fraction**

A. Schematic diagram of Snx14$^{Fl}$, Snx14$^{N}$ and Snx14$^{PXCN}$ tagged with 3XFlag at the C-terminal.
B.  Co-immunofluorescent imaging of ER marker Hsp90B1 and 3XFlag tagged Snx14$^{N}$ and Snx14$^{PXCN}$.
C. Organelle fractionation showing Snx14$^{N}$ enrichment in the microsomes, and Snx14$^{PXCN}$ enriches in the cytosol.
D. Western Blot of lysates from patient heterozygous parents expressing both full length SNX14$^{WT}$ and SNX14$^{\Delta PX}$ proteins.
E. Organelle density fractionation of full length and SNX14$^{\Delta PX}$ proteins which show the subcellular distribution similar to the ER marker Calnexin (EE=Early endosome, LE= Late Endosome/Lysosome, ER=Endoplasmic reticulum).
F. Western blot of organelle fractions of full length and SNX14$^{\Delta PX}$ proteins and other organelle associated proteins. C, D, E and F are adapted from (Bryant et al. 2018).

**Snx14 is not involved in cholesterol transport out of the lysosomes**

Given that SCAR20 patients exhibit similar clinical symptoms like NPC patients (eg. coarse facial features, intellectual disability), and since the NPC1/2 complex proteins are involved in cholesterol efflux from lysosomes, we investigated whether Snx14 functions in cholesterol transport. In support of this investigation, a study using a genome-wide siRNA screen identified Snx14-deficient cells as defective in the retrograde transport of cholesterol out of lysosomes, although the mechanisms for this were unclear (Chu et al. 2015). In this screen, mammalian cells were forced to accumulate cholesterol within their lysosomes, and then induced to recycle this back to their plasma membrane (PM). They were then treated with Amphotericin B (AmB), a cell impermeable drug that binds to cholesterol in the PM, thus forming pores and causing cytoplasm leakage and cell death (**Figure 2.3A**). Cells with proper cholesterol transport and hence more cholesterol on PM will be more sensitive to AmB than those which have defects in cholesterol trafficking. The sensitivity of the cells is thus determined by assessing cell death. The genome wide screen had Snx14 as one of the candidates along with NPC1 and SREBP2 (**Figure 2.3A**). The perturbed lysosome morphology in *SNX14-KO* cells could explain the Niemann Pick Type C-like pathology observed in *SNX14*-deficient patients, and thus provide a cellular basis for this neurological disease.

In our lab, I tested whether Snx14 is involved in lysosome cholesterol trafficking by repeating the established aforesaid assay in WT cells, as well as Snx14 overexpressed (OE) cells and CRISPR/Cas9 *SNX14-KO* U2OS cells. As we hypothesize that Snx14 plays a role in cholesterol trafficking, we expected to see a defect in retrograde cholesterol efflux out of lysosomes in *SNX14-KO* cells, which would readout as resistance to AmB treatment. In contrast, if Snx14 promotes cholesterol efflux out of lysosomes, then Snx14OE cells will be more sensitive to Amphotericin B and will have more cell death compared to *SNX14-KO* cells.

To conduct the cholesterol transport assay, the following steps were performed to treat the cells: 1) the cells were treated with lovastatin to inhibit any intracellular cholesterol synthesis, 2) then cholesterol transport was blocked out of the lysosomes with U18666a compound and simultaneously the cells were fed with LDL particles to increase cholesterol levels inside

lysosomes, 3) cyclodextrin treatment was then done to remove cholesterol from the plasma membrane, and 4) the cells were washed and refed with cholesterol depleting media so we could track the accumulation of cholesterol to the PM. Next the cells were treated with AmB, and cell death was assessed by fixing the cells, staining with crystal violet and then measuring the intensity of the stain extracted in 10% acetic acid by spectrophotometer at 600nm optical density (OD). Remarkably, following this protocol we did not see any significant difference in cell sensitivity to AmB in either wildtype, *SNX14-KO*, or Snx14OE cells, suggesting that under these experimental conditions Snx14 does not influence retrograde cholesterol export from the lysosomes (**Figure 2.3B**).

To further determine whether intracellular cholesterol distribution changes with changes in Snx14 expression, we also stained WT and SCAR20 patient-derived fibroblasts with filipin, a chemical compound that binds cholesterol. There was no distinguishable change in filipin staining between the two cell types. However, when we also treated with U18666a, a compound which inhibits NPC1 activity, there was significant but mild increase in cholesterol accumulation in SCAR20 cells (**Figure 2.3C,D**). We noticed similar filipin staining in HEK293 tissue culture cells, where the effect of U18666a and Snx14 loss was additive showing increased perinuclear cholesterol accumulation. There was also an increase in late endosome (LE) and lysosomal structures under these conditions in *SNX14-KO* cells. However, TEM analysis indicated that the ER-lysosome contacts were still maintained in absence of Snx14, suggesting Snx14 does not function at these MCSs to maintain lipid homeostasis (**Figure 2.3E**).

As SCAR20 patient fibroblasts manifested lipofusion like granular autophagic deposits, the cellular response to autophagy induction was tested. Loss of Snx14 showed an elevated response to Torin-mediated autophagy induction which indicates either an increased rate of autophagosome formation or blockage in autophagosome-lysosome fusion. However, the formation of a functional autolysosome was not disrupted by Snx14 absence (**Figure 2.3F**). Another possibility can be ER derived autophagosome formation caused by ER stress due to Snx14 loss, but we could not determine any change in UPR activity in *SNX14-KO* as well (**Figure 2.3G**). Thus, Snx14 direct role in lysosome function could not be determined.
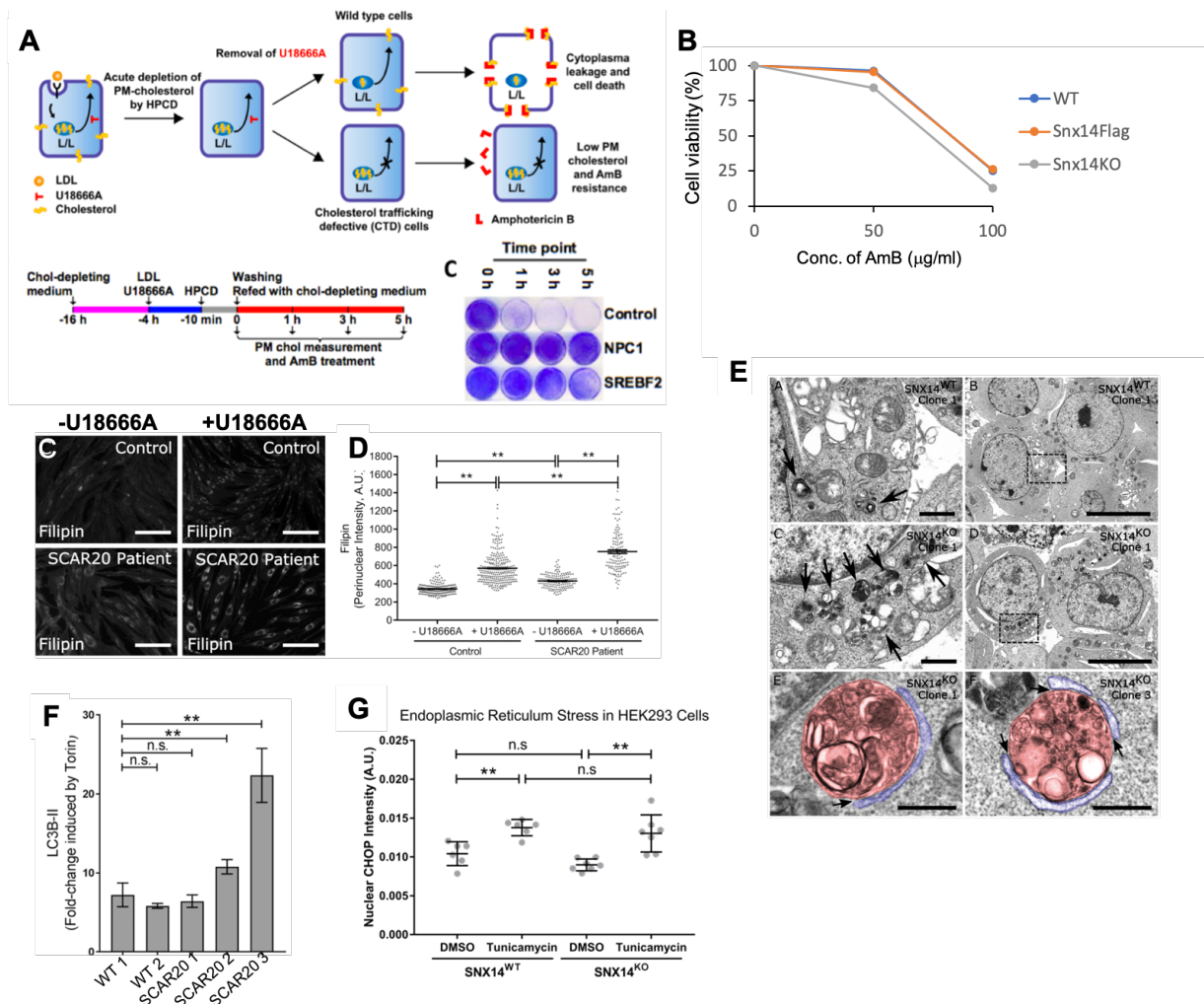
**Figure 2.3 Snx14 is not involved in cholesterol transport out of lysosome**

**A.** Representation of cell treatments followed by AmB. Incubation time of different cell treatments. Example of the effect of AmB assay on control, NPC1 and SREBF2 knockdown (adapted from *Chu et al, Cell, 2014*)

**B.** Effect of AmB assay on WT, Snx14Flag, *SNX14-KO*.

**C.** WT and SCAR20 patient derived fibroblasts stained with filipin with and without U18666A treatment. Scale bar = 200 µm.

**D.** Perinuclear filipin intensity from each cell shown in C quantified, $n \geq 143$, bars = mean, error bars = SEM, $**P \leq 0.01$, one-way ANOVA.

**E.** TEM images of SNX14[WT] and *SNX14-KO* HEK293 clones treated with U18666A shows greater accumulation of autophagic organelles (indicated by arrows) in absence of Snx14. Examples of membrane contact sites (arrows) detected between autophagic organelles (pseudo coloured red) and the endoplasmic reticulum (pseudo coloured blue) in *SNX14-KO* HEK293 clones. Scale bar = 1 µm (top row) Scale bar = 10 µm (middle row) Scale bar = 500 nm (bottom row).

**F.** Fold-change of LC3B-II expression in WT and SCAR20 patient cells in response to Torin1 treatment. $n = 6$, error bars = SEM, $**P \leq 0.01$, ns $P \geq 0.05$, Student's *t*-test. **G.** ER stress quantified as nuclear CHOP expression in SNX14[WT] and *SNX14-KO* cells that were treated with and without Tunicamycin for 24 hours. $N$=6-7, error bars = STD, $**p \leq 0.01$, n.s = $p \geq 0.05$, one-way ANOVA.

33

## Is Snx14 a lysosome-associated starvation sensor?

Lysosomes not only function to catabolize and recycle important metabolites, but also act as the decision-making center to regulate cellular growth and survival. Since lysosomes redistribute near the ER-rich perinuclear region in response to nutrient starvation, we tested whether Snx14 could potentially function as a type of lysosome "sensing" protein. In support of this concept, we found transcriptional up-regulation of both Snx14 and its interacting partner Snx13 in mammalian tissue culture cells under nutrient deprived conditions, consistent with the upregulation of Snx14 homolog Snz levels in starved flies (**Figure 2.4A**). To better understand how starvation-induced upregulation of Snx14 regulates cellular responses in adaptive metabolic stress, we conducted an unbiased RNAseq experiment comparing wild type cells (WT), cells overexpressing Snx14 (Snx14 O/E), and *SNX14-KO* cells (**Figure 2.4B**). Several genes, the expression of which was altered with changing levels of Snx14, are involved in amino acid metabolism, mitochondrial FA oxidation, lipid metabolism, and ROS stress response (**Figure 2.4B**). Interestingly, we found that Snx14 O/E significantly upregulates FGF21, a known ER stress-associated factor associated with lipid metabolism and nutrient adaptation. Similarly, *SNX14-KO* cells displayed low FGF21 expression
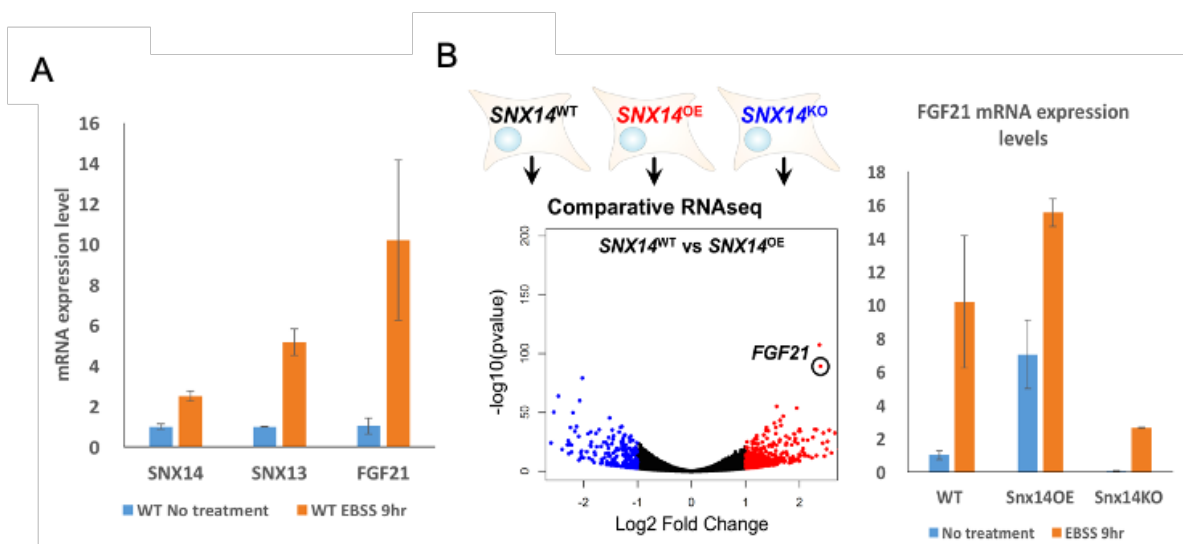


**Figure 2.4 Is Snx14 a lysosome-associated starvation sensor?**
A. Snx14, Snx13 and FGF21 mRNA levels increase in nutrient poor condition.
B. RNAseq reveals that change in Snx14 levels alter FGF21 levels. Also, in nutrient poor medium FGF21 levels fail to increase with loss of Snx14.

(**Figure 2.4B**). FGF21 has been mostly reported to be up-regulated in response to starvation stress, such as fasting or dietary restriction (**Figure 2.4A**). Consistent with this, when *SNX14-KO* cells are starved, they can no longer upregulate FGF21, indicating that Snx14 might be an upstream regulator of FGF21 expression (**Figure 2.4B**). Perhaps in support of this, we also observe more fragmented mitochondria in Snx14 O/E cells, which other reports indicate is associated with elevated mitochondrial β-oxidation to mobilize fat stores (Liesa and Shirihai 2013). Moreover, PPAR-alpha, PCR1 and ATF4 have been reported as transcription factors (TFs) regulating FGF21 expression and PPAR-alpha stimulation has been shown to up-regulate Snx14 (Bosch et al. 2008).

### *SNX14-KO* cells have defects in neutral lipid homeostasis

We observe lysosome cholesterol accumulation in *SNX14-KO* cells when NPC inhibition is induced by U18666a treatment. The cholesterol which ends up at the ER either gets trafficked to other organelles or is converted to CE which incorporates along with TAG into LDs. To understand what causes cholesterol accumulation in absence of Snx14, we tested other lipids such as TAG and CE levels in WT and *SNX14-KO* cells with and without U18666a and LDL treatment. We found slight but significant reduction in CE levels and upregulation in TAG levels in *SNX14-KO* cells (**Figure 2.5 A,B,A',B',A",B"**), whereas phospholipids levels remained unaltered (**Figure 2.5C**). TAG and CE are synthesized at the ER and forms the major components of ER-derived LDs. In line with this, Mdm1 in yeast associates with LDs as they bud at the NVJ during nutrient stress (Hariri et al. 2018). This prompted us to test whether Snx14 also associates with LDs during periods of LD biogenesis. To understand if Snx14 is involved in LD formation, we examined Snx14 sub-cellular localization following treatment with the fatty acid oleate, which induces LD biogenesis. Strikingly, immunofluorescent imaging revealed that Snx14 relocalizes from throughout the ER network to enrich at regions immediately surrounding the LDs in the form of ring-shaped structures following oleate treatment (**Figure 2.5D,E**). Altogether this suggests that Snx14 may function in LD biogenesis and ER-LD crosstalk, which will be the focus of the subsequent Chapters.
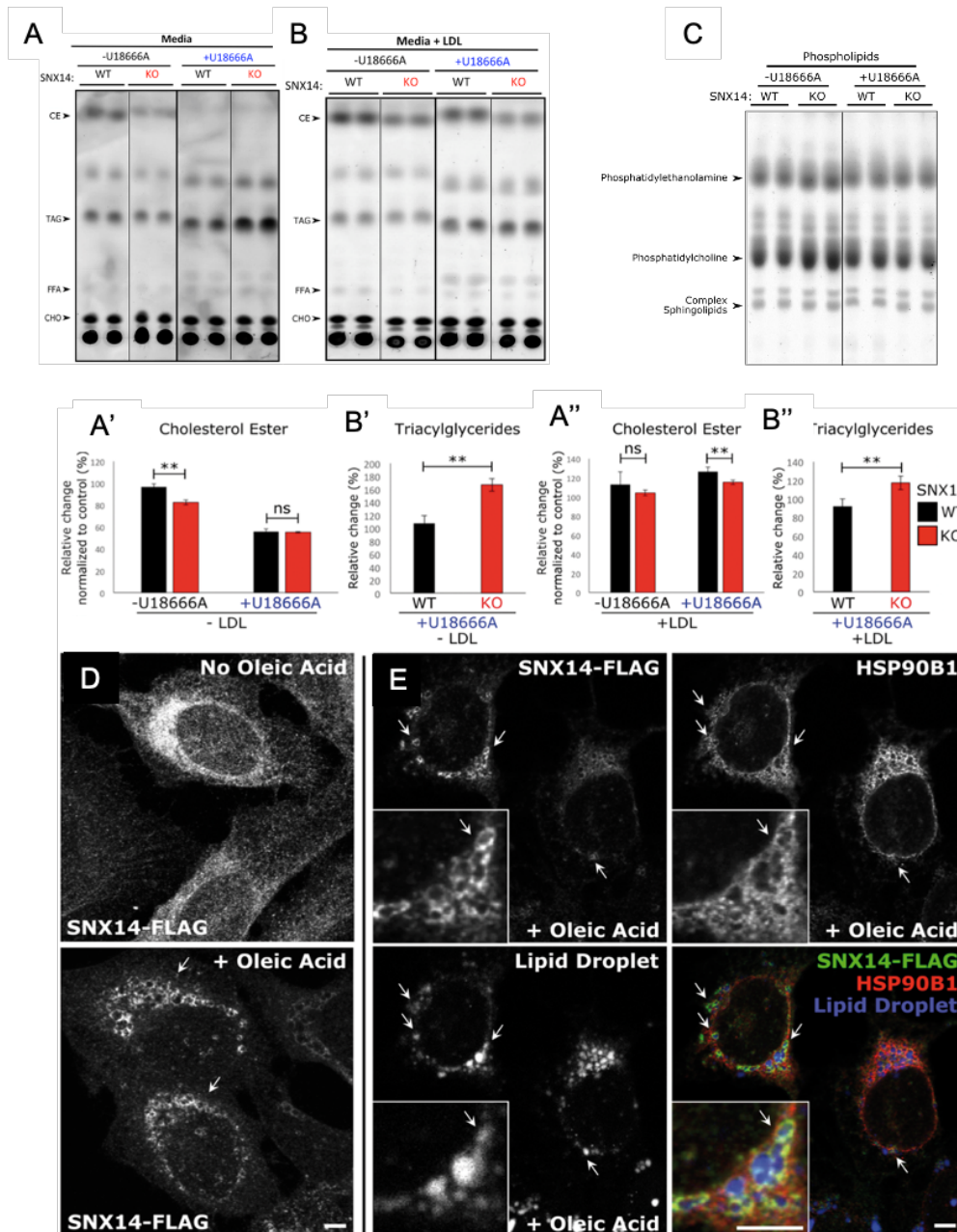
**Figure 2.5 *SNX14-KO* cells have defects in neutral lipid homeostasis**

A. Thin layer chromatography (TLC) analysis in SNX14WT and *SNX14-KO* HEK293 cultured cells without or with low-density lipoprotein (LDL) (B) and U18666A A'. Analysis of A show slight decrease in CE and increase in TAG in *SNX14-KO* cells (B') without LDL treatment. Same with LDL treatment in A" and B". N = 2, error bars = SD, **P ≤ 0.01, ns P ≥ 0.05, Student's t-test.

C. TLC of phospholipids in SNX14WT and *SNX14-KO* HEK293 cells showing no change.

D. Confocal images of Immunofluorescent staining of U2OS cells transfected with Flag tagged Snx14 with Flag antibody. Snx14 distributes throughout the ER with no oleate treatment and translocates as rings upon 600 μM oleate treatment for 8h (arrows).

E. Following oleate treatment, co-immunofluorescent imaging of SNX14-FLAG (Green), ER marker HSP90B1 (Red) and LD stain monodansylpentane (Blue), showing Snx14 enriches surrounding LDs. Scale bar = 5 μm.

36

**Discussion**

Lysosomes are not only the catabolizing centers of the cell, but have an emerging role as organelles that coordinate various cellular metabolic pathways. In response to starvation, lysosomes drive autophagy, and digest macromolecules to recycle metabolites back to organelles such as the ER for *de novo* synthesis. How the anabolic-catabolic crosstalk between these organelles is modulated is not very clear. Defects in repurposing the catabolized metabolites from the lysosomes cause lysosomal storage diseases (LSDs), many of which manifest as neurological diseases. Moreover, failure in transporting metabolites or lipids to other organelles such as mitochondria for FA oxidation and the ER for new synthesis inhibit major anabolic processes, causing diabetes, heart disease, etc. An example is the LSD NPC disease caused by blockage of cholesterol export from lysosomes resulting in pathological accumulation of lysosomal cellular debris. These electron dense lysosome accumulation in NPC patients show similar characteristics and symptoms to SCAR20 patients.

Mutations in Snx14 protein encoding region is associated with SCAR20 disease. Since studies in yeast homolog Mdm1 revealed its function as ER-lysosome tether and SCAR20 patients exhibited increased vacuolation and electron dense lysosomal deposits, we hypothesized that Snx14 functions in lysosomal homeostasis. However, detailed investigation revealed several negative results, including:

1) we do not observe Snx14 acting as a bone vide ER-lysosome tether in mammalian cells. Indeed, cell biological analysis of its PX domain shows that it fails to localize to PI3P containing organelles, and biochemical data and structural data indicates that the PX domain does not bind to PIP containing liposomes in vitro because it contains natural mutations which attenuate PIP binding (Mas et al. 2014). However, we do find that, Snx14 is an ER resident protein which may transiently colocalize with lysosome/late endosomes, potentially through its interaction with paralog Snx13.

2) In contrast to previous studies which reported Snx14 function in autophagy, further studies (Bryant et al. 2018) showed that autophagosome-lysosome fusion is intact in *SNX14-KO* cells. In fact, Snx14 loss actually enhances autophagic response. Thus, the increase in

lysosome formation and autophagy induction might be an indirect response to other stresses associated with Snx14 loss. In line with this, we conducted a cholesterol trafficking assay to determine whether Snx14 is involved in cholesterol transport like NPC1. However, this assay indicated that retrograde cholesterol transport was generally unaltered with loss or over-expression of Snx14, suggesting that Snx14 is not required for cholesterol transport from lysosomes contrary to published large-scale screening work. It should be noted that the large-scale screening study (Chu et al. 2015) did not validate their Snx14 hit from their screening.

3) To understand if Snx14 responds to nutrient stress like Mdm1, we determined the transcriptional expression changes for both Snx13 and Snx14 in cells grown in different cultured media. We found that both Snx13 and Snx14 are transcriptionally upregulated when cells are starved of FBS and other nutrients when placed in EBSS minimal media. Moreover, unbiased RNAseq data showed that genes necessary for amino acid metabolism, mitochondrial FA oxidation, lipid metabolism, and ROS stress altered with changing Snx14 expression levels. All these genes are associated with ER or organelle homeostasis, which is able to sense starvation and responds by secreting proteins responsible to mobilize energy stores. One such example is FGF21 which we observe is impacted by Snx14 expression. In response to starvation stress, FGF21 acts on cells in an autocrine, endocrine or paracrine manner. FGF21 is known to be secreted primarily by the liver into the blood. FGF21 is then transported to other cells such as adipocytes, cardiomyocytes etc. where it triggers mobilization of fat stores, stimulates lipolysis and drives mitochondrial fatty acid oxidation. All these studies suggest the possibility that Snx14 levels increase in response to starvation stress, which triggers alterations in metabolism which may subsequently alter the signaling of FGF21. One possibility is that Snx14 modulates energy metabolism at the ER, which is facilitated by FGF21 that plays a role in utilizing fat storage to provide cellular energy. How Snx14 may function as a potential nutrient sensor, and whether Snx14 regulates lipid metabolism mediated through FGF21 signaling still needs further investigation. In line with this, recently published ChIP-Seq binding assay has shown that Snx13 is upregulated by Srebp2 in nutrient deprived conditions.

4) Our initial work on the sub-cellular localization of Snx14 indicated that Snx14 can be spatially redistributed from the ER network to regions of the ER adjacent to LDs after cells are fed with the fatty acid oleate. This initial observation suggests that Snx14 may play a role in lipid metabolism and potentially LD biogenesis, which will be the focus of the subsequent chapters of this dissertation.

Collectively, this chapter of data indicates that rather than directly functioning at lysosomes, Snx14 functions at the ER where lipids are newly synthesized and processed. Indeed, Snx14 localization to the ER and association with ER-derived LDs under oleate-fed conditions implies a role for Snx14 in ER lipid homeostasis. In support of this, the main component of LDs, the neutral lipids CE and TAG, are altered in Snx14-deficient cells, especially when lysosomal cholesterol export is blocked by U18666a treatment. LDs are stress response organelles with several functions such as energy storehouses and storage compartments for toxic lipids. They have been implicated in many neurological diseases such HSP, ALS, and PD. In the next chapter, I will focus on dissecting how Snx14 interacts with the ER and LDs, and its role in LD and fatty acid homeostasis.

# CHAPTER THREE

# Cerebellar ataxia disease-associated Snx14 promotes lipid droplet growth at ER-droplet contacts

## Abstract

Lipid droplets (LDs) are nutrient reservoirs utilized by cells to maintain homeostasis. Nascent droplets form on the endoplasmic reticulum (ER) and grow following an influx of exogenous fatty acids (FAs). The budding of LDs requires extensive ER-LD crosstalk, but how this is regulated remains poorly understood. Here, we show that sorting nexin protein Snx14, an ER-resident protein associated with the cerebellar ataxia SCAR20, localizes to ER-LD contacts following FA treatment where it promotes LD maturation. Using proximity-based APEX technology and topological dissection, we show that Snx14 accumulates specifically at ER-LD contacts independently of Seipin, where it remains ER-anchored and binds LDs *in trans*. *SNX14-KO* cells exhibit perturbed LD morphology, whereas Snx14 over-expression promotes LD biogenesis and extends ER-LD contacts. Multi-time point imaging reveals that Snx14 is recruited to ER microdomains containing the fatty acyl-CoA ligase ACSL3, where nascent LDs bud. We propose that Snx14 is a novel marker for ER-LD contacts and regulates FA-stimulated LD growth.

## Introduction

Fatty acids (FAs) are fundamental cellular metabolites used for membrane biosynthesis, cell signaling, and energy via their oxidation. Excess FAs are stored as triacylglycerol (TAG) housed within cytoplasmic organelles called lipid droplets (LDs). Defects in FA processing or the inability to store excess FAs in LDs lead to cellular lipotoxicity and are associated with metabolic syndromes such as diabetes, obesity, cardiovascular disease, and numerous neurological diseases (Listenberger et al. 2003).

LDs bud from the surface of the endoplasmic reticulum (ER) and receive TAG from the ER (Fujimoto and Parton 2011; Guo et al. 2009). Although the mechanisms of LD biogenesis remain

debated, it is generally accepted that neutral lipids accumulate at distinct microdomains within the ER membrane bilayer, leading to the formation of a lipid "lens" between the monolayer leaflets that gradually grows as neutral lipids coalesce (Athenstaedt and Daum 2006). In fasted mammalian cells, ER microdomains containing nascent LDs designated pre-LDs have been observed, and are marked by the enzyme Acyl-CoA Synthetase Long Chain Family Member 3 (ACSL3) (Kassan et al. 2013). These small pre-LDs can grow in response to an influx of FAs such as oleic acid (OA), which is esterified by ACSL3 and combined with diacylglycerol (DAG) via DAG O-acyltransferase (DGAT) enzymes into TAG. In *C. elegans,* the ER-localized Fatty Acid Transport Protein 1 (FATP1) interacts with the LD-localized DGAT2 to promote OA incorporation into TAG during LD growth (Xu et al. 2012). Furthermore, numerous studies implicate the protein Seipin in LD homeostasis, and Seipin localizes to ER-LD contacts in yeast and mammalian cells (Szymanski et al. 2007; Salo et al. 2016). Thus, LD homeostasis and growth requires extensive ER-LD inter-organelle crosstalk, which ultimately governs the flux of lipids from the ER into the growing LD through either direct ER-LD contacts or recruitment of LDs to the ER surface (Wilfling et al. 2014). How this ER-LD crosstalk is coordinated remains poorly understood, and ER-LD contacts themselves remain poorly characterized as they are difficult to observe by conventional microscopy.

Recent studies in yeast reveal that LD biogenesis can also be spatially restricted to distinct sub-regions of the ER surface. When yeasts are deprived of a carbon source, LDs bud and accumulate on the surface of the nucleus (nuclear ER) which is in close apposition to the vacuole, a region known as the Nuclear ER-Vacuole junction (NVJ). NVJ-associated LD clustering is regulated by Mdm1, an ER-resident protein that interacts with the ACSL3 homolog Faa1 and promotes LD biogenesis (Hariri et al. 2018). Although mammalian cells lack NVJ contacts, Mdm1 is a member of the sorting nexin (Snx) protein family and is conserved in humans as four orthologs: Snx13, Snx14, Snx19, and Snx25. Snx14 loss-of-function mutations are associated with a distinct cerebellar ataxia termed Spinocerebellar Ataxia Autosomal Recessive 20 (SCAR20; OMIM 616354) (Thomas et al. 2014; Shukla et al. 2017). This disease to date has been reported in 45 individuals from 24 families and is characterized by cerebellar hypertrophy, intellectual disability,

and defects in speech. Recent studies reveal that human Snx14 localizes to the ER network, and its loss causes defects in neutral lipid homeostasis, although its function in lipid metabolism remains unclear (Bryant et al. 2018).

Here, we characterize Snx14 and mechanistically dissect how it regulates ER-LD crosstalk and LD maturation. Using proximity-based ascorbate peroxidase (APEX) technology combined with multi-time point imaging and biochemistry, we find that Snx14 localizes to ER microdomains containing pre-LDs following OA treatment where it promotes LD maturation at ER-LD contacts.

## Results

### Snx14 localizes at ER-LD contacts following oleic acid (OA) treatment

Previously, we demonstrated that Snx14 is an ER-resident protein whose loss in HEK293 cells perturbs ER-associated neutral lipid metabolism. Furthermore, the addition of OA, which is esterified in the ER prior to its incorporation into LDs as TAG, induced the accumulation of Snx14 near LDs (Bryant et al. 2018). To better understand the cellular function of Snx14, we investigated how its sub-cellular localization changed in response to OA treatment by culturing U2OS cells overnight with BSA-conjugated OA (denoted hereon simply as OA treatment). In the absence of OA, confocal imaging of immuno-fluorescently labeled U2OS cells stably expressing an untagged Snx14 revealed it was uniformly distributed across the ER. Following 16 hours of OA treatment to induce LD expansion, Snx14 redistributed and accumulated within a subdomain of the ER that formed ring-like structures surrounding LDs (**Figure 3.1A**). We observed the same result when we examined a cell line stably expressing a C-terminally EGFP-tagged Snx14 construct (**Supplementary Figure 3.1A**). In both experiments, whether Snx14 remained ER-associated or transferred to the LD surface following OA treatment could not be distinguished at this resolution. Nonetheless, as a consequence of this redistribution, quantification of the Snx14-ER co-localization between the two conditions revealed a significant loss of ER co-localization following OA treatment, changing from a Pearson's coefficient (r) of 0.41±0.07 in no OA to -0.06±0.01 (**Supplementary Figure 3.1A**).

To examine the accumulation of Snx14 near LDs at higher spatial resolution, we utilized the genetically encoded proximity-based labeling technology ascorbate peroxidase (APEX2), which allows high-resolution sub-cellular localization of a protein-of-interest via thin section transmission electron microscopy (TEM) (Martell et al. 2012; Lam et al. 2015). We generated U2OS cells stably expressing Snx14$^{EGFP-APEX2}$, and treated them with OA to stimulate LD production. These cells were then imaged in bright field microscopy to confirm the function of the APEX2 enzyme tag. When treated with diaminobenzidine (DAB) and hydrogen peroxide ($H_2O_2$), but not in their absence, APEX2 catalyzes the formation of an electron dense precipitate that is deposited within ~10 nm of the enzyme (**Figure 3.1B**, **Supplementary Figure 3.1B**).

Next, cells were treated with OA and then exposed or not to DAB+$H_2O_2$ before processing for thin sectioning TEM. Both cell samples contained many LDs, but the DAB+$H_2O_2$ treated cells contained unambiguous electron dense DAB precipitates on the surface of distinct LDs (**Figure 3.1C-E**). High magnification imaging revealed that the DAB stain accumulated specifically in spaces between the LD surface and ER tubular structures that were wrapped around the LD (Figure 1D, D' green arrows). We also noted that regions of the LD surface not wrapped by ER contained no DAB stain (**Figure 3.1D**, **D' blue arrows**). Clusters of small LDs also exhibited DAB stain around the LD surfaces, and ER tubular structures could be observed closely associated with these small LDs (**Figure 3.1E**, **Supplementary Figure 3.1D**). Notably, there was no visible DAB stain associated with LDs that were not associated with ER (**Figure 3.1D, D' purple stars**). We did not detect any obvious DAB stain at other inter-organelle contact sites such as ER-mitochondria or mitochondria-LD contacts (**Supplementary Figure 3.1C, blue diamonds**). Likewise, no obvious DAB stain was associated with the ER membrane network itself (**Figure 3.1D, D' orange arrows**). These observations suggested that Snx14 may associate with the LD surface specifically at sites of ER-LD contact.
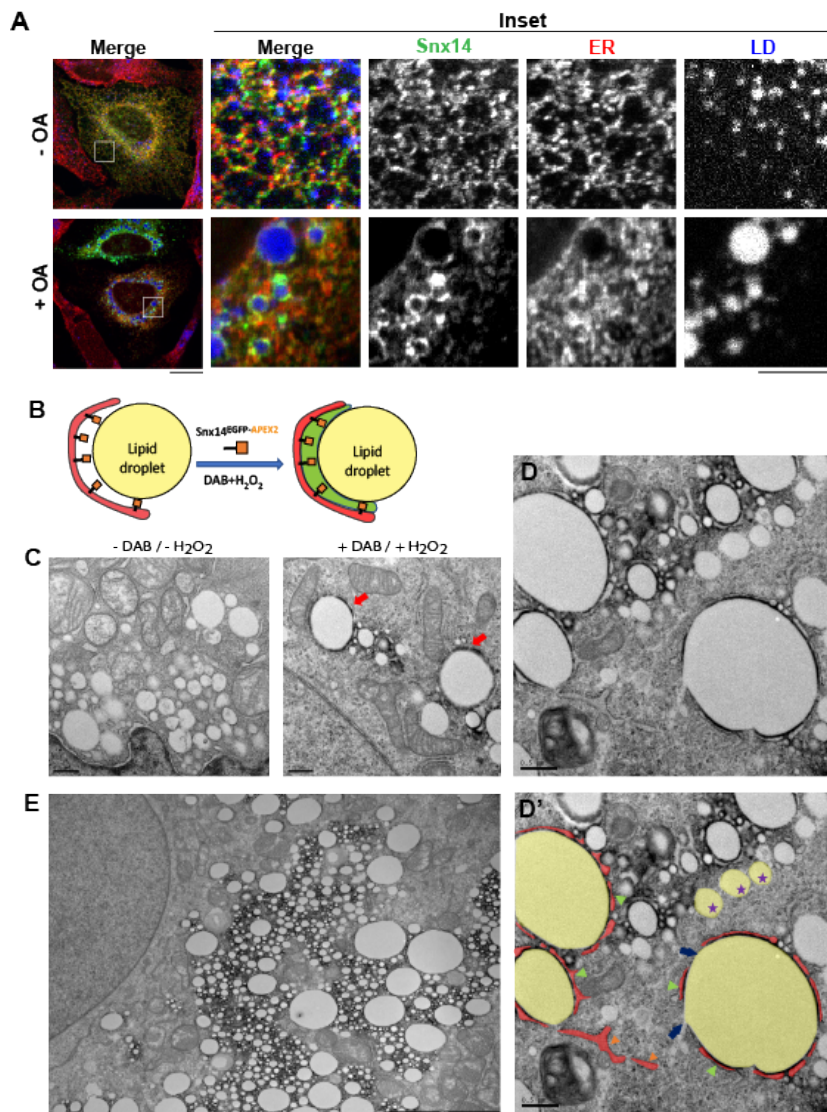
**Figure 3.1 Snx14 localizes at ER-LD contacts following oleic acid (OA) treatment**

**A.** Localization of Snx14 in U2OS cells in absence and presence of oleic acid (OA) respectively. Co-IF staining of the cells stably expressing an untagged Snx14 with $\alpha$-Snx14 antibody (green) and $\alpha$-HSP90B1 (ER marker, red) antibodies and LDs stained with MDH (blue) and imaged by confocal microscopy. Inset of OA-treated cells displays Snx14 accumulating around LDs. Scale bar = 20µm. Scale bar of insets = 5 µm.

**B.** Schematic diagram showing Snx14$^{EGFP-APEX2}$ fusion at ER-LD contacts.

**C.** TEM micrographs showing OA treated cells with and without DAB + $H_2O_2$ staining. The dark precipitate with DAB + $H_2O_2$ treatment indicates presence of Snx14$^{EGFP-APEX2}$. Scale bar = 0.5µm.

**D.** TEM micrograph showing SNX14$^{EGFP-APEX2}$ expressing cell with DAB precipitate at ER-LD contacts. D'. Image from D showing pseudo-colored ER (red), LD (yellow), green arrows pointing at DAB precipitate (Snx14) specifically at the junction of ER and LD. The blue arrows indicate a region of LD surface which lacks ER wrapping and also lacks DAB precipitate. Purple stars indicate LDs without any detectable ER association (and no DAB precipitate). The orange arrow indicates an ER membrane itself. Scale bar = 0.5µm.

**E.** Lower magnification TEM micrographs of a Snx14$^{EGFP-APEX2}$ expressing cell following OA treatment and stained with DAB, showing precipitate surrounding various LDs entangled with the ER network. Scale bar = 0.5µm.
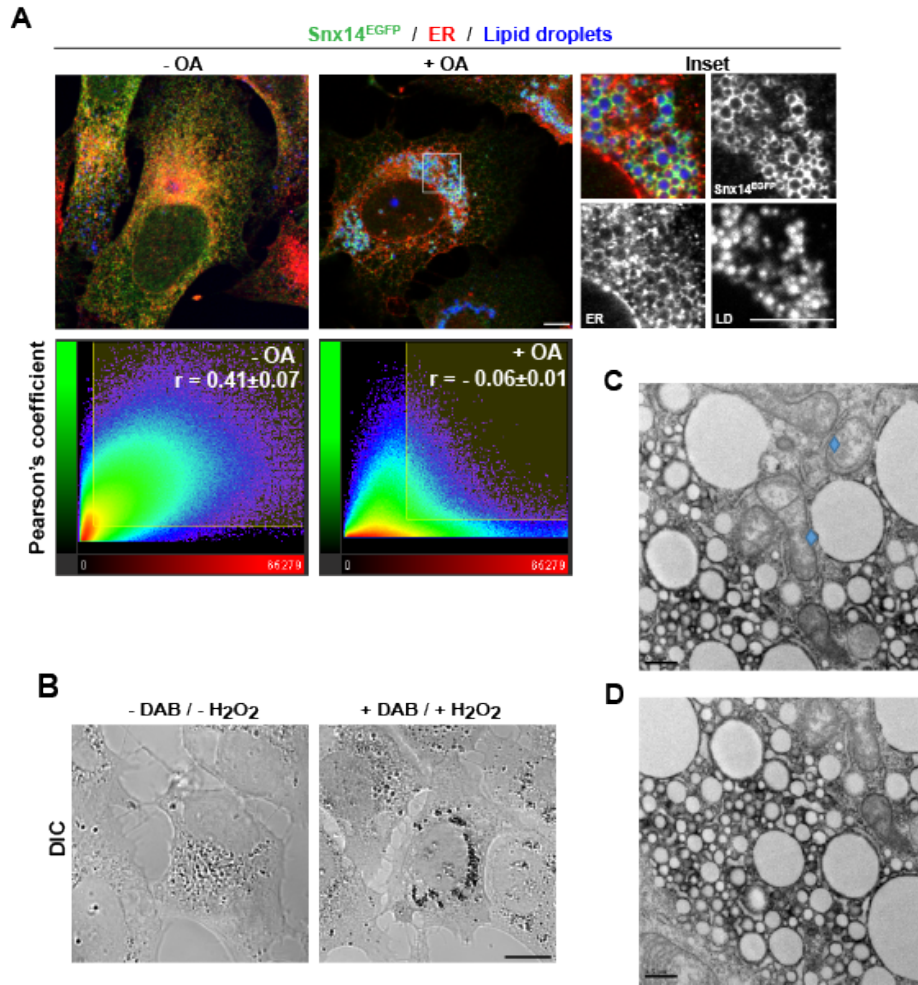
**Supplementary Figure 3.1**

**A.** Co-immunofluorescent staining of U2OS cells transiently transfected with Snx14[EGFP], in absence and presence of OA, were performed with α–EGFP (green) and α-HSP90B1 (ER marker, red) antibodies and LDs were stained with monodansylpentane MDH, blue) and imaged by confocal microscopy. Scale bar = 10 μm. Representative cytofluorogram of Snx14 (green) and ER (red) showing Snx14 and ER colocalization (r = 0.41±0.07) in untreated conditions, and following OA treatment (r = - 0.06±0.01). ~20 cells were quantified for the average r values.

**B.** Differential Interference Contrast (DIC) images of U2OS cells expressing Snx14[EGFP-APEX2] and treated with OA overnight without (*left*) and following DAB+ $H_2O_2$ staining (*right*). Dark regions indicate presence of DAB precipitate. Scale bar = 14μm.

**C.** TEM image of cellular region showing mitochondria, LDs, and ER. Blue diamonds denote close junctions between ER-mitochondria and LD-mitochondria devoid of detectable DAB stain. Scale bar = 0.5μm.

**D.** Zoom-in of small LD clusters showing grape-like clustering of LDs with associated ER membranes and DAB staining them. Scale bar = 0.5μm.

**Snx14 interacts with LDs *in trans* from the ER surface**

The enrichment of Snx14 specifically at ER-LD contacts following OA treatment suggested at least two possible models: 1) Snx14 translocates from the ER to the LD surface following OA treatment, or 2) Snx14 is retained in the ER and associates with LDs *in trans* at ER-LD contact sites. To test these models, we next conducted biochemical fractionation of OA-treated U2OS cells stably expressing Snx14$^{EGFP}$ to generate ER, LD, and cytoplasmic fractions and probed for Snx14 in each fraction using an anti-EGFP antibody. Snx14$^{EGFP}$ was primarily enriched in the ER membrane fraction, with negligible signal detected in the LD float fraction, suggesting Snx14 remained associated with the ER following its association with the LD surface (**Figure 3.2A**). To confirm that endogenous Snx14 also remained in the ER following OA treatment, we also fractionated wildtype (WT) U2OS cells and probed for Snx14. We detected endogenous Snx14 in the membrane fraction similar to the Snx14$^{EGFP}$ stably expressing cell line (**Supplementary Figure 3.2A**).

To topologically dissect how Snx14 remained anchored at the ER but accumulated at ER-LD contact sites, we generated cell lines stably expressing 3XFlag-tagged fragments of Snx14: full length Snx14 (Snx14$^{FL}$) or Snx14 fragments encoding its N-terminal transmembrane, PXA and RGS domains (Snx14$^{N}$), or C-terminal PX and C-Nexin domains (Snx14$^{PXCN}$). Whereas, the Snx14$^{N}$ fragment contains predicted transmembrane helices, the Snx14$^{PXCN}$ fragment is predicted to be soluble and face the cytoplasm. To quantitatively assess the sub-cellular localization of these Snx14 constructs, we biochemically isolated membrane, LD, and cytosolic fractions following ~16hr OA treatment, and immuno-blotted for each construct with anti-Flag antibody. Indeed, both Snx14$^{FL}$ and Snx14$^{N}$ were present primarily in the ER membrane fraction following overnight treatment with OA (**Figure 3.2C**, **Supplementary Figure 3.2B**). However, Snx14$^{PXCN}$ was significantly associated with the LD fraction, suggesting it was sufficient to interact with LDs (**Figure 3.2C**, **Supplementary Figure 3.2B**).

Next we evaluated the sub-cellular distribution of these constructs using EGFP-tagged versions and fluorescence confocal microscopy (**Figure 3.2B**). As previously observed, Snx14$^{FL}$ localized

to ER-LD contacts following OA addition (**Figure 3.2D**, **Supplementary Figure 3.2C**). In contrast, Snx14$^{N}$ distributed throughout the ER network following OA treatment, suggesting removal of the C-terminal region attenuated LD association (**Figure 3.2D**). Consistent with this, Snx14$^{PXCN}$ accumulated around the surfaces of LDs, consistent with its biochemical fractionation (**Figure 3.2D**, **Supplementary Figure 3.2C**). We conclude that Snx14$^{N}$ remains anchored at the ER following OA treatment but Snx14$^{PXCN}$ exhibits affinity for LDs and is sufficient for LD targeting.

To mechanistically dissect how the Snx14 C-terminal region interacts with LDs, we generated fragments encoding only the PX domain (Snx14$^{PX}$) and C-Nexin domain (Snx14$^{CN}$) and monitored their sub-cellular localizations. Interestingly, Snx14$^{CN}$ was sufficient to bind LD surfaces whereas Snx14$^{PX}$ was cytosolic (**Figure 3.2D**, **Supplementary Figure 3.2C**). Since hydrophobic and amphipathic helices (AHs) have been shown to mediate binding to LD surfaces in previous studies (Prevost et al. 2018), we analyzed the C-Nexin region and identified one putative AH region (**Figure 3.2B**). Strikingly, deletion of this AH region from both the C-terminal fragment (Snx14$^{PXCN\Delta H}$) and full length Snx14 (Snx14$^{FL\Delta H}$) attenuated LD association following OA treatment (**Figure 3.2D**, **Supplementary Figure 3.2C**). Collectively, we conclude that Snx14 localizes to ER-LD contacts by remaining anchored in the ER with its N-terminal region and binding the LD surface with a C-terminal AH region present in its C-Nexin domain.
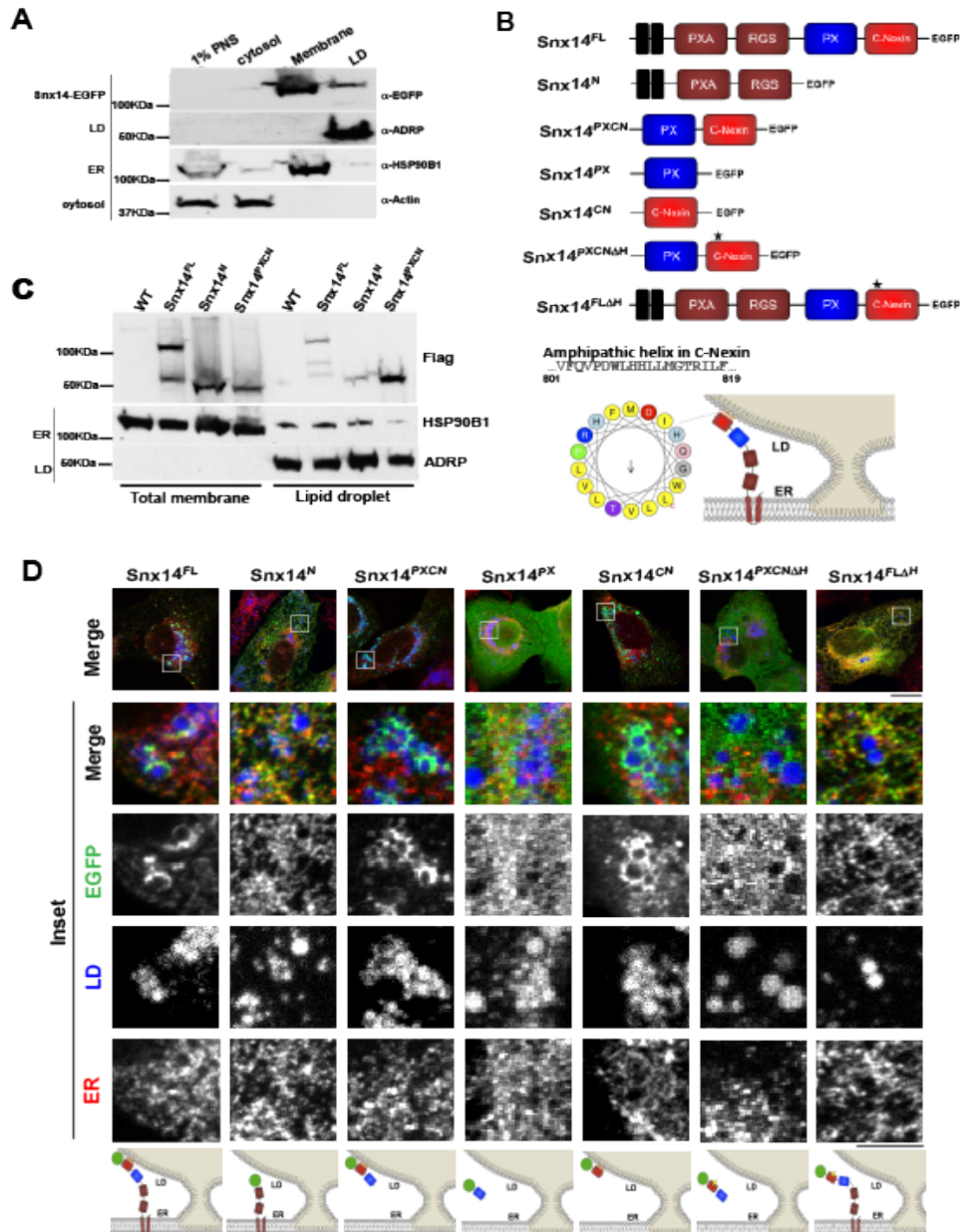
**Figure 3.2 Snx14 is topologically anchored in the ER and interacts with LDs *in trans***

**A.** LD floatation assay of OA-treated U2OS cells expressing Snx14[EGFP]. Lanes indicate Post-nuclear supernatant (PNS, 1%), cytosol (cyt, 1%), total membrane (Mem, 10%) and lipid droplet float (LD, 25%) fractions.

**B.** Schematic diagram of Snx14 fragment constructs tagged with EGFP. Snx14[FL] depicts the full length human Snx14. Snx14[N] is the N-terminal fragment from the start that includes PXA and RGS domains. Snx14[PXCN] includes the PX domain and C-Nexin domains. Snx14[PX] consists of PX and Snx14[CN] represents C-Nexin domain. An amphipathic helix in the C-Nexin domain is identified as depicted in the schematic diagram. Snx14[PXCNΔH] indicates the PX and C-Nexin domain from which the AH is deleted. Snx14[FLΔH] depicts the full length Snx14 with AH deletion.

**C.** Western blot showing distribution of Snx14[FL], Snx14[N] and Snx14[PXCN] tagged with 3XFlag among total membrane and LD fractions following OA treatment.

**D.** U2OS cells transfected with Snx14[FL], Snx14[N], Snx14[PXCN], Snx14[PX], Snx14[CN], Snx14[PXCNΔH] and Snx14[FLΔH] respectively and treated with OA for 16 hours. Co-Immunofluorescent staining with α–EGFP (green) and α-HSP90B1 (ER marker, red) and LDs stained with MDH (blue) and imaged by confocal microscopy. Scale bar = 20µm. Inset scale bar = 5 µm. Cartoons represent the localization of the respective Snx14 fragments with respect to ER and LD.
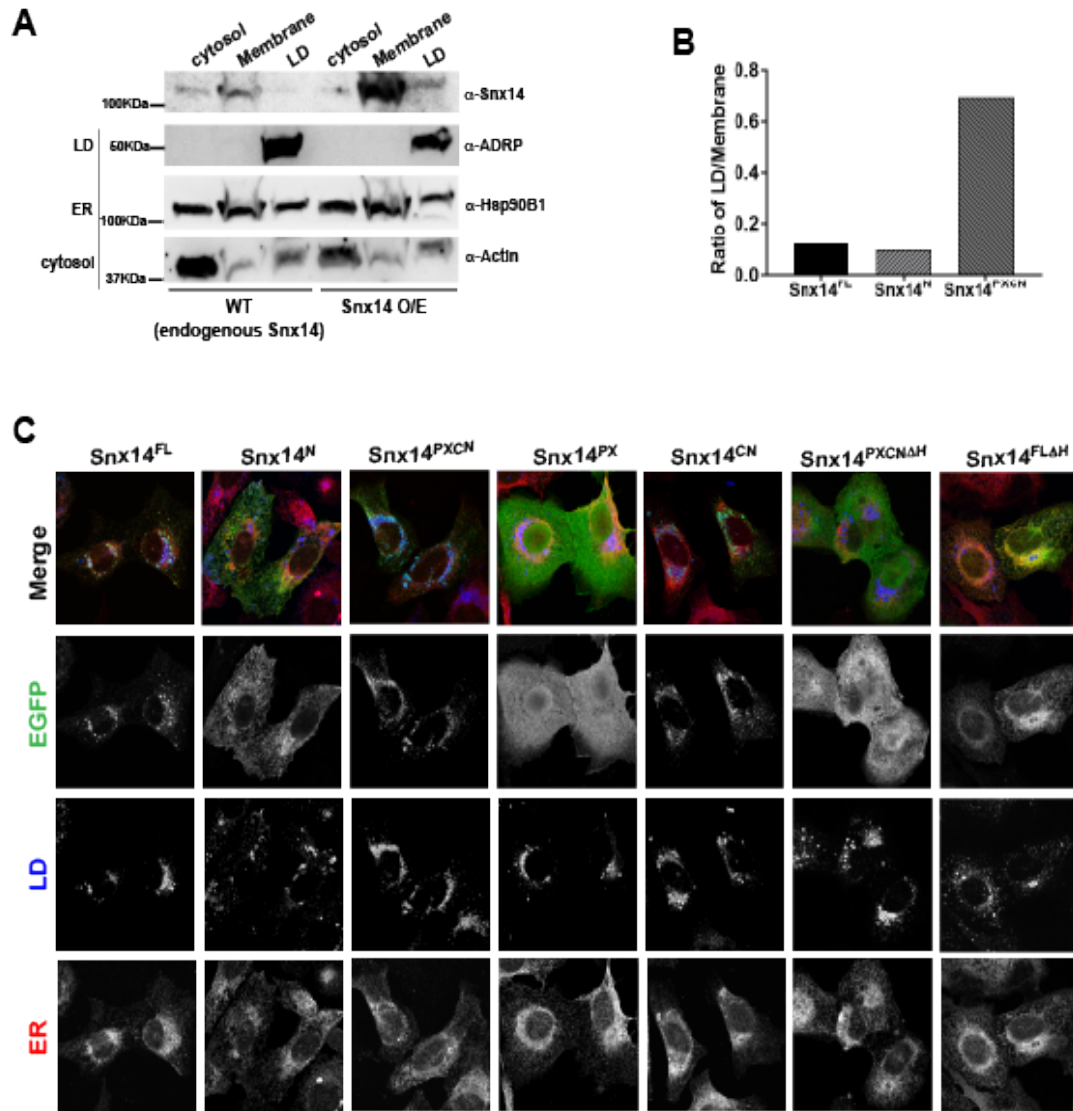
**Supplementary Figure 3.2**

**A.** Western blot with α-Snx14 antibody showing the enrichment of endogenous Snx14 in the membrane fraction similar to that in Snx14 O/E cells following OA treatment.

**B.** Quantified densitometry of bands in Figure 2C analyzed and plotted in the form of ratio of LD fraction over membrane fraction.

**C.** Larger field of view of Figure 2D showing localization of different Snx14 fragments. Scale bar = 50 μm.

**Loss of *SNX14* alters LD morphology following OA treatment**

Since ER-LD contacts have been proposed to regulate the flux of lipids into LDs during their expansion, we next evaluated whether loss of Snx14 would disrupt proper LD maturation following OA treatment. We generated *SNX14* homozygous knockout (*SNX14-KO*) U2OS cells using CRISPR/Cas9 technology with sgRNA that targeted the first exon of the *SNX14* ORF, resulting in deletion of several bases and an inserting base 'A', which led to the formation of a stop codon after 25 amino acids (**Supplementary Figure 3.3A**). We confirmed that this CRISPR indel resulted in loss of Snx14 polypeptide by Western blot (**Supplementary Figure 3.3B**). To determine whether loss of *SNX14* affected OA-induced LD maturation, we treated WT and *SNX14-KO* cells for ~16 hours with OA to induce LD expansion, and imaged LDs by staining them with the fluorescent dye monodansylpentane (MDH). As expected, WT cells exhibited many LDs that were densely clustered near the nucleus. In contrast, *SNX14-KO* cells displayed heterogeneous LDs of varying size and sub-cellular distribution (**Figure 3.3A**). Due to the limited resolution of individual LDs by light microscopy, we calculated the total LD area per cell, which is indicative of both LD number and size. Indeed, quantification revealed that *SNX14-KO* cells contained significantly less total LD area per cell, suggesting a defect in some aspect of LD homeostasis (**Figure 3.3B**).

To evaluate LD morphologies with better resolution, we next conducted thin-section TEM imaging of OA-treated cells. Similar to fluorescence imaging, we observed many LDs in WT cells of various sizes (**Figure 3.3C**). Quantification of the cross-sectional areas of ~900 LDs revealed a broad distribution of LD sizes, although ~55% of all LDs in WT cells ranged in size between $0.125\mu m^2$ to $0.4\mu m^2$ (**Figure 3.3C,D, Supplementary Figure 3.3C,D'**). In contrast, *SNX14-KO* cells contained fewer and more sparsely distributed LDs that were also more heterogeneous in size and exhibited a more bimodal size distribution (**Figure 3.3C, D**, **Supplementary Figure 3.3C**). Indeed, only ~10% of LDs in *SNX14-KO* cells were between $0.125\mu m^2$ to $0.4\mu m^2$ in size (**Supplementary Figure 3.3C, D'**). In fact, most LDs in *SNX14-KO* cells were very small (~78% $<0.125\mu m^2$ compared to ~44% in WT cells), although the proportion of large LDs ($>0.4\mu m^2$) also increased in *SNX14-KO* cells (~14% compared to only ~2% in WT) (**Supplementary Figure**

**3.3C, D, D''**). We conclude that loss of *SNX14* causes alterations in LD morphology following OA treatment, with a substantial increase in the proportion of very small and large LDs.

To confirm that the changes in LD morphologies were due to loss of Snx14, we re-introduced either full length Snx14 or Snx14 fragments back into *SNX14-KO* cells and monitored whether these constructs could rescue LD morphology. Whereas Snx14$^{FL}$ localized to ER-LD contacts and could restore the LD morphology defects, Snx14$^{N}$ remained in the ER network and did not rescue, suggesting that LD targeting is required for Snx14 function (**Figure 3.3E, F**). Similarly, a full-length version of Snx14 which lacked the AH region present in the C-Nexin domain also failed to localize to ER-LD contacts and could not functionally rescue LD morphology (**Figure 3.3E, F**). This indicates that Snx14's localization to ER-LD contacts via this AH region is required for Snx14 function. Surprisingly, expression of Snx14$^{PXCN}$ was sufficient to restore LD morphology. However, Snx14$^{PXCN}$ required its LD targeting region to rescue, as a mutant fragment not containing the AH (Snx14$^{PXCN\Delta H}$) could not rescue LD morphology (**Figure 3.3E, F**). Altogether, these results indicate that loss of Snx14 perturbs LD morphology, and Snx14 requires LD targeting via its C-terminal AH region for function.

Next, we examined whether loss of *SNX14* altered the incorporation of OA into TAG. WT and *SNX14-KO* cells were fed OA, collected at 2-hour time intervals, and their lipids extracted and evaluated by thin layer chromatography (TLC). As expected, TLC revealed a gradual increase in TAG and corresponding decrease in free fatty acids (FFA) following OA treatment (**Supplementary Figure 3.3E**). Surprisingly, loss of *SNX14* did not significantly affect TAG levels at any time point (**Supplementary Figure 3.3E, F**). Similarly, we did not detect significant alterations in cholesterol nor cholesterol-ester levels in *SNX14-KO* cells, collectively suggesting that loss of Snx14 primarily affects LD morphology (**Supplementary Figure 3.3F', F''**). Given the clear LD morphological changes, it is possible that some neutral lipids are not properly transported from the ER into LDs during their formation. Alternatively, the increase in very small and very large LDs in *SNX14-KO* cells may mean the LD population has become more bi-modal in size but retained similar total lipid levels.
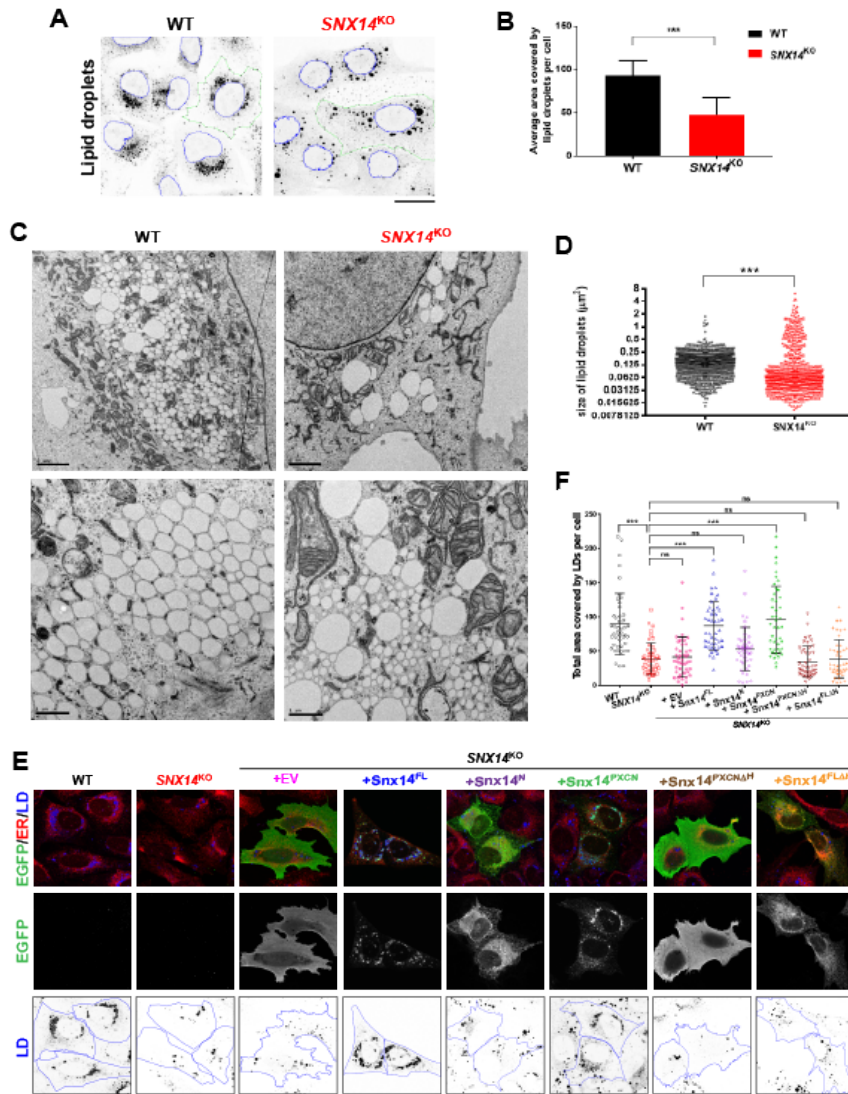
**Figure 3.3 Loss of Snx14 perturbs LD size and morphology but does not change neutral lipid levels**

A. Confocal micrographs of WT and *SNX14-KO* cells treated with OA overnight. LDs visualized by Nile Red (black) and nucleus stained with DAPI (blue outline). LDs were grayscaled and inverted. Scale bar = 25µm.
B. Quantification of average area covered by LDs per cell of representative images from A. Total LD area was derived from more than 5 fields of view, each consisting of approx. 5 cells or more of 2 different sets of experiments (total no. of cells >75, **$p<0.001$ multiple t-test by Holm-Sidak method with alpha = 0.05).
C. TEM micrographs of WT and *SNX14-KO* cells treated with OA overnight to visualize LD distribution and morphology. The top panels are lower magnification (scale bar = 2µm). The bottom panels are higher magnifications (scale bar = 1µm).
D. Scatter dot plot of cross-sectional areas of LDs in WT and *SNX14-KO* cells as in panel C. (Total LDs = 896, ***$p<0.0001$, Kolmogorov-Smirnov D test with alpha = 0.05)
E. Rescue of LD morphology in *SNX14-KO* cells by re-addition of empty vector (EV), Snx14$^{FL}$, Snx14$^{N}$, Snx14$^{PXCN}$, Snx14$^{PXCN\Delta H}$ and Snx14$^{FL\Delta H}$ respectively, all tagged with EGFP. Cells were co-IF stained with α-EGFP (green), α-HSP90B1 (ER, red) and LDs stained with MDH (blue) and imaged with confocal microscope. Scale bar = 50 µm.
F. Area covered by LDs in each cell from E analyzed and plotted. Total no. of cells quantified are 45 from two different sets of experiments (***$p<0.0001$, one-way ANOVA with alpha = 0.05). Line bars indicate mean ± SD.

52
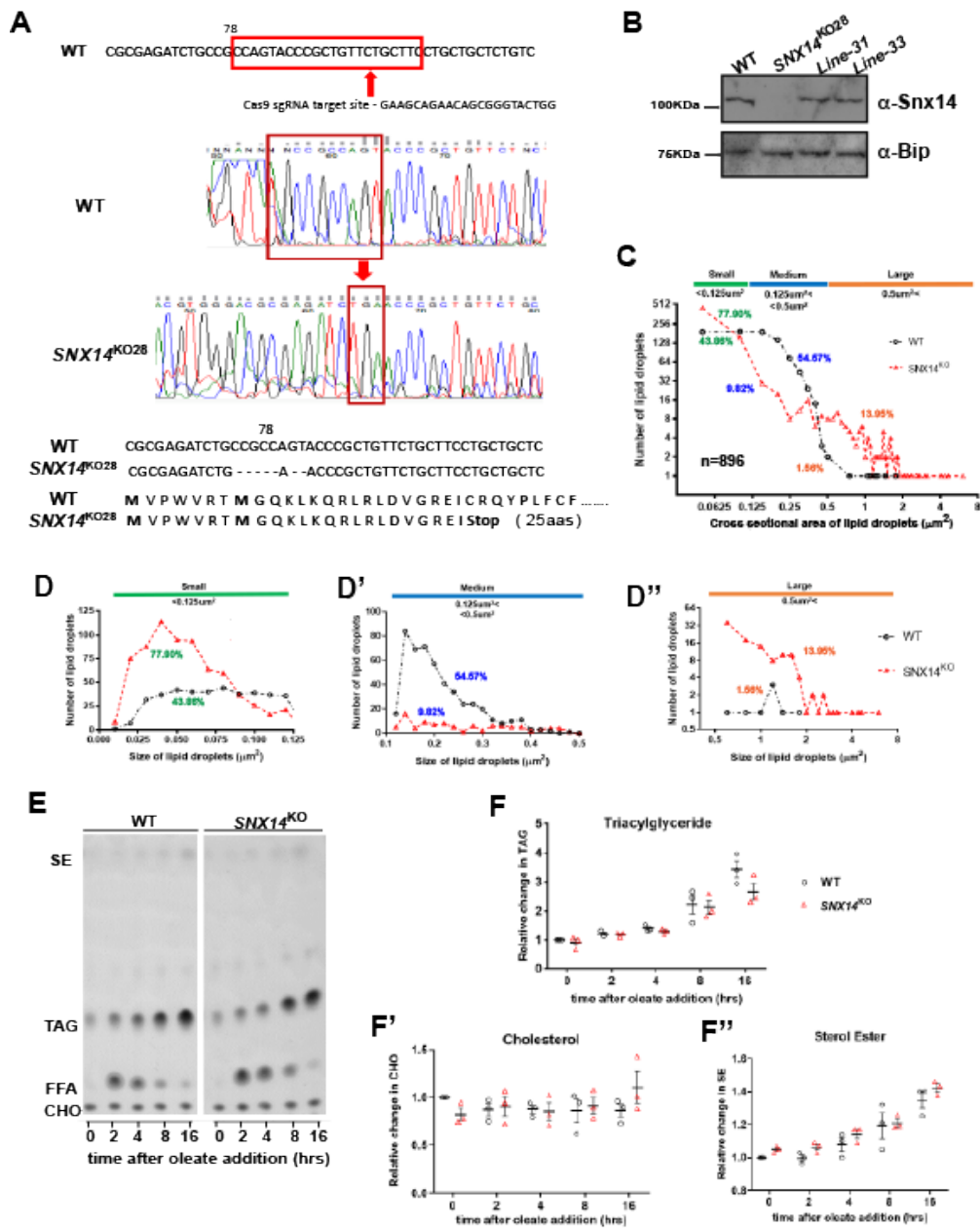
**Supplementary Figure 3.3**

A. Schematic diagram of generation of *SNX14* homozygous knockout (*SNX14-KO*) U2OS cells using CRISPR/Cas9 technology. The sgRNA was designed to target the first Exon of the *SNX14* ORF, resulting in deletion of several bases and an inserting base 'A' that lead to the formation of a stop codon after 25 amino acids.

B. WB with α-Snx14 of WT and *SNX14-KO* clonal line 28. Candidate lines (line-31 and 33) shown Snx14 was not targeted.

C. The frequency of LD distributions by their cross sectional areas in WT and *SNX14-KO* cells as quantified from C (n=896). The LD size ranges were grouped into small (size<0.125μm²; green bar), medium (0.125μm²<size<0.5μm²; blue bar) and large (size>0.5μm²; orange bar) LDs.

D. The frequency distribution of the area of small LDs <0.125μm² in WT and *SNX14-KO* cells. D'. The frequency distribution of the area of medium-sized LDs >0.125μm² and area< 0.5μm² in WT and *SNX14-KO* cells. D''. The frequency distribution of the area of large LDs of WT and *SNX14-KO* of area >0.5μm².

E. TLC plate of neutral lipids extracted from WT and *SNX14-KO* cells treated with OA for 0, 2, 4, 8, 16 hours.

F. Quantification of relative fold-changes in triacylglycerol (TAG) (F), Cholesterol (CHO) (F') and Sterol-esters (SE) (F'') (normalized to cell pellet weight) of TLC from I. Values represent mean ± SEM.

## Snx14 expression modulates ER-LD contacts

LDs bud from the ER surface and establish and/or maintain contact with the ER to ensure proper LD growth. Since Snx14 localized at the interface between the ER and LDs, and its loss affected LD morphology, we next investigated how modulating Snx14 expression level would affect ER-LD contacts. We imaged WT, Snx14$^{EGFP-APEX2}$ over-expressing (Snx14 O/E), and *SNX14-KO* cells treated with OA overnight by thin-section TEM. Strikingly, we observed significantly enhanced ER wrapping across the surfaces of LDs in Snx14 O/E samples (**Figure 3.4A-C**). In contrast, *SNX14-KO* cells displayed mildly reduced ER-LD contacts that could be observed by TEM (Figure 4A, C). Indeed, after plotting the distribution of ER-LD contacts normalized to LD size, we observe a significant increase in the ER-LD contact size in Snx14 O/E cells, and a significant decrease in *SNX14-KO* cells compared to the WTs (**Figure 3.4C**). These observations are consistent with a model where Snx14 localizes to ER-LD contacts and tethers these organelles together, so that increasing the Snx14 tether abundance enhances their contact.
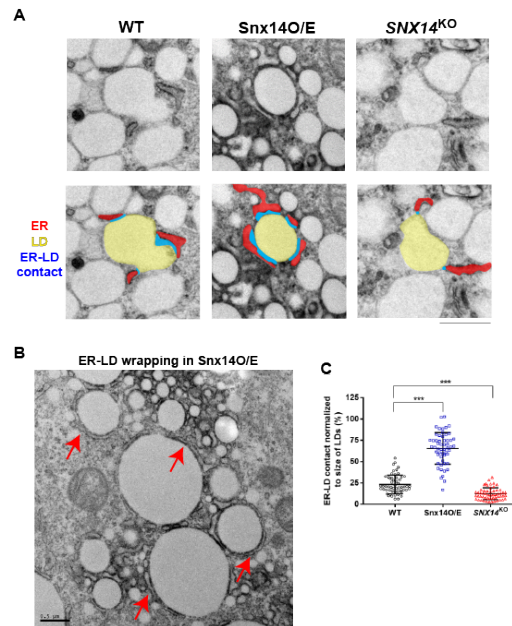


**Figure 3.4. Snx14 expression modulates ER-LD contacts following OA addition**
A. TEM images showing the extent of ER-LD contacts in WT, over-expressing Snx14$^{EGFP-APEX2}$, and *SNX14-KO* cells treated with OA overnight. LDs are colored in yellow, ER in red and the contact between ER-LD is depicted in blue.
B. ER-LD wrapping indicated by red arrows in Snx14$^{EGFP-APEX2}$ cells.
C. Quantification of the length of ER-LD contact normalized to circumference of the LDs in the form of box plot in WT, Snx14$^{EGFP-APEX2}$ and *SNX14-KO* cells (n=55, ***p<0.001, Welch's t-test with alpha = 0.05).

## Snx14 functions independently of Seipin at ER-LD contacts

The enrichment of Snx14 at ER-LD contacts, as well as the defects in LD morphology observed in *SNX14-KO* cells appeared reminiscent of recent studies on the protein Seipin. Seipin has been shown to localize to ER-LD contacts, and is required for the proper maturation of nascent LDs into mature LDs following OA treatment (Fei et al. 2008; Szymanski et al. 2007; Wang et al. 2016; Salo et al. 2016). Furthermore, loss of Seipin leads to defects in LD morphology in yeast, insect, and mammalian cells. However, overall TAG levels are largely unaltered in *SEIPIN*$^{KO}$ cells, similar to loss of Snx14. Since Seipin has also been proposed to be an ER-LD tether, we next investigated the functional relationship between Snx14 and Seipin.

First, we evaluated whether Seipin is required for Snx14 to localize to ER-LD contacts. We ectopically expressed Snx14$^{EGFP}$ in SUM159 *SEIPIN*$^{KO}$ cells, and observed that Snx14$^{EGFP}$ could still target to LDs following OA treatment (**Figure 3.5A**, **Supplementary Figure 3.5A**). During these experiments, we noted that ectopic expression of Snx14$^{EGFP}$ was unable to rescue the LD morphology defects present in *SEIPIN*$^{KO}$ cells (**Figure 3.5B, C**). To further investigate this functional relationship, we ectopically expressed mCherry-tagged Seipin in U2OS *SNX14-KO* cells. Similarly, ectopic expression of Seipin$^{mCherry}$ was unable to rescue the LD morphology defects observed in *SNX14-KO* cells, although LD area per cell was mildly different compared to *SNX14-KO* alone (**Figure 3.5D, E**). We also depleted both proteins together, but did not observe a cumulative effect on LD morphology when we siRNA depleted Snx14 in *SEIPIN*$^{KO}$ cells (**Supplementary Figure 3.5B, C**).

Finally, we monitored the sub-cellular localization of both Snx14$^{EGFP}$ and Seipin$^{mCherry}$ when co-expressed. Over-expression of Seipin$^{mCherry}$ caused it to localize evenly across the ER network in WT cells which was different than the punctate distribution shown near LDs in previous endogenous labeling studies (Salo et al. 2016; Wang et al. 2016). The distribution of Seipin$^{mCherry}$ was not altered in *SNX14-KO* cells (**Figure 3.5F**). However, we observed an enrichment of Seipin$^{mCherry}$ at Snx14$^{EGFP}$ positive ER-LD contacts when we co-expressed the two proteins together (**Figure 3.5F**). Collectively, we conclude that Seipin and Snx14 both accumulate at ER-
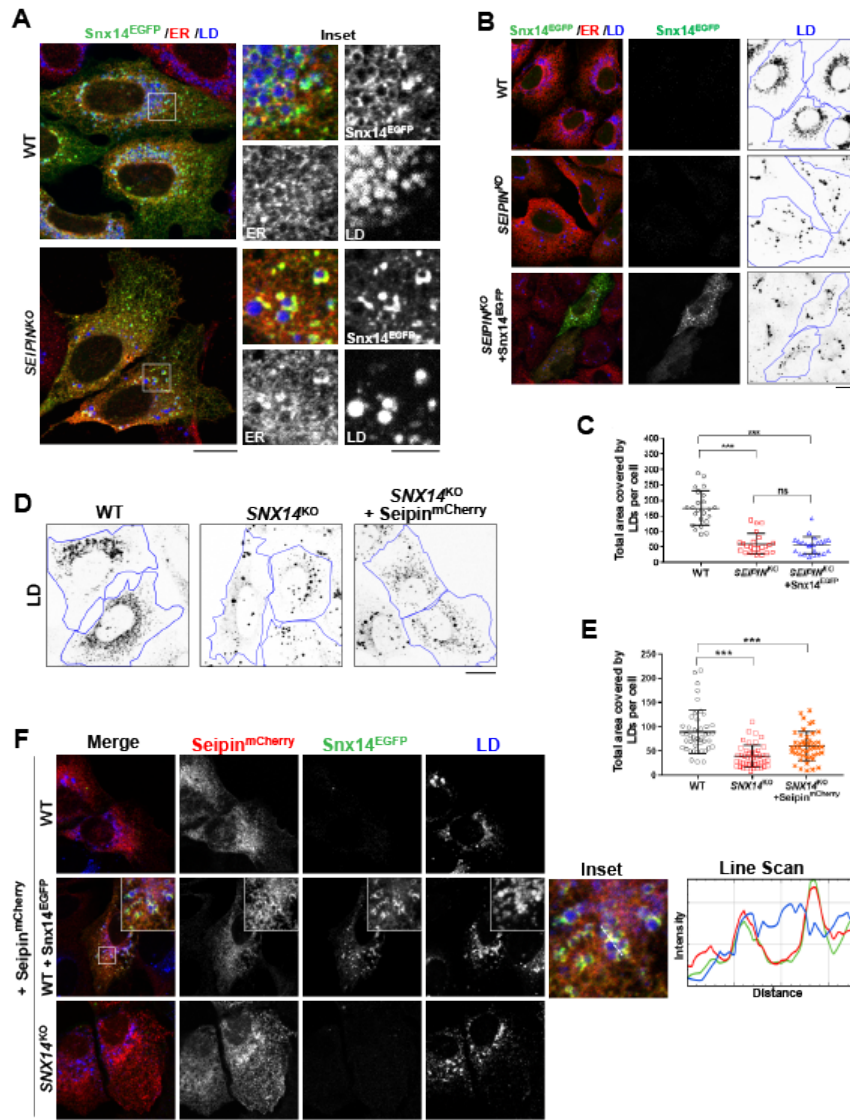
**Figure 3.5 Snx14 functions independently of ER-LD protein, Seipin**

**A.** Confocal micrographs showing localization of Snx14 in WT and *SEIPIN*$^{KO}$ SUM159 cells. The cells were transfected with Snx14$^{EGFP}$ and treated with OA overnight. Labels were Snx14$^{EGFP}$ ($\alpha$–EGFP), ER ($\alpha$-HSP90B1), and LDs (MDH). Scale bar = 20 μm. Inset scale bar = 5 μm.

**B.** Rescue of LD morphology in *SEIPIN*$^{KO}$ examined by ectopic expression of Snx14$^{EGFP}$ into *SEIPIN*$^{KO}$. Labels were Snx14$^{EGFP}$ ($\alpha$–EGFP), ER ($\alpha$-HSP90B1), and LDs (MDH stained, grayscaled and inverted by ImageJ). Scale bar = 20 μm.

**C.** Area covered by LDs in each cell from B analyzed and plotted. Total no. of cells quantified are 23 from two different sets of experiments (***$p<0.0001$, one-way ANOVA with alpha = 0.05). Line bars indicate mean ± SD.

**D.** Rescue of LD morphology in *SEIPIN*$^{KO}$ examined by re-addition of Snx14$^{EGFP}$. Blue line depicts cell boundary. Black speckles represent LDs which are MDH-stained, grayscaled and inverted by ImageJ. Scale bar = 20 μm.

**E.** Area covered by LDs in each cell from D analyzed and plotted. Total no. of cells quantified are 45 from two different sets of experiments (***$p<0.0001$, one-way ANOVA with alpha = 0.05). Line bars indicate mean ± SD.

**F.** Confocal micrographs of U2OS cells to examine localization of Seipin$^{mCherry}$ in WT cells, those transfected with Snx14$^{EGFP}$ and in *SNX14-KO* cells. Cells were transfected with Seipin-mcherry and treated with OA overnight. Labels were Snx14$^{EGFP}$ ($\alpha$–EGFP), Seipin-mcherry ($\alpha$-mCherry), and LDs (MDH). Scale bar = 20 μm.

56
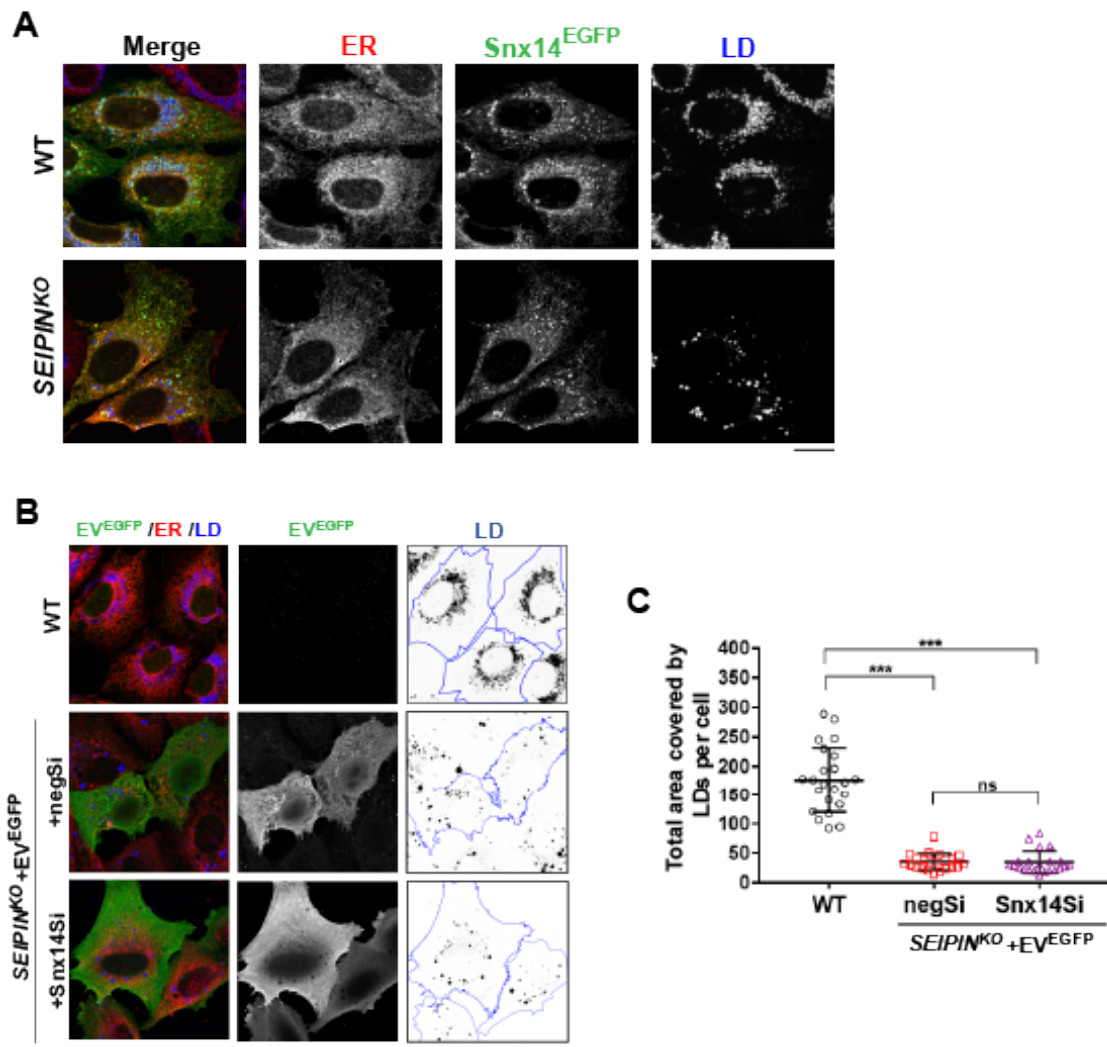
**Supplementary Figure 3.5**

A. Larger field of view of Figure 5A showing localization of Snx14 in WT and *SEIPIN*[KO] cells following OA treatment. Scale bar = 20 μm.

B. LD morphology of *SEIPIN*[KO] transfected by negSi and Snx14Si respectively and comparing to that of WT in SUM159 cells. Labels were EV[EGFP] (α–EGFP), ER (α-HSP90B1), and LDs (MDH stained, grayscaled and inverted by ImageJ). Scale bar = 20 μm.

C. Area covered by LDs in each cell from B analyzed and plotted. Total no. of cells quantified are 23 from two different sets of experiments (***$p < 0.0001$, one-way ANOVA with alpha = 0.05). Line bars indicate mean ± SD.

LD contacts and influence LD growth and morphology, but are functionally independent of one another and play unique roles in LD maturation.

**Snx14 localizes to ACSL3-associated pre-LDs during OA-induced LD expansion**

The presence of Snx14 at ER-LD interfaces following OA treatment, as well as its requirement for proper LD morphology suggested Snx14 may be recruited to pre-existing nascent LDs within the ER network to regulate LD growth following OA addition. To better dissect when and how Snx14 associates with LDs, we next monitored Snx14$^{EGFP}$ distribution in the ER during set time-points following the addition of OA and its subsequent processing and incorporation into growing LDs.

First, we fixed U2OS cells prior to the addition of OA and at 1, 2, 4, 8, and 16 hours following OA treatment, and performed co-immunofluorescence (IF) labeling of Snx14$^{EGFP}$ and the ER network, as well as stained LDs with MDH. In cells receiving less than 2 hours of OA, Snx14$^{EGFP}$ was distributed throughout the ER network with a Snx14-ER Pearson's coefficient of r=~0.4-0.6 (**Figure 3.6A, C**, **Supplementary Figure 3.6A**). Following 2 hours of OA treatment we observed a slight coalescence of Snx14$^{EGFP}$ into distinct ER-localized foci that were associated with small LDs (**Figure 6A, Supplementary Figure 3.6A**). These Snx14$^{EGFP}$ foci became more prominent by 4 hours of OA treatment, and by 8 hours there was a significant decrease in Snx14-ER co-localization as Snx14$^{EGFP}$ accumulated around growing LDs (**Figure 3.6A, C**). This Snx14 accumulation around LDs corresponded with a significant decrease of the Snx14-ER Pearson's coefficient, from r= ~0.5 at 4 hours OA to r= ~0.13 at 8 hours OA treatment (**Figure 3.6A, C**). By 16 hours of OA treatment, large LDs had appeared with Snx14 closely juxtaposed around them, and Snx14-ER colocalization was minimal.

Next, we investigated whether Snx14$^{EGFP}$ was accumulating at ER microdomains containing nascent pre-LDs by co-staining for Snx14$^{EGFP}$ and the acyl-CoA ligase ACSL3, an ER resident protein and known pre-LD marker that promotes LD expansion following OA treatment (Kassan et al. 2013). As before, we performed co-localization analysis of IF stained cells following OA treatment at 0, 1, 2, 4, 8, and 16 hours. Even prior to OA treatment we observed ACSL3 foci in

the ER network, a sub-population of which co-localized with MDH-stained LDs (**Figure 3.6B, red arrows**). However, MDH staining remained minimal, and several ACSL3 foci contained almost no detectable MDH, consistent with other studies where nascent LDs stain poorly with fluorescent dyes (Gao et al. 2017) (**Figure 3.6B, D**, **Supplementary Figure 3.6B**). In contrast, Snx14$^{EGFP}$ displayed no detectable enrichment at ACSL3-positive pre-LD sites, and exhibited no positive Pearson's coefficient value for either ACSL3 or MDH-stained LDs prior to OA addition (**Figure 3.6D, E**). Following 2 hours of OA treatment, we observed Snx14$^{EGFP}$ foci which co-localized with bright MDH-associated ACSL3 foci, along with a ~2.5-fold increase in the Snx14-ACSL3 Pearson's coefficient (Figure 6B, red arrows). This also coincided with a significant increase in the Snx14-LD Pearson's coefficient to r=~0.2 which approached the ACSL3-LD coefficient for this time point (**Figure 3.6D**). By 4 hours OA treatment, Snx14 and ACSL3 co-localized, and this further increased at 8 and 16 hours as Snx14$^{EGFP}$ accumulated around ACSL3-decorated LDs (**Figure 3.6B, D, E**). These results indicate that Snx14$^{EGFP}$ does not detectably associate with ACSL3-positive pre-LDs under ambient conditions, but is recruited to the ER-LD interface following OA treatment during LD growth.

Since Snx14$^{EGFP}$ was accumulating at ACSL3-positive LD buds, we next asked whether loss of Snx14 or ACSL3 impacted the recruitment of one another to LDs. First, we stained for endogenous ACSL3 in WT and *SNX14-KO* cells. Loss of Snx14 did not affect ACSL3 localization, and ACSL3 was detected on LD surfaces following OA treatment (**Figure 3.6F**). In contrast, siRNA depletion of ACSL3, which decreased LD abundance, also perturbed the association of Snx14$^{EGFP}$ with the remaining LDs following OA treatment, indicating that ACSL3 is necessary for Snx14$^{EGFP}$ accumulation at ER-LD contacts (**Figure 3.6G**). Collectively, we conclude that ACSL3 functions upstream of Snx14 and is required for the recruitment of Snx14 to pre-LDs during OA-induced LD growth.
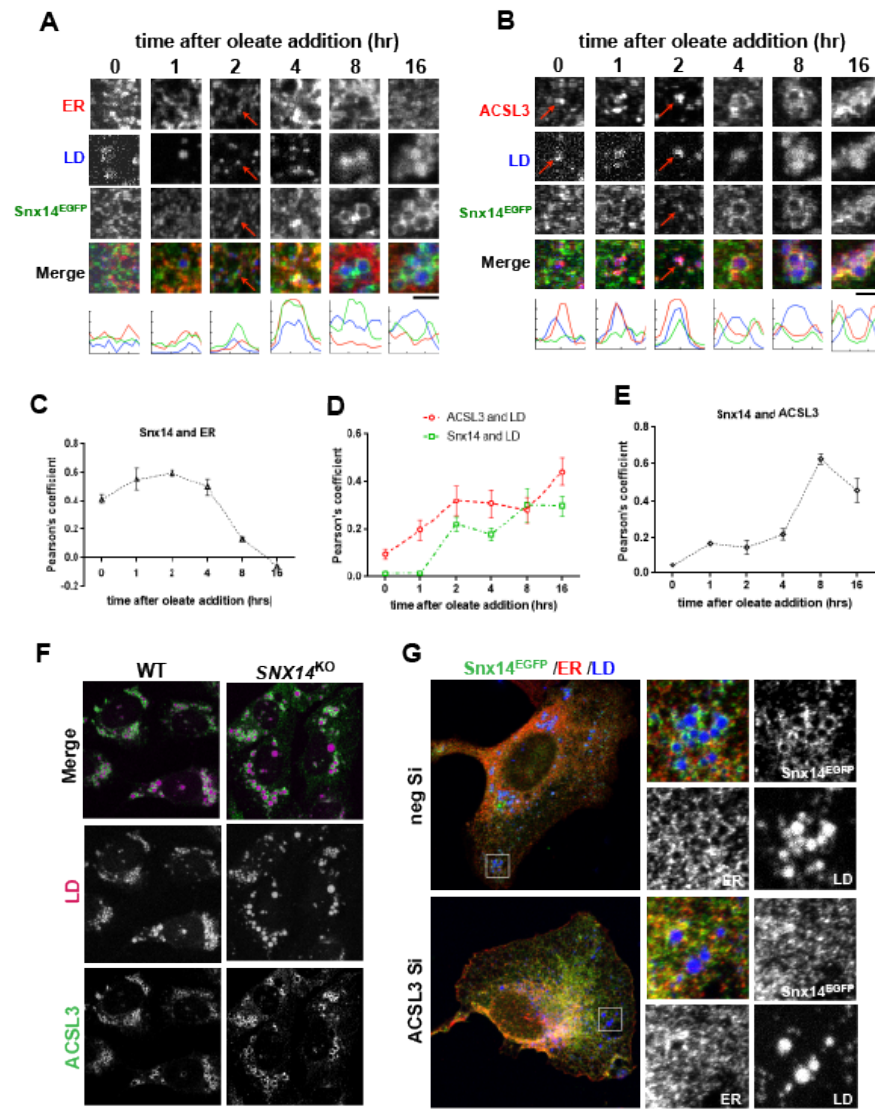
**Figure 3.6 Snx14 localizes at ACSL3-positive pre-LDs following OA addition**

**A.** Confocal micrographs of immuno-fluorescently stained Snx14$^{EGFP}$ expressing cells following OA treatment for t=0, 1, 2, 4, 8, 16 hours. Labels were Snx14$^{EGFP}$ ($\alpha$–EGFP), ER ($\alpha$-HSP90B1), and LDs (MDH). Scale bar = 2μm. Line scans show the spatial distribution of Snx14 (green) with respect to ER (red) and LDs (blue).

**B.** Confocal micrographs of immuno-fluorescently stained Snx14$^{EGFP}$ expressing cells following OA treatment for t=0, 1, 2, 4, 8, 16 hours. Labels were Snx14$^{EGFP}$ ($\alpha$–EGFP), native ACSL3 ($\alpha$-ACSL3), and LDs (MDH). Scale bar = 2μm. Line scans show the spatial distribution of Snx14 (green) with respect to ACSL3 (red) and LDs (blue). Scale bar = 2μm.

**C.** Quantification of Pearson's coefficient between Snx14 and ER of n=~20 cells depicted in panel A.

**D.** Quantification of Pearson's coefficient between ACSL3 and LDs, and Snx14 and LDs of n=~20 cells depicted in panel C.

**E.** Quantification of Pearson's coefficient between Snx14 and ACSL3.

**F.** Confocal micrographs examining localization of ACSL3 in WT and *SNX14-KO* cells treated with OA overnight. Labels were native ACSL3 ($\alpha$-ACSL3, green) and LDs (MDH, magenta). Scale bar = 20 μm.

**G.** Confocal micrographs to examine localization of Snx14 in WT cells treated with negative scrambled siRNA (neg Si) and ACSL3-targeted siRNA (ACSL3 Si) respectively. The cells were transfected with Snx14$^{EGFP}$ along with the respective siRNAs and treated with OA overnight. Labels were Snx14$^{EGFP}$ ($\alpha$–EGFP), ER ($\alpha$-HSP90B1), and LDs (MDH). Scale bar = 20 μm. Inset scale bar = 5 μm.
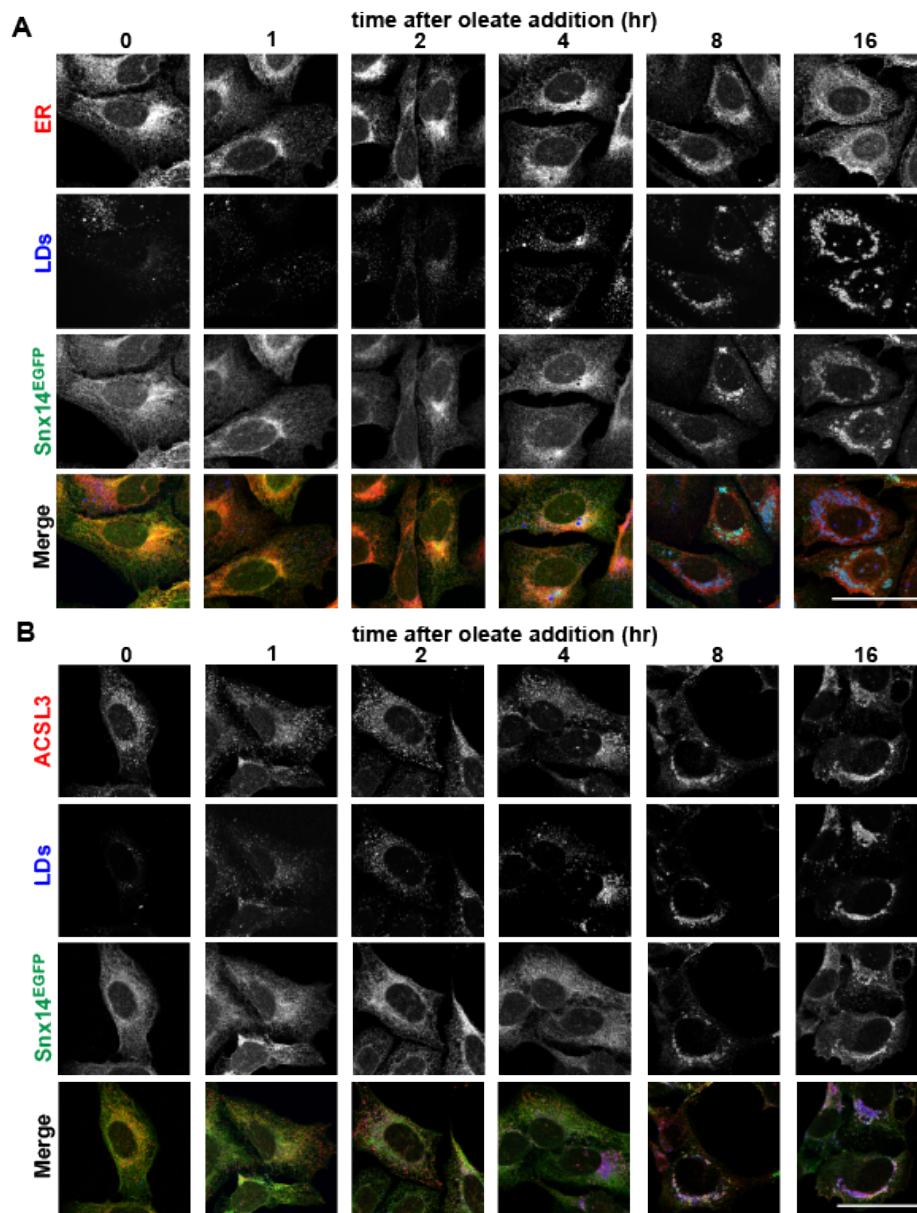
**Supplementary Figure 3.6**

**A.** Immuno-fluorescent staining of U2OS cell lines stably expressing Snx14$^{EGFP}$ at set time points (t=0, 1, 2, 4, 8, 16 hours) following OA addition. Labels were Snx14$^{EGFP}$ ($\alpha$–EGFP), the ER ($\alpha$-HSP90B1), and LDs (MDH) and imaged by confocal microscopy. Scale bar = 10μm.

**B.** Immuno-fluorescent staining of U2OS cell lines stably expressing Snx14$^{EGFP}$ at set time points (t=0, 1, 2, 4, 8, hours) following OA addition. Labels were Snx14$^{EGFP}$ ($\alpha$–EGFP), the ACSL3 ($\alpha$-ACSL3), and LDs (MDH) and imaged by confocal microscopy. Scale bar = 10μm.

**Snx14 promotes LD biogenesis following OA addition**

Since Snx14 accumulated at ACSL3-positive ER microdomains following OA treatment, we hypothesized that Snx14 may promote the incorporation of FAs into TAG during LD growth. To test this hypothesis, we ectopically over-expressed (O/E) Flag-tagged Snx14 and examined its effect on OA-stimulated LD biogenesis in U2OS cells. We used confocal microscopy to quantify the number of MDH-stained LDs formed following a brief 30-minute treatment with OA. Prior to OA treatment, Snx14 O/E cells exhibited no significant differences in MDH-stained LDs compared to WT cells (**Figure 3.7A, B**). However, following 30 minutes of OA treatment, Snx14 O/E cells exhibited a significant increase in the total number of MDH-stained LDs, suggesting excess Snx14 promoted OA-induced LD biogenesis (**Figure 3.7A, B**). To eliminate the possibility that this was due to general ER stress caused by the overexpression of Snx14[Flag], which might cause the production of LDs non-specifically, we also monitored the unfolded protein response (UPR) by examining levels of spliced XBP1 transcripts, and found no significant differences (**Supplementary Figure 3.7A,B**).

To determine whether Snx14 influenced the incorporation of FAs into TAG during LD growth, we next monitored the incorporation of a fluorescently labeled fatty acyl-CoA (NBD-palmitoyl-CoA) into TAG when it was incubated with membranes isolated from WT and Snx14 O/E cells (**Figure 3.7C**). Using this *in vitro* assay, we observed that over time NBD-palmitoyl-CoA could be incorporated with exogenously added DAG into NBD-labeled TAG, which could be visibly detected by TLC (McFie and Stone 2011). Notably, by 40 minutes of reaction time there was a significant increase in the incorporation of NBD-palmitoyl-CoA into TAG in samples derived from Snx14 O/E cells compared to WT (**Figure 3.7C, D**). We also noted an increase in the level of NBD-labeled free palmitate (NBD-FFA) (**Figure 3.7C, D'**).

Next, we determined whether Snx14 O/E also increased total TAG levels in intact cells following OA treatment. We monitored the change in TAG and FFAs by TLC in WT and Snx14 O/E cells following treatment with OA for 2, 4, 8, and 16 hour time points (**Figure 3.7E**). Indeed, Snx14
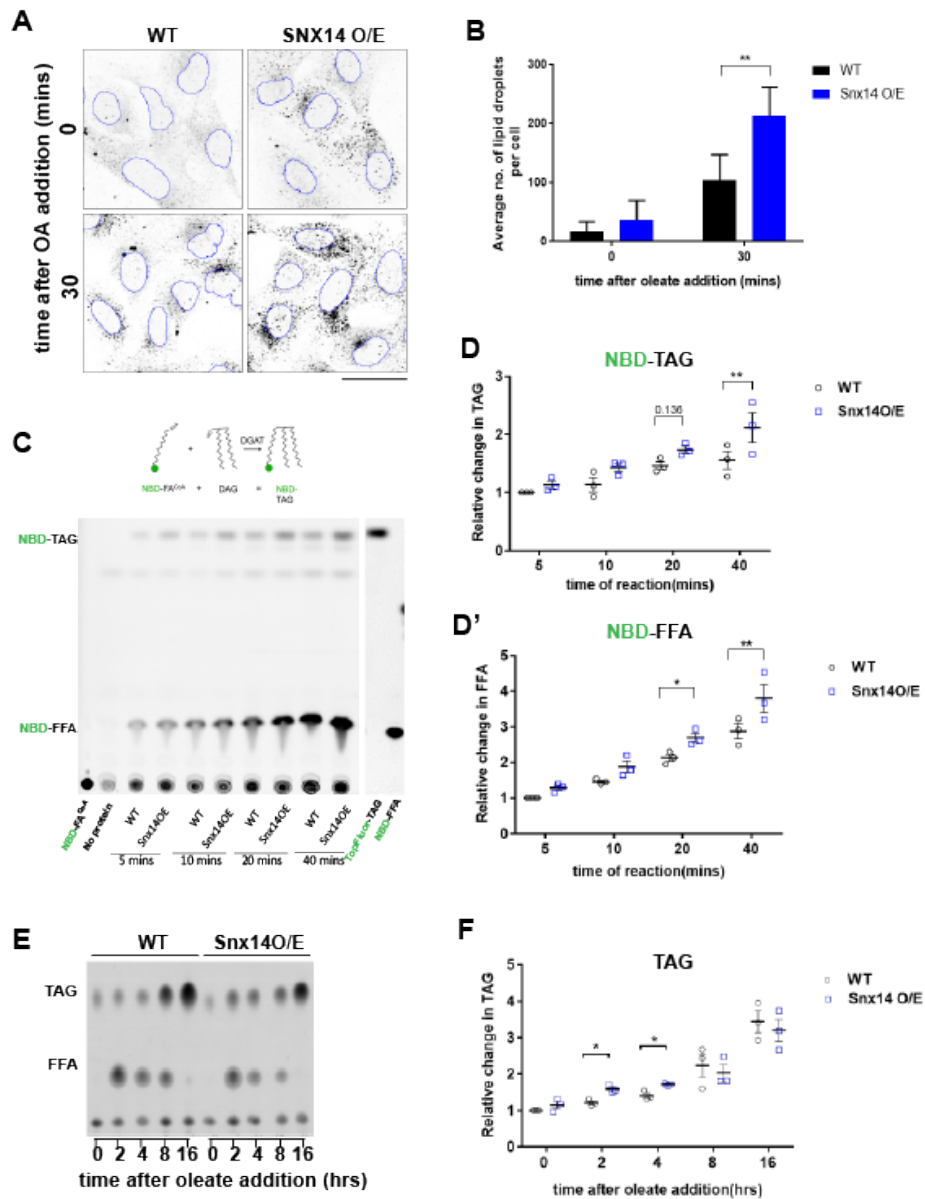
**Figure 3.7 Snx14 promote LD biogenesis and enhances TAG synthesis**

**A.** Confocal micrographs of wildtype (WT) and Snx14[Flag] over-expressing (O/E) U2OS cells either without OA or following 30mins OA treatment. LDs were labeled with Nile Red and grayscaled black. ImageJ was used to mark the border of nuclei in blue. Scale bar = 50μm.

**B.** Quantification of average number of LDs per cell of representative image from **A.** Each set of values were analyzed from 5 fields of view, each consisting more than 10 cells of 2 different sets of experiments (total no. of cells >100, **p<0.001 multiple t-test by Holm-Sidak method with alpha = 0.05).

**C.** Schematic diagram depicting fluorescent *in vitro* assay to measure NBD-FA[CoA] incorporation into NBD-TAG. TLC of fluorescent NBD-FA-CoA incorporated into neutral lipids over time. WT and Snx14[Flag] over-expressing cells were pulsed with NBD-FA-CoA and collected at 5, 10, 20 and 40 minute time-points.

**D.** Quantification of relative fold change in NBD-TAG (D) and NBD-FFA (D') (normalized to protein concentration) of TLC from C. Values represent mean±SEM (n=3, *p<0.01, multiple t-test by Holm-Sidak method with alpha = 0.05).

**E.** TLC of neutral lipids in WT cells and cells over-expressing Snx14[EGFP] treated with oleic acid for 0, 2, 4, 8, 16 hours.

**F.** Quantification of relative fold change in TAG (normalized to cell pellet weight) of TLC from B. Values represent mean±SEM (n=3, *p<0.01, multiple t-test by Holm-Sidak method with alpha = 0.05).
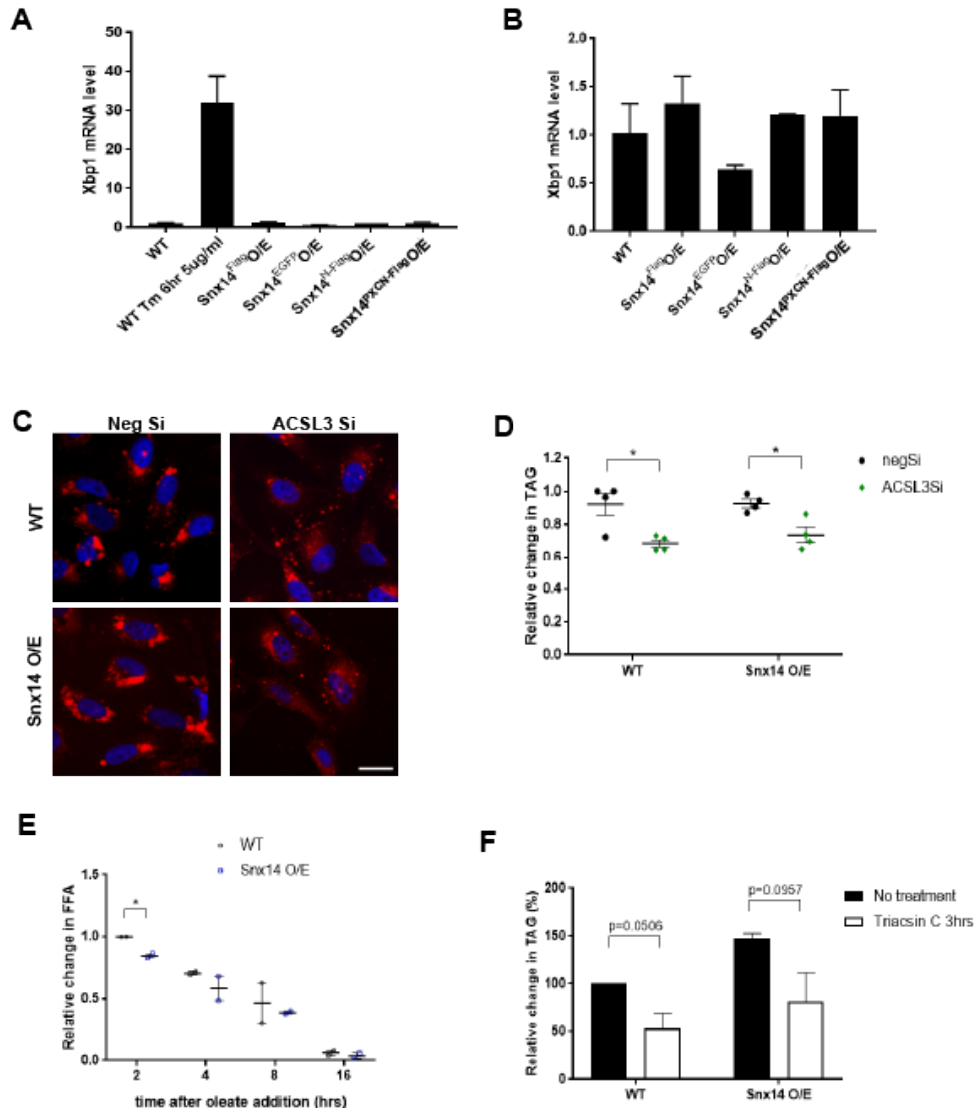
**Supplementary Figure 3.7**

A. RT-PCR data monitoring mRNA levels of spliced Xbp1, an indicator of active Unfolded Protein Response (UPR). WT Tm 6hr (5μg/mL) indicates U2OS cells treated with Tunicamycin (Tm) to induce UPR. Snx14$^{Flag}$O/E and Snx14$^{EGFP}$O/E represent stable cell lines overexpressing full length Snx14 tagged with 3XFlag and EGFP respectively. Snx14$^{N-Flag}$O/E and Snx14$^{PXCN-Flag}$O/E are the respective N-terminal and C-terminal fragments of Snx14 as depicted in Figure 2B which are overexpressed stably in the cells.

B. Zoom-in of same RT-PCR data as in panel A but omitted the Tunicamycin-treated sample.

C. U2OS cells treated with OA overnight receiving either scrambled (negative) siRNA or siRNA to reduce ACSL3 expression. Cells were stained with Nile Red (red) to label LDs and DAPI nuclear stain. Scale bar = 30μm.

D. Quantification of relative fold change in TAG (normalized to cell pellet weight) from TLC in OA-treated WT cells and cells overexpressing Snx14$^{Flag}$ and treated with neg siRNAs and ACSL3 siRNAs respectively. Values represent mean±SEM (n=4, *p<0.01, multiple t-test by Holm-Sidak method with alpha = 0.05).

E. Quantification of relative fold-change in FFA (normalized to cell pellet weight) of TLC from B. Values represent mean±SEM (n=3, *p<0.01, multiple t-test by Holm-Sidak method with alpha = 0.05).

F. Quantification of percent change in TAG in WT and Snx14$^{Flag}$ overexpressed cells when treated with Triascin C for 3 hours (n=2, t-test by Holm-Sidak method with alpha=0.05).

O/E cells exhibited mild but significantly elevated TAG levels at early time-points (2 hour and 4 hour), as well as a significant decrease in FFAs at 2 hours, coincident with the initial accumulation of Snx14 to ACSL3 positive pre-LDs observed by light microscopy (**Figure 3.7F**, **Supplementary Figure 3.7E**). To confirm that these increases in TAG were due to increased TAG biogenesis and not decreased LD turnover, we monitored TAG mobilization by treating cells with the acyl-CoA synthesis inhibitor Triacsin C for 3 hours to inhibit LD biogenesis and promote LD mobilization. We observed similar levels of TAG reduction in both WT and Snx14 O/E cell lines, suggesting LD turnover is not blocked in Snx14 O/E cells (**Supplementary Figure 3.7F**).

Finally, since ACSL3 and Snx14 co-localized at LDs following OA treatment, and Snx14 recruitment to LDs required ACSL3, we determined whether loss of ACSL3 would similarly affect TAG synthesis and LD biogenesis in WT and Snx14 O/E cells. Indeed, siRNA depletion of ACSL3 in both WT and Snx14 O/E cells similarly reduced LD numbers and TAG levels, suggesting Snx14 O/E alterations were ACSL3 dependent (**Supplementary Figure 3.7C,D**). Altogether we conclude that Snx14 promotes the incorporation of OA into TAG during OA-induced LD growth in an ACSL3-dependent manner.

**Discussion**

LD biogenesis and maturation involves distinct stages of lipid synthesis and ER membrane remodeling, and is executed by the coordinated effort of several proteins and enzymes that accumulate at ER microdomains from which LDs bud. During their initial maturation, LDs maintain contact with the ER, and this ER-LD bridge serves as a site for inter-organelle lipid flux that drives LD growth. How, when, and whether an LD will be released from the ER surface remains poorly understood, and what factors regulate the dynamics of ER-LD crosstalk remain a major question in the LD field. Recent studies have highlighted proteins such as Seipin, Rab18, and others that localize at ER-LD contacts and promote LD maturation through inter-organelle tethering (Salo et al. 2016; Wang et al. 2016; Xu et al. 2018). Here, we identify the SCAR20 disease-related protein Snx14 as a novel factor that contributes to FA-induced LD growth at ER-LD contacts. Using proximity-based APEX technology, we visualize Snx14 at ER-LD contact sites

following OA treatment, the first use of APEX imaging technology at this inter-organelle junction to our knowledge. Furthermore, we find that Snx14 remains topologically associated with the ER while at ER-LD contacts and binds LDs *in trans*. Consistent with its role as an ER-LD tether, Snx14 expression can modulate the extent of ER-LD contacts, and Snx14 O/E cells display extended ER-LD contact sites. We find with multi-time point imaging that Snx14 is not detectably present at nascent pre-LDs containing ACSL3, but is recruited to these ER sites following OA treatment as pre-LDs grow (**Figure 3.8A**).

Intriguingly, the phenotypes observed in *SNX14-KO* cells appear similar to loss of Seipin, another bridging protein that localizes to ER-LD contacts. Like Snx14, loss of Seipin perturbs LD morphology, but does not generally alter cellular TAG levels (Cartwright et al. 2015; Wang et al. 2016). Both proteins also appear to use similar mechanisms to target to ER-LD contacts (Sui et al. 2018) (Yan et al. 2018). Seipin and Snx14 both contain transmembrane helices anchored in the ER. Snx14 contains an AH region on its C-Nexin domain which is necessary for LD binding and Snx14 function. Similarly, *Drosophila* Seipin contains a hydrophobic helix in its lumenal domain and a N-terminal LD targeting region, both of which display affinity for LDs. Mutation of both these regions together perturbs Seipin function in LD formation, indicating that LD targeting by these regions is functionally important (Sui et al. 2018). Both proteins also play roles in LD maturation following OA addition. Seipin has also been reported to promote LD expansion in *Drosophila* S2 cells, as well as during adipocyte development (Pagac et al. 2016). Although further studies are required, an intriguing model is that both Seipin and Snx14 independently regulate LD maturation at the ER-LD interface by stabilizing the ER-LD bridge and helping to maintain this contact so TAG can be efficiently produced in the ER and fluxed into the growing LD (**Figure 3.8B**). Consistent with this, Snx14 over-expression promoted FA incorporation into TAG. The precise mechanism of this is unclear, but one model is that Snx14 drives the stabilization and extension of ER-LD contacts, and these contacts are sites where TAG synthesis enzymes accumulate. In the absence of Snx14, compensatory mechanisms maintain neutral lipid synthesis, but proper LD growth is perturbed.

Human Snx14 displays functional conservation with yeast Mdm1, which also localizes to specific ER microdomains (yeast NVJs) and associates with LDs as they mature there. Furthermore, both proteins work in conjunction with fatty acyl-CoA ligases at sites of LD maturation. In yeast, Mdm1 functionally interacts with fatty acyl-CoA ligase Faa1 (Hariri et al. 2018). Similarly, Snx14 co-localizes with ACSL3 in human cells, and requires ACSL3 for recruitment at ER-LD contacts, implying a conserved function in FA metabolism. However, whereas Mdm1 constitutively localizes to NVJ contact sites in yeast, human cells do not contain NVJ contacts and Snx14 displays no detectable sub-cellular localization prior to its association with growing LDs. This difference may be attributed to the different phospholipid binding properties of the two proteins' Phox homology (PX) domains. Mdm1 contains a PX domain that binds to vacuolar PI3P, thus constitutively anchoring Mdm1 to ER microdomains adjacent to the vacuole surface. In contrast, structural and biochemical studies reveal that the Snx14 PX domain lacks residues necessary for PI3P binding, and it displays negligible phospholipid binding affinity *in vitro* (Mas et al. 2014; Bryant et al. 2018). Instead, we find that Snx14 inducibly accumulates at distinct ER sub-domains marked by ACSL3 following OA treatment. Once there, Snx14 remains associated with a growing LD via a C-terminal amphipathic helix region in its C-Nexin domain. Further studies are needed to dissect these distinctions, which imply a functional divergence between Mdm1 and Snx14 regarding how they associate with different cellular organelles.

Recent studies reveal that many proteins re-target from the ER network to LDs during times of elevated TAG synthesis and LD growth. These generally include lipid synthesis enzymes that promote neutral lipid synthesis (GPAT4, DGAT2) or phospholipid synthesis (CCT1) to promote proper LD maturation (Wilfling et al. 2013). These proteins also feature LD targeting mechanisms including either a hairpin membrane insertion motif that can inter-changeably anchor in both the ER bilayer and LD monolayer (Type I) or an amphipathic helix that can insert into the LD monolayer surface (Type II) (Prevost et al. 2018). In contrast to Type I LD-targeting proteins that leave the ER, Snx14 appears to maintain its ER localization throughout LD maturation. We propose that Snx14, like Seipin, constitutes its own class of LD-associated proteins that localize to ER-LD contacts during LD growth and maturation, but remain firmly anchored in the ER while

binding the LD monolayer surface *in trans*. This allows them to act as inter-organelle tethers firmly connecting the ER and LD during LD growth, and ensuring the two organelles maintain a connection as TAG produced in the ER is fluxed into the maturing LD (**Figure 3.8**). Given its role in pediatric cerebellar ataxia SCAR20, further analysis of Snx14 will no doubt yield more interesting and surprising discoveries in cell physiology.
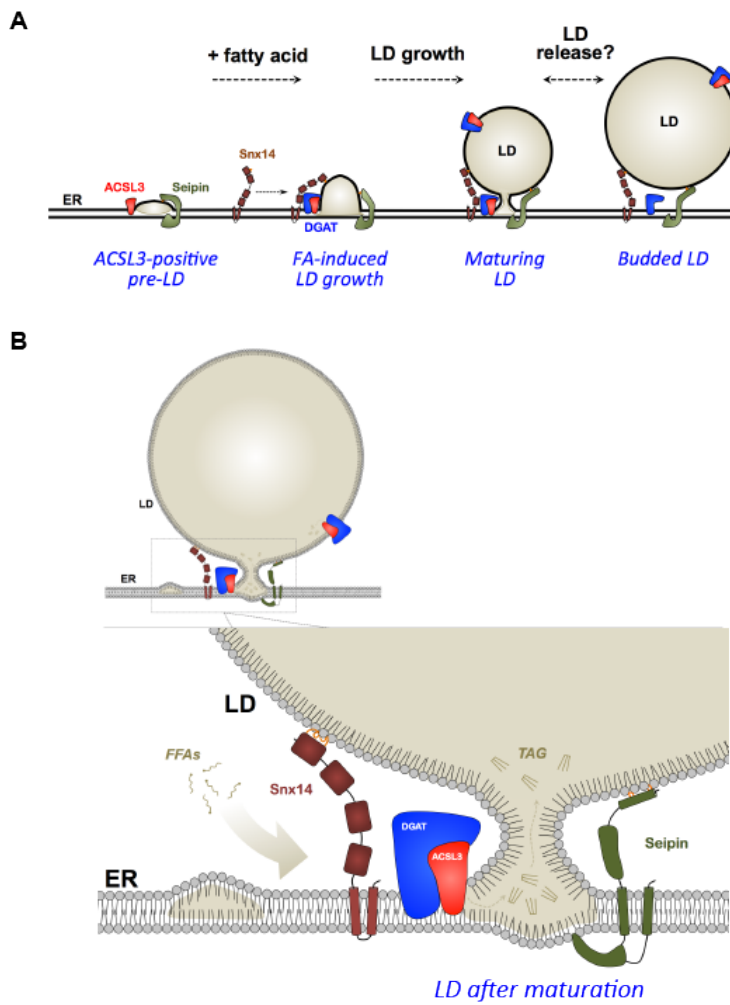


**Figure 3.8. Working Model for Snx14 in fatty acid-induced LD maturation**
A. Stepwise cartoon of FA-induced LD biogenesis promoted by Snx14.
B. Model of Snx14 and other key factors at ER-LD contact site following LD maturation.

# Snx14 proximity labeling reveals a role in saturated fatty acid metabolism and ER homeostasis defective in SCAR20 disease

## Abstract

Fatty acids (FAs) are central cellular metabolites that contribute to lipid synthesis, that can be stored or harvested for metabolic energy. Dysregulation in FA processing and storage causes toxic FA accumulation or altered membrane compositions and contributes to metabolic and neurological disorders. Saturated lipids are particularly detrimental to cells, but how lipid saturation levels are maintained remains poorly understood. Here, we identify the cerebellar ataxia SCAR20-associated protein Snx14, an endoplasmic reticulum (ER)-lipid droplet (LD) tethering protein, as a novel factor required to maintain the lipid saturation balance of cell membranes. We show that following saturated FA (SFA) treatment, the ER integrity in *SNX14-KO* cells are compromised and both *SNX14-KO* cells and SCAR20 disease patient-derived cells are hypersensitive to SFA-mediated lipotoxic cell death. Using APEX2-based proximity labeling, we reveal the protein composition of Snx14-associated ER-LD contacts and define a functional interaction between Snx14 and Δ-9 FA desaturase SCD1. Lipidomic profiling reveals that *SNX14-KO* cells increase membrane lipid saturation following exposure to palmitate, phenocopying cells with reduced SCD1 activity. In line with this, *SNX14-KO* cells manifest delayed FA processing and lipotoxicity, which can be rescued by SCD1 over-expression. Altogether these mechanistic insights reveal a role for Snx14 in FA and ER homeostasis, defects in which may underlie the neuropathology of SCAR20.

## Introduction

Cells regularly internalize exogenous fatty acids (FAs), and must remodel their metabolic pathways to process and properly store FA loads. As a central cellular currency that can be stored, incorporated into membrane lipids, or harvested for energy, cells must balance FA uptake, oxidation, and processing to maintain homeostasis. Defects in any of these processes can elevate intracellular free fatty acids which can act as detergents to damage organelles, or be aberrantly

incorporated into membranes. Excessive membrane lipid saturation can alter organelle function and contribute to cellular pathology, known as lipotoxicity (Schaffer 2003; Lelliott and Vidal-Puig 2004). Failure to properly maintain lipid compositions and storage contributes to many metabolic disorders (Ertunc and Hotamisligil 2016) including type 2 diabetes (Kusminski et al. 2009), obesity (Ye, Onodera, and Scherer 2019), cardiac failure (Borradaile and Schaffer 2005; Schaffer 2016) and various neurological diseases (Bruce, Zsombok, and Eckel 2017).

Properties of FAs such as their degree of saturation and chain length are key determinants of their fate within the cell (Estadella et al. 2013). High concentrations of saturated FAs (SFAs) in particular are highly toxic, as their incorporation into organelles affects membrane fluidity and can trigger lipotoxicity and cell death (Piccolis et al. 2019; Hetherington et al. 2016; Borradaile et al. 2006a; Listenberger et al. 2003). To prevent this, cells desaturate SFAs into mono-unsaturated FAs (MUFAs) before they are subsequently incorporated into membrane glycerophospholipids or stored as triacylglycerol (TG) in lipid droplets (LDs). LD production provides a lipid reservoir to sequester otherwise toxic FAs, providing a metabolic buffer to maintain lipid homeostasis (Fujimoto and Parton 2011; Plotz et al. 2016).

As LDs are created by and emerge from the ER network, inter-organelle communication between the ER and LDs is vital for LD biogenesis (Wilfling et al. 2013). Consequently numerous proteins that contribute to LD biogenesis, such as Seipin (Szymanski et al. 2007; Salo et al. 2019) and the diacylglyceride acyltransferase (DGAT) (Xu et al. 2012), are implicated in ER-LD crosstalk. Previously, we identified Snx14, a sorting nexin (SNX) protein linked to the cerebellar ataxia disease SCAR20 (Thomas et al. 2014; Shukla et al. 2017; Akizu et al. 2015), as a novel factor that promotes FA-stimulated LD growth at ER-LD contacts (Datta et al. 2019; Bryant et al. 2018). Snx14 is an ER-anchored integral membrane protein. During periods of elevated FA flux, Snx14 is recruited to ER-LD contact sites where it promotes the incorporation of FAs into TAG as LDs grow (Datta et al. 2019). In line with this, *SNX14-KO* cells exhibit defective LD morphology following oleate addition, implying Snx14 is required for proper FA storage in LDs. Related

studies of Snx14 homologs in yeast and *Drosophila* indicate a conserved role for Snx14 family proteins in FA homeostasis and LD biogenesis (Hariri et al. 2019; Ugrankar et al. 2019).

Despite these insights, why humans with Snx14 loss-of-function mutations develop the cerebellar ataxia disease SCAR20 remains enigmatic. Given the proposed role of Snx14 in lipid metabolism, and that numerous neurological pathologies arise through defects in ER lipid homeostasis (Blackstone, O'Kane, and Reid 2011; Yamanaka and Nukina 2018; Adibhatla and Hatcher 2008), here we investigated whether Snx14 loss alters the ability of cells to maintain lipid homeostasis in response to FA influx. Our findings indicate that Snx14-deficient cells are hypersensitive to SFA exposure, and manifest defects in ER morphology and ER-associated lipid metabolism.

**Results**

***SNX14-KO* cells are hypersensitive to saturated fatty acid associated lipotoxicity**

Previously, we showed that following oleate addition, Snx14 enriches at ER-LD contacts to promote LD growth, and Snx14 loss disrupts LD homeostasis (Datta et al. 2019). To further dissect Snx14 function in maintaining lipid homeostasis, we interrogated how *SNX14-KO* cells respond to exposure to various saturated and unsaturated FAs. We exposed wildtype (WT) or *SNX14-KO U2OS* cells to titrations of specific SFAs or MUFAs for 48 hours, and monitored cell viability using an established crystal violet assay (Feoktistova, Geserick, and Leverkus 2016; Chu et al. 2015). Exposure to MUFAs including palmitoleate (16:1) and oleate (18:1) did not perturb cell viability of either WT or *SNX14-KO* cells even at 1000μM concentrations (**Figure 4.1 A, A'**). In contrast, treatment of WT cells with increasing concentrations of SFAs such as palmitate (16:0) or stearate (18:0) resulted in decreased cell survival, as previously reported (Listenberger et al. 2003; Spigoni et al. 2017) (**Figure 4.1 B, B'**).

Intriguingly, *SNX14-KO U2OS* cells were hyper-sensitive to SFA-induced death compared to WT cells (**Figure 4.1 B, B'**). The concentration of palmitate at which ~50% of WT cells survive is ~1000μM, but only ~500μM for *SNX14-KO* (**Figure 4.1B**). Similarly, exposure to ~600μM stearate resulted in ~50% cell viability for WT cells, but only required ~300μM for *SNX14-KO*

(**Figure 4.1B'**). Consistent with this, SCAR20 patient-derived fibroblasts (Bryant et al. 2018; Thomas et al. 2014) which are homozygous for loss-of-function Snx14 mutations exhibited significantly reduced cell viability compared to control fibroblasts following palmitate addition (**Figure 4.1C**). SCAR20 patient cells reached ~50% viability at ~1000μM palmitate exposure whereas more than 50% WT cells were viable even at 2000μM palmitate treatment. Collectively, these observations indicate that Snx14-deficient cells are hyper-sensitive to SFA exposure.

Once internalized, free FAs (FFAs) are esterified and shunted into several distinct metabolic fates, including their incorporation into ceramides (Turpin et al. 2006), glycerophospholipids (Ellingson, Hill, and Lands 1970), or neutral lipids (Bell and Coleman 1980). They can also be harvested by catabolic breakdown in oxidative organelles such as mitochondria (Lelliott and Vidal-Puig 2004). To begin to dissect why *SNX14-KO* cells were hyper-sensitive to SFAs, we conducted a systemic analysis of each FA-associated pathway. Since intracellular ceramide accumulation can itself be toxic (Turpin et al. 2006), we tested whether pharmacologically lowering ceramide synthesis could rescue *SNX14-KO* SFA-associated toxicity. We treated cells with myriocin, which inhibits the SPT complex that incorporates palmitate into newly synthesized ceramides (Piccolis et al. 2019). Myriocin treatment did not rescue *SNX14-KO* SFA hypersensitivity, suggesting that elevated ceramides do not contribute to *SNX14-KO* palmitate-induced cell death (**Figure 4.1D**). Next, we examined whether mitochondrial FA oxidation was required for *SNX14-KO* hypersensitivity by treating cells with etomoxir that inhibits mitochondrial FA uptake (Schrauwen et al. 2010; Haffar, Berube-Simard, and Bousette 2015). This did not suppress palmitate-induced lipotoxicity in *SNX14-KO* cells, indicating perturbed mitochondrial FA oxidation is likely not causative of Snx14-associated lipotoxicity (**Figure 4.1E**).
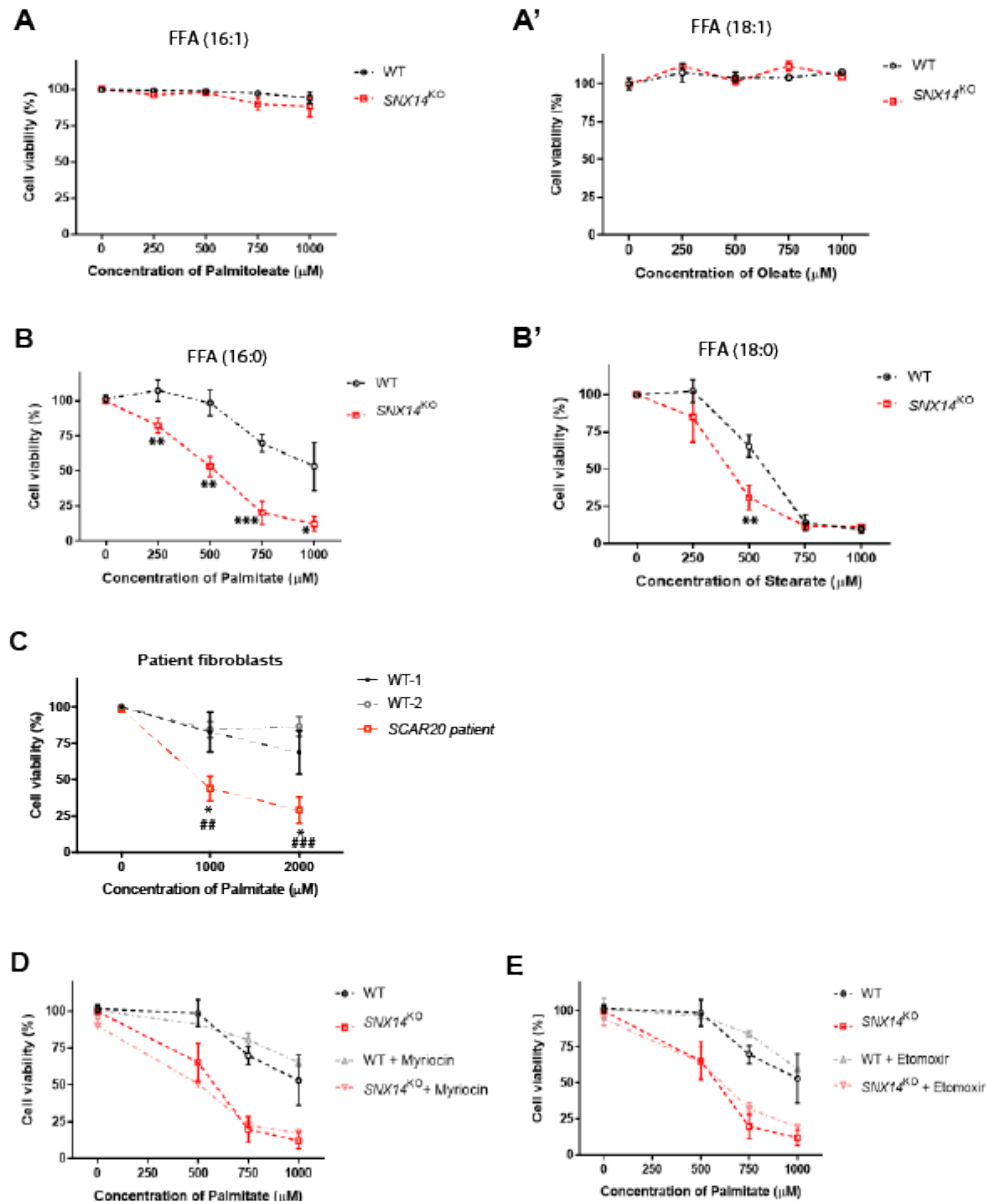
**Figure 4.1: Snx14 deficient cells are hypersensitive to saturated fatty acids**

A. Cell viability (%) of WT and *SNX14-KO* cells, following treatment with increasing concentration (0, 250, 500, 750, 1000µM) of palmitoleate (FA|16:1) for 2 days. **A'.** Treatment of WT and *SNX14-KO* cells with similar increasing concentration of oleate (FA|18:1) for 2 days. Values represent mean±SEM.

B. Cell viability (%) of WT and *SNX14-KO* cells, showing *SNX14-KO* cells are hypersensitive to (0, 250, 500, 750, 1000µM) of palmitate (FA|16:0) treatment for 2 days. **B'**. Exposure to similar concentration of stearate (FA|18:0) for 2 days in WT and *SNX14-KO* cells. Values represent mean±SEM. Significance test between WT and *SNX14-KO* (n=3, ***$p<0.0001$,**$p<0.001$,*$p<0.01$, multiple t-test by Holm-Sidak method with alpha = 0.05)

C. Cell viability (%) of fibroblasts derived from 2 WT (*SNX14+/SNX14+*) subjects and 1 SCAR20 patient, showing hypersensitivity of SCAR20 cells after 2-day exposure to 0, 1000, 2000µM palmitate. Values represent mean±SEM (n=3, *$p<0.01$ relative to WT-1; ##$p<0.001$ and ###$p<0.0001$ relative to WT-2; multiple t-test by Holm-Sidak method, alpha = 0.05).

D. Cell viability (%) of WT and *SNX14-KO* cells following exposure to increasing palmitate concentration (0, 250, 500, 750, 1000 µM) and treated with 10 µM Etomoxir for 2 days. Values represent mean±SEM.

E. Cell viability (%) of WT and *SNX14-KO* cells following addition of increasing palmitate concentration (0, 250, 500, 750, 1000µM) in presence of 50µM Myriocin for 2 days. Values represent mean±SEM.

**SFA-induced lipotoxicity in *SNX14-KO* cells is associated with defects in ER morphology**

A major FA destination is their incorporation into membrane glycerophospholipids via *de novo* lipid synthesis and esterification at the ER. Excessive SFA incorporation into diacyl-glycerophospholipids can impact ER membrane fluidity and drive cellular stress (Borradaile et al. 2006a; Shen et al. 2017). To determine whether SFA exposure affected ER homeostasis in *SNX14-KO* cells, we examined ER morphology of WT and *SNX14-KO* cells exposed to palmitate via fluorescence confocal microscopy. Whereas the immunofluorescently stained ER network of WT cells was reticulated and regular following overnight exposure to 500μM palmitate, *SNX14-KO* cells displayed perturbed ER morphology. The ER of *SNX14-KO* cells appeared fragmented, and contained drastic bulges within the tubular network following palmitate treatment (**Figure 4.2A; red arrows**). A subpopulation of *SNX14-KO* cells exhibited solubilized ER lumen marker in the cytoplasm, suggesting defects in ER integrity. We quantified these ER morphological alterations into distinct classes (**Figure 4.2A,B; white arrows indicating ER morphology of each class**), revealing ~70% of *SNX14-KO* cells exhibited irregular or fragmented ER structure following palmitate exposure, compared to only ~22% of WT (**Figure 4.2B**). These perturbations became more prominent when examining ER ultrastructure with transmission electron microscopy (TEM). Here, WT and *SNX14-KO* cells were either left untreated or cultured in media containing 500μM of palmitate for 6hrs or 16hrs. Even with palmitate, WT cells exhibited normal tubular ER networks and did not manifest any significant change in the ER morphology (**Fig. 4.2C**). *SNX14-KO* cells not exposed to palmitate also exhibited normal ER morphology. However, the ER of *SNX14-KO* cells exposed to 6hrs palmitate appeared swollen and dilated, forming sheet-like extensions within the thin-section plain (**Figure 4.2C; red arrows**). This ER dilation in *SNX14-KO* cells was more pronounced following 16hrs treatment (**Figure 4.2C; red arrows**).

Since Snx14 is implicated in LD biogenesis, we also examined LD morphology in WT and *SNX14-KO* cells exposed to palmitate overnight. Whereas WT cells generated many small LDs in response to palmitate, *SNX14-KO* cells exhibited significantly fewer LDs that stained more poorly with the LD dye monodansylpentane (MDH), suggesting defective palmitate processing and LD incorporation (**Supplementary Figure 4.2A, B**). Collectively, these observations suggest that

*SNX14-KO* cells manifest altered ER architecture and LD homeostasis following prolonged exposure to palmitate.

Changes in ER lipid homeostasis can induce the unfolded protein response (UPR) as well as caspase-dependent apoptotic cell death (Listenberger et al. 2003). To understand whether such responses were associated with palmitate-induced cell death in Snx14 deficienct cells, we monitored them in *SNX14-KO* cells. First, we examined the levels of spliced Xbp1 (s-Xbp1) following palmitate exposure. As expected, palmitate induced elevated s-Xbp1 levels compared to no treatment in both WT and *SNX14-KO* cells, but there was not a significant difference between *SNX14-KO* cells compared to WT (**Supplementary Figure 4.2C**). In line with this, addition of the IRE1 inhibitor 4µ8c or PERK inhibitor GSK2606414, both of which suppress branches of UPR signaling, did not rescue palmitate-induced cell death in *SNX14-KO* cells, suggesting altered or hyper-active UPR signaling was not causative of *SNX14-KO* cell death following palmitate exposure (**Supplementary Figure 4.2D**). To dissect whether SFAs induced an apoptotic response in *SNX14-KO* cells, we also treated cells with the caspase-6/8 inhibitor SCP0094. This did not rescue palmitate-induced cell death, indicating *SNX14-KO* cells were not manifesting hyper-active caspase-6/8-dependent apoptosis (**Supplementary Figure 4.2D**).
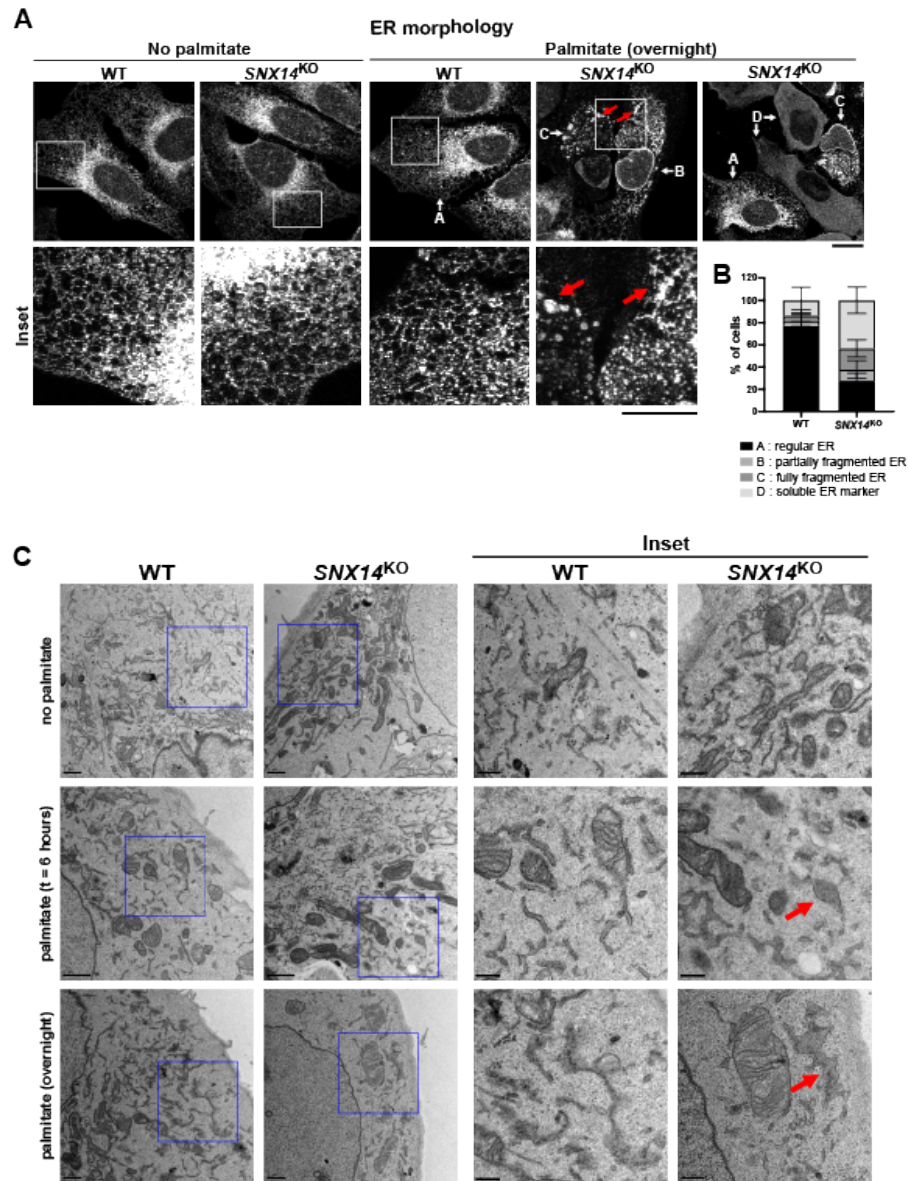
**Figure 4.2: Palmitate-induced hypersensitivity in *SNX14-KO* is associated with defective ER morphology**

**A.** Immunofluorescent (IF) labeling of the ER with α-HSP90B1 (ER marker) antibody before and after overnight palmitate treatment in WT and *SNX14-KO* cells. Scale bar = 10μm. Red arrows indicating the extensive bulges in the ER. White arrows indicating each class of ER morphology where A is regular ER, B is partially fragmented ER, C is fully fragmented ER and D shows soluble ER marker.

**B.** Percentage of palmitate treated WT and *SNX14-KO* cells quantified and grouped based on whether the ER morphology is regular (A), partially fragmented (B), fully fragmented (C) or completely soluble (D). Total ~100 cells quantified from 3 experiments. Values represent mean±SEM.

**C.** TEM micrographs of WT and *SNX14-KO* cells with no palmitate treatment and with palmitate treatment for 6hr and overnight to visualize ER ultra-structure. Scale bar = 1μm. Scale bar of inset = 0.5 μm. Red arrows indicate ER dilation in palmitate treated *SNX14-KO* cells.
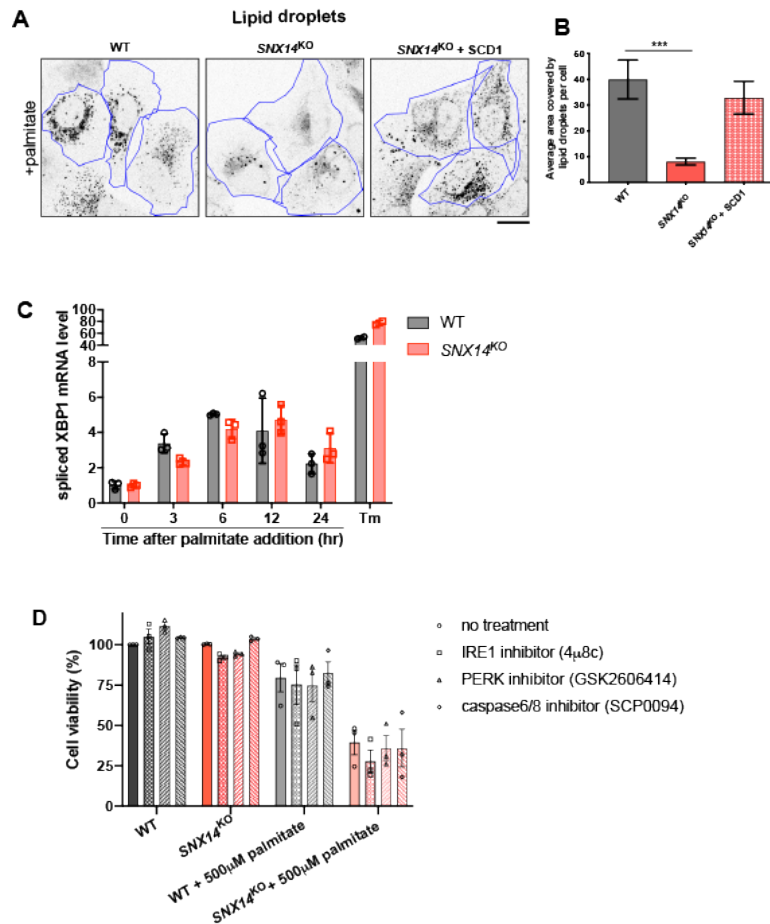
**Supplementary Figure 4.2**

**A.** Confocal micrographs of WT and *SNX14-KO* cells treated with palmitate overnight and stained with monodansylpentane (MDH) to visualize LDs (black). The cell boundary is marked by blue outline. Images are processed so that the LDs are grayscaled and then inverted in Image-J. Scale bar = 10μm.

**B.** Average area covered by LDs per cell of representative images from Supplementary Figure 2A is quantified. Total LD area was derived from six fields of view, each consisting of approximately eight cells from two different sets of experiments (total no. of cells ~90; ***$p < 0.0001$ unpaired t test with $\alpha = 0.05$).

**C.** RT-PCR data of spliced Xbp1 mRNA levels which is an indicator of UPR activity in WT and *SNX14-KO* cells treated with palmitate for indicated time. Tunicamycin (Tm) treatment for 6hr (5 μg/ml) used as control which induces UPR activity.

**D.** Cell viability (%) of WT and *SNX14-KO* cells following 2 days exposure to 500μM palmitate and either untreated or treated with one of the following –a) 64μM of IRE1 inhibitor 4μ8c (b) 30 nM of PERK inhibitor GSK2606414 (c) 40μM of caspase 6/8 inhibitor SCP0094. The assay was repeated thrice in triplicates. Values represent mean±SEM.

**APEX-based proteomics reveals Snx14 is in proximity to proteins involved in SFA metabolism**

Given that Snx14 was required for maintaining ER morphology and LD biogenesis following palmitate exposure, we next investigated what proteins Snx14 interacted with that may promote lipid homeostasis. Previously we utilized an ascorbate peroxidase APEX2-based proximity technology to examine the localization of APEX2-tagged Snx14 at ER-LD contact sites using TEM (Datta et al. 2019). APEX2-tagging also enables the local interactome of a protein-of-interest to be interrogated. The addition of biotin-phenol and hydrogen peroxide to APEX2-expressing cells induces the local biotinylation of proteins within ~20nm of the APEX2 tag. These biotinylated proteins can be subsequently affinity purified via streptavidin beads and identified via mass-spectrometry (MS) (Hung et al. 2016) (**Figure 4.3A**). As ER-LD contacts are lipogenic ER sub-domains with known roles in FA processing, we hypothesized that Snx14's enrichment at ER-LD junctions represented an opportunity to use APEX2 technology to reveal proteins that contribute to ER lipid metabolism in conjunction with Snx14.

We generated *U2OS* cells stably expressing Snx14-EGFP-APEX2 and *HEK293* cells transiently expressing Snx14-EGFP-APEX2 and exposed them to oleate to induce Snx14 recruitment to ER-LD contacts. We then treated cells with biotin-phenol for 30 minutes and hydrogen peroxide for 1 minute. As expected, co-immunofluorescence staining of *U2OS* cells for Streptavidin-Alexa647 and EGFP revealed their colocalization, suggesting proteins in close proximity to Snx14-EGFP-APEX2 were biotinylated (**Figure 4.3B**). Biotinylated proteins from both *U2OS* and *HEK293* cells were then affinity purified with streptavidin beads. Gel electrophoresis followed by Coomassie staining and anti-streptavidin/HRP Western blotting revealed many biotinylated proteins in Snx14-EGFP-APEX2-expressing cell lysates, but not in controls lacking APEX2 (**Figure 4.3C**). The bead enriched biotinylated proteins from both Snx14-EGFP-APEX2 and the control lacking APEX2 were then identified by tandem MS/MS proteomic analysis.

Previous proteomics studies have isolated LDs and characterized LD-associated proteins (Krahmer et al. 2013; Beller et al. 2006; Ding et al. 2012; Beller et al. 2008; Bersuker et al. 2018), and several

of these were also detected in our APEX2-based approach (**Figure 4.3D**). However, to confirm that these peptide hits were specific to the Snx14-EGFP-APEX2 interactome, we also conducted proteomics on biotinylated proteins from cells expressing a soluble EGFP-APEX2 (cyto-APEX) as well as cells expressing APEX2-tagged Sec61β, a general ER marker (ER-APEX). High abundance peptides in the Snx14-EGFP-APEX2 proteomics that were correspondingly low in the cyto-APEX and ER-APEX were thus considered high confidence hits (**Figure 4.3D, Supplementary Table 1**). Notably, this list included well-characterized LD surface proteins Perilipin 3 (PLIN3), Perilipin 2, and PNPLA2. In fact, PLIN3 was one of the most enriched proteins from both cell line samples (>65-fold) (**Supplementary Figure 4.3A**), consistent with it being a highly abundant LD protein that coats newly synthesized LDs. Proteins recently highlighted as localizing to ER-LD contact sites were also identified including VPS13C and VPS13A (Kumar et al. 2018). We also detected several Rab proteins such as Rab7a, Rab10, and Rab11b, which had previously been detected on LDs using a LD-targeted APEX approach (Bersuker et al. 2018). Additionally, we detected enzymes involved in ER-associated lipid synthesis, including lyso-phospholipid acyltransferases LPCAT1, LPCAT3, and LPGAT, as well as enzymes driving sterol metabolism like the sterol O-acyltransferase SOAT1, the squalene synthase FDFT1, and the squalene epoxidase SQLE. Lastly, we noted several enzymes involved in FA metabolism and desaturation including ACSL4, ELOVL1, ELOVL5, FASN, SCD1, FADS1, and FADS2.

To identify Snx14 functional interactors that may play a role in FA metabolism that was defective in *SNX14-KO* cells, we implemented a multi-stage analysis approach (**Figure 4.3E**). First, we selected proteins that were greater than 2.0-fold enriched in Snx14-EGFP-APEX2 samples over negative controls lacking APEX2 (**Supplementary Figure 4.3A, Circle 1 of Figure 4.3E**). Next, we focused on proteins annotated to localize to the ER network but also specific to the Snx14 interactome, since the ER was the primary organelle that manifested morphological alterations in *SNX14-KO* cells following palmitate exposure. We did this by eliminating proteins detected at similar levels in both the ER-APEX and Snx14-EGFP-APEX2 proteomics (**Supplementary Figure 4.3A, B; Circle 2 of Figure 4.3E**). We then applied gene ontology enrichment analysis on

the annotated ER-associated proteins specific to Snx14 (**Circle 3 of Figure 4.3E, Supplementary Figure 4.3C**), revealing that ~250 of these proteins are associated with cellular metabolism, and ~100 with lipid metabolism (**Supplementary Figure 4.3D**).

With this smaller candidate list, we compared them to a recently published genome-wide CRISPR/Cas9 screen identifying proteins whose loss sensitized cells to palmitate-induced lipotoxicity (Zhu et al. 2019). Remarkably, this unbiased screening identified Snx14 in the top 6% of proteins that were protective against palmitate (KO gene score: -2.28). This study also identified 310 proteins detected in our Snx14 interactome that exhibited a negative score greater than -1.8 for palmitate sensitivity (Zhu et al. 2019) (**Supplementary Table 1; orange dots of Supplementary Figure 4.3A; Circle 4 of Supplementary Figure 4.3E**). These palmitate-sensitive proteins included FADS1, FADS2, SCD1, CEPT1 and HSD17B12 (**Supplementary Figure 4.3F**). As a final stage of analysis, we compared our list to our recently published interactome of Snx14 *Drosophila melanogaster* ortholog Snz, which also functions in lipid homeostasis in fruit fly adipocytes (Ugrankar et al. 2019). Snz proteomics identified the enzyme DESAT1, the major fly Δ-9 FA desaturase, as a key Snz interactor that was required for Snz-driven TAG synthesis in *Drosophila* (Ugrankar et al. 2019). DESAT1 is the ortholog of human Δ-9 FA desaturase SCD1, which catalyzes the conversion of SFAs to MUFAs prior to their incorporation into glycerophospholipids or neutral lipids (Paton and Ntambi 2009). Indeed, several lines of evidence converged on SCD1 and its desaturation activity as being functionally linked to Snx14: 1) both proteins are ER-associated integral membrane proteins, and SCD1 was highly enriched in Snx14-EGFP-APEX2 proteomics in both *U2OS* and HEK293 cell lines (**Figure 4.3D, Supplementary Figure 4.3A**); 2) SCD1 genetic or pharmacological perturbation hyper-sensitizes cells to palmitate-induced cell death, similar to Snx14 loss (Listenberger et al. 2003; Miyazaki et al. 2000; Miyazaki, Kim, and Ntambi 2001) (**Figure 4.3F**); 3) in genome-wide screening both Snx14 and SCD1 scored similarly in impact to palmitate sensitivity (SCD1: -2.42, Snx14: -2.28) (Zhu et al. 2019). Based on this analysis, we chose to investigate the functional interplay between Snx14 and SCD1-associated FA desaturation in ER lipid homeostasis.
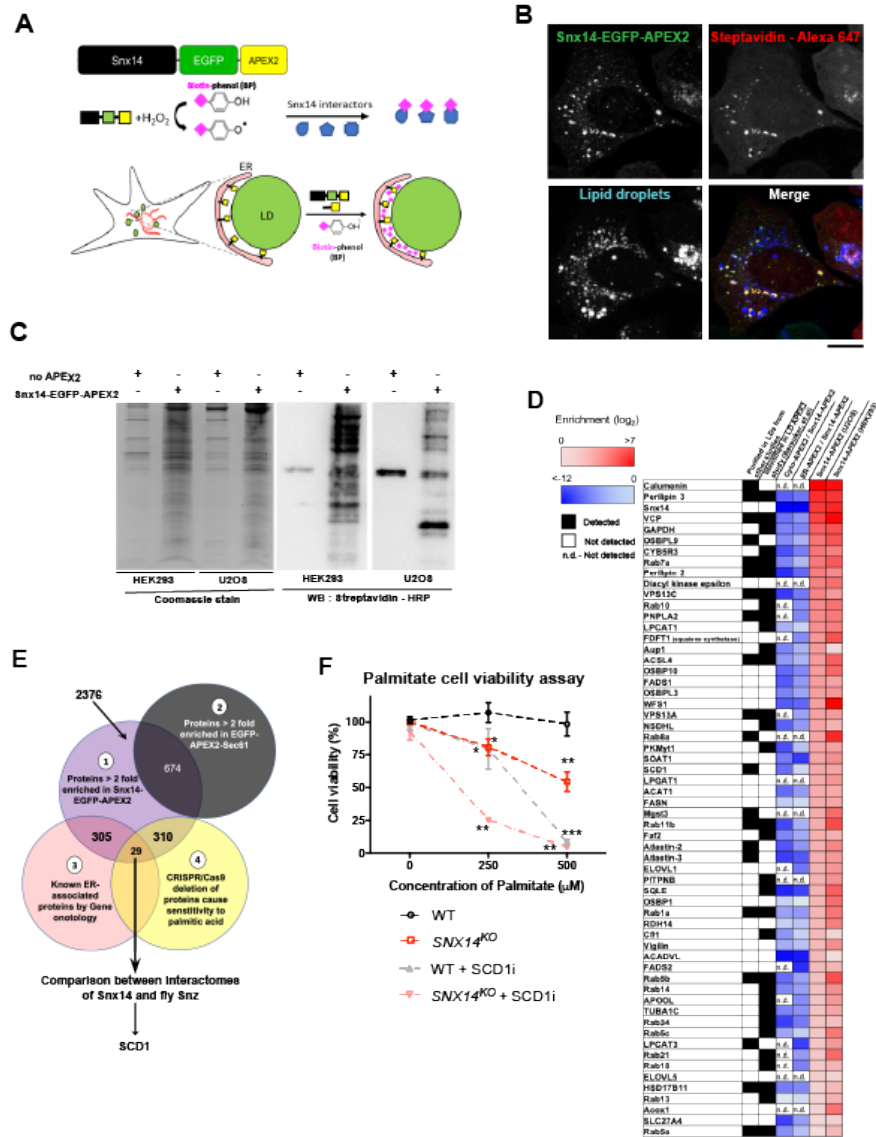
**Figure 4.3: APEX2-based proteomics reveals the Snx14-associated ER-LD proteome**

**A.** Schematic diagram showing Snx14 tagged with EGFP-APEX2. The reaction of biotin phenol and $H_2O_2$ catalysed by APEX2 generates biotin-phenoxyl radicals which covalently attaches with proteins proximal to Snx14. Following oleate treatment, APEX2 tagged Snx14 enriches at ER-LD contacts to biotinylate the interactors of Snx14 at those contacts.

**B.** Co-IF staining of cells stably expressing Snx14-EGFP-APEX2 with anti-EGFP (green) antibody, streptavidin-conjugated Alexa647 fluorophore (biotinylated proteins, red) antibody and LDs stained with monodansylpentane (MDH, blue). Scale bar = 10μm.

**C.** Biotinylated proteins pulled down by streptavidin conjugated beads from HEK293 and U2OS cells expressing Snx14-EGFP-APEX2 and no-APEX2 (negative control) were Coomassie stained and Western blotted.

**D.** Heat map of ~60 proteins highly enriched in Snx14-APEX2 proteomics (red columns), de-enriched in the cyto-APEX2 and ER-APEX2 proteomics (blue columns) and cross referenced with other LD proteomics (referenced in text).

**E.** Venn diagram representing the multi-stage analysis of the MS data from Snx14-EGFP-APEX2, no-APEX2 and EGFP-APEX2-Sec61. 2376 proteins are enriched >2 fold in Snx14-EGFP-APEX2 (1: purple circle). Among them 674 which are also enriched in APEX2-Sec61 are excluded (2 : black circle). 305 of (1) are ER-associated according to Gene ontology analysis (3: red circle). Again 310 of (1) comprise of genes whose CRISPR/Cas9 deletion cause palmitate sensitivity (Zhu et al. 2019) (4 : yellow circle). Overlap of sets (1),(3) and (4), revealed 29 Snx14 interactome. Its comparison with fly homolog Snz interactome included SCD1.

**F.** Cell viability of WT and *SNX14-KO* cells treated with 4μM SCDi along with increasing palmitate concentration (0, 250, 500μM) for 2 days. Values represent mean±SEM. (n=3, *p<0.1, **p<0.001, ***p<0.0001, multiple t-test by Holm-Sidak method, alpha = 0.05).
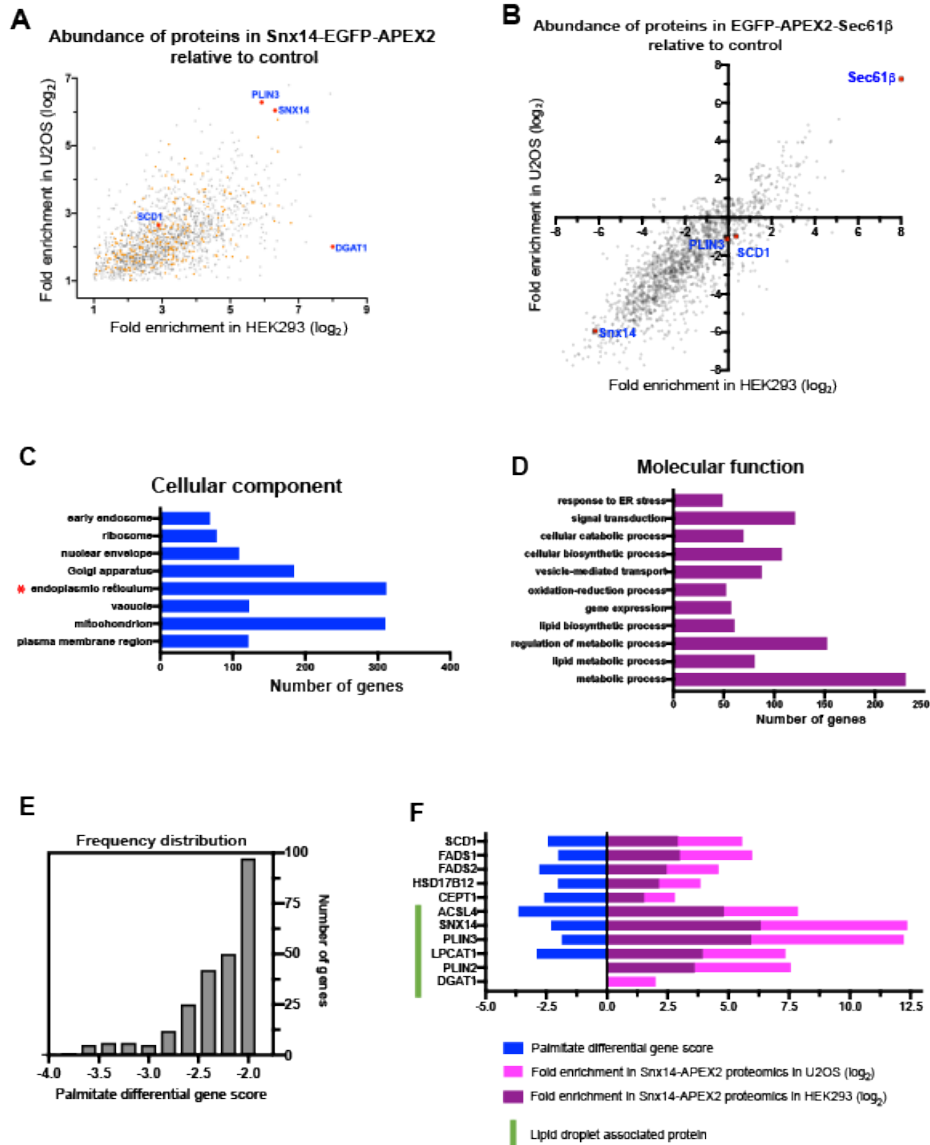
**Supplementary Figure 4.3**

**A.** Proteins enriched for Snx14 from set (1) of Figure 3E after excluding proteins also enriched for Sec61 are plotted as log₂ fold enrichment relative to negative control from HEK293 (x-axis) and U2OS cells (y-axis) and are denoted by grey dots. Orange dots represent those proteins whose CRISPR/Cas9 deletion results in palmitate mediated sensitivity.

**B.** Log₂ fold enrichment of proteins in APEX2-Sec61 relative to negative control from HEK293 (x-axis) and U2OS cells (y-axis) are plotted and denoted by grey dots.

**C.** Gene ontology enrichment analysis by ClueGO using Cytoscape software grouped genes from set (1) of Figure 3E according to their association with a cellular organelle.

**D.** Gene ontology enrichment analysis by ClueGO using Cytoscape software clustered ER-localized genes from Supplementary Figure 3C according to their molecular function.

**E.** Frequency distribution of the CRISPR/Cas9 screened genes tested negative (<-1.8) for palmitate treatment from (Zhu et al. 2019) enriched specifically for Snx14 (denoted as orange dots) in Supplementary Figure 3A.

**F.** Examples of some proteins including LD-associated proteins which are specifically and highly enriched in Snx14 after analysis in Figure 3E and also has a high negative screen score showing palmitate sensitivity similar to Snx14 from (Zhu et al. 2019).

***SNX14-KO* cell FA elevations are similar to cells with reduced SCD1 activity**

To begin dissecting the functional interplay between Snx14 and FA metabolism, we conducted whole-cell lipidomic FA profiling. We pulsed WT and *SNX14-KO* cells for 2 hrs with 500μM palmitate, extracted polar lipids, and conducted gas chromatography (GC)-MS analysis to profile polar lipid fatty acyl chain length and saturation. Indeed, *SNX14-KO* cells exhibited a significant increase in total polar lipid-derived FAs (**Supplementary Figure 4.4A**), as well as a significant increase in the abundance of 16-carbon length saturated fatty acyl chains (FA|16:0) in polar lipids relative to WT cells (**Figure 4.4A**). To determine whether this increase mimics alterations in polar lipids when SCD1 function is perturbed, we also treated WT cells with SCD1 inhibitor (SCD1i). Indeed, WT cells exposed to SCD1i exhibited similar increases in 16:0 saturated fatty acyl chains in their polar lipid fraction, mirroring elevations observed in *SNX14-KO* cells (**Figure 4.4A**). Furthermore, SCD1i-treated *SNX14-KO* cells exhibited no additional 16:0 acyl chain increases in the polar lipid profile, implying SCD1i treatment and Snx14 loss may perturb the same pathway.

**TG, PC, and lysolipids exhibit significant elevations in saturated acyl chains in *SNX14-KO* cells**

To further dissect how specific lipid classes are altered by Snx14 loss, we conducted global lipidomics via quantitative liquid-chromatography (LC)-MS analysis. WT and *SNX14-KO* cells were either left untreated or exposed to 2 hrs of palmitate, harvested, and analyzed. For comparative analysis, we again treated cells with SCD1i. Importantly, this LC-MS analysis revealed fatty acyl properties such as chain length and saturation types of major lipid classes, including triacylglycerol (TG), diacylglycerol (DAG), phosphatidylethanolamine (PE), phosphophatidylcholine (PC), phosphatidic acid (PA), phosphatidylserine (PS), and lysophospholipids. Analysis revealed a significant (~40%) increase in the levels of DAG, LPE and PC in *SNX14-KO* cells relative to WT cells following palmitate treatment as calculated from the fold change percentage of the color-coded heat map (**Figure 4.4B**). However, relative abundances of most lipid classes between these two samples with or without palmitate treatment were not significantly altered.

Next, we examined the change in acyl chain saturation within each lipid class in *SNX14-KO* cells. In general, there was a greater proportion of saturated fatty acyl chains within several lipid classes. The most significant change in saturated fatty acyl chains in palmitate-treated *SNX14-KO* cells relative to WT was in TAG and lyso-PC (LPC). Examining ~60 different TAG species revealed the most significant increase in TAG species containing two or more saturated acyl chains. These TAG species contained either 0 or 1 unsaturation among all three acyl chains (denoted as an N score of 0 or 1) (**Figure 4.4C**). For example, TG|48:1(NL-16:1), which contains one mono-unsaturated (16:1) acyl chain and two fully saturated acyl chains, was significantly elevated in *SNX14-KO* cells following palmitate treatment (**Figure 4.4C, species 11**). Notably, TAG 50:0 (NL-16:0) and 50:0 (NL-18:0), both of which contained three saturated acyl chains, were also elevated in *SNX14-KO* cells compared to WT following palmitate addition and SCD1 inhibition, suggesting *SNX14-KO* cells incorporated SFAs into TAG more than WT cells (**Figure 4.4C, species 1 and 2**). For more general analysis, we pooled the abundances of all TAG species comprising only 0 or 1 total fatty acyl unsaturation. Indeed, TAG pooling revealed that TAG species containing 0 or 1 unsaturation was significantly increased in palmitate treated *SNX14-KO* cells, and closely mirrored levels of WT cells treated with SCD1i (**Figure 4.4D**). Collectively, this suggests that the TAG lipid profile of palmitate-treated *SNX14-KO* cells appears similar to cells with perturbed SCD1 function.

Among polar lipid species, the abundance of LPC species containing the saturated fatty acyl chain 18:0 was significantly increased in palmitate-treated *SNX14-KO* cells relative to WT (**Figure 4.4E**). In fact, levels of 18:0-containing LPC in *SNX14-KO* cells treated with palmitate closely mirrored WT cells treated with palmitate and SCD1i, again indicating that *SNX14-KO* cells closely resembled cells with inhibited SCD1 function by lipid profiling (**Figure 4.4E**). In line with this, there was a decrease in LPC species containing 18:1 or 18:2 acyl chains following palmitate treatment. LPE species containing 18:0 fatty acyl chains were also significantly increased in *SNX14-KO* cells even without palmitate treatment (**Supplementary Figure 4.4B**). Profiling of PC, one of the most abundant glycerophospholipids, also revealed an increase in PC species with 18:0 fatty acyl chain in *SNX14-KO* cells, and that was more pronounced with palmitate treatment
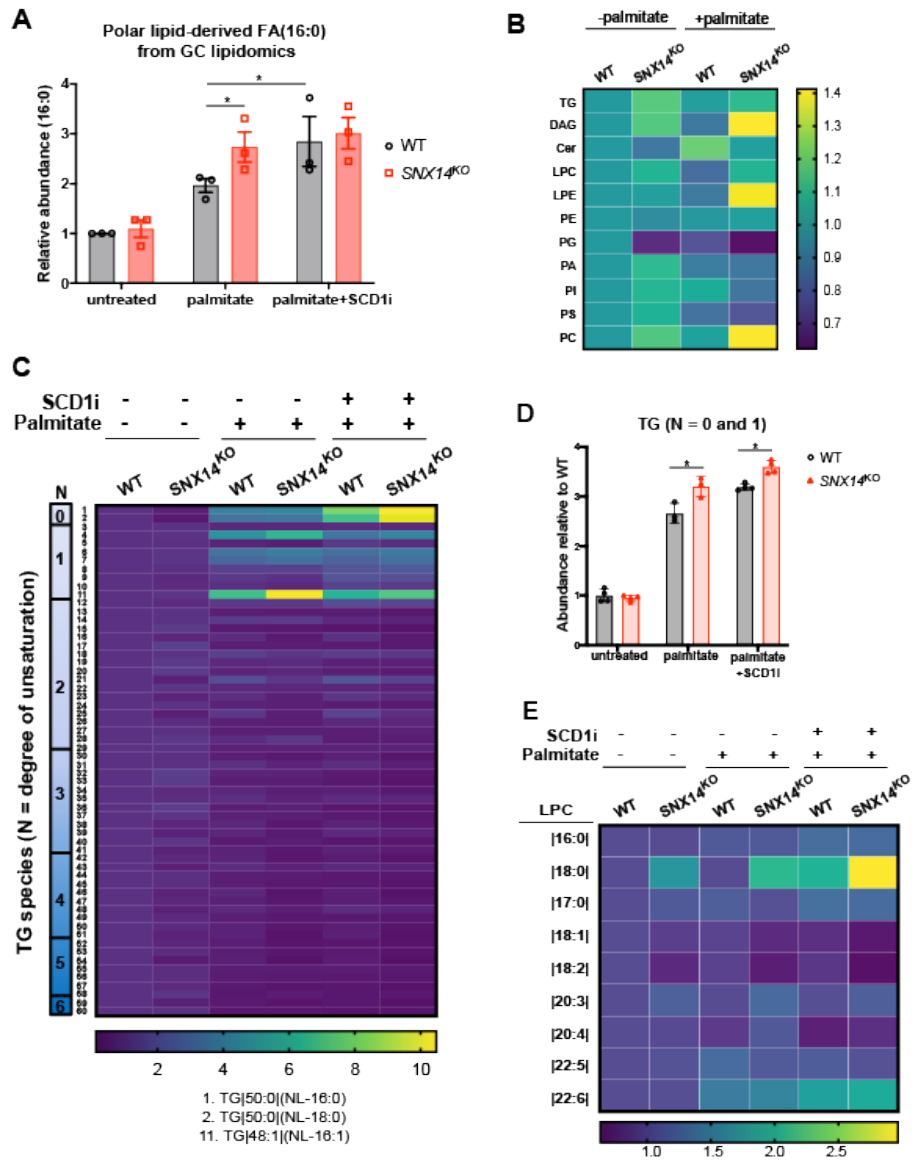
**Figure 4.4: *SNX14-KO* cell lipidomic profiling is similar to cells with reduced SCD1 activity**

**A.** Abundance of FAs (16:0) derived from polar lipids of WT and *SNX14-KO* cells relative to untreated WT under the following conditions – no treatment, palmitate treatment and treatment with palmitate and SCD1 inhibitor (SCD1i). Values represent mean ± SEM (n=3, *p<0.01, multiple t-test by Holm-Sidak method with alpha = 0.05).

**B.** Heatmap indicating the relative change in abundance of individual lipid species of *U2OS* WT and *SNX14-KO* cells before and after palmitate treatment relative to untreated WT cells.

**C.** Heatmap indicating the relative change in abundance of 60 different TG species of WT and *SNX14-KO* cells relative to untreated WT. These cells were either untreated or treated with palmitate or palmitate in presence of SCD1i. N indicates the number of double bonds in those group of TG species. The vertical serial number represents a different TG species where 1 is TG|50:0|(NL-16:0) and 11 is TG|48:1|(NL-16:1) and they exhibit the most changes in TG in the treated *SNX14-KO* cells.

**D.** Abundance of TG (with 0 or 1 unsaturation) relative to untreated WT as analyzed in WT and *SNX14-KO* cells quantified from Figure 4C. These cells were either untreated or treated with palmitate or palmitate in presence of SCD1i. Values represent mean±SEM (n=3, *p<0.01, multiple t-test by Holm-Sidak method with alpha = 0.05).

**E.** Heatmap indicating the relative change in abundance of 9 different LPC species of WT and *SNX14-KO* cells relative to untreated WT. These cells were either untreated or treated with palmitate and palmitate in presence of SCD1i.
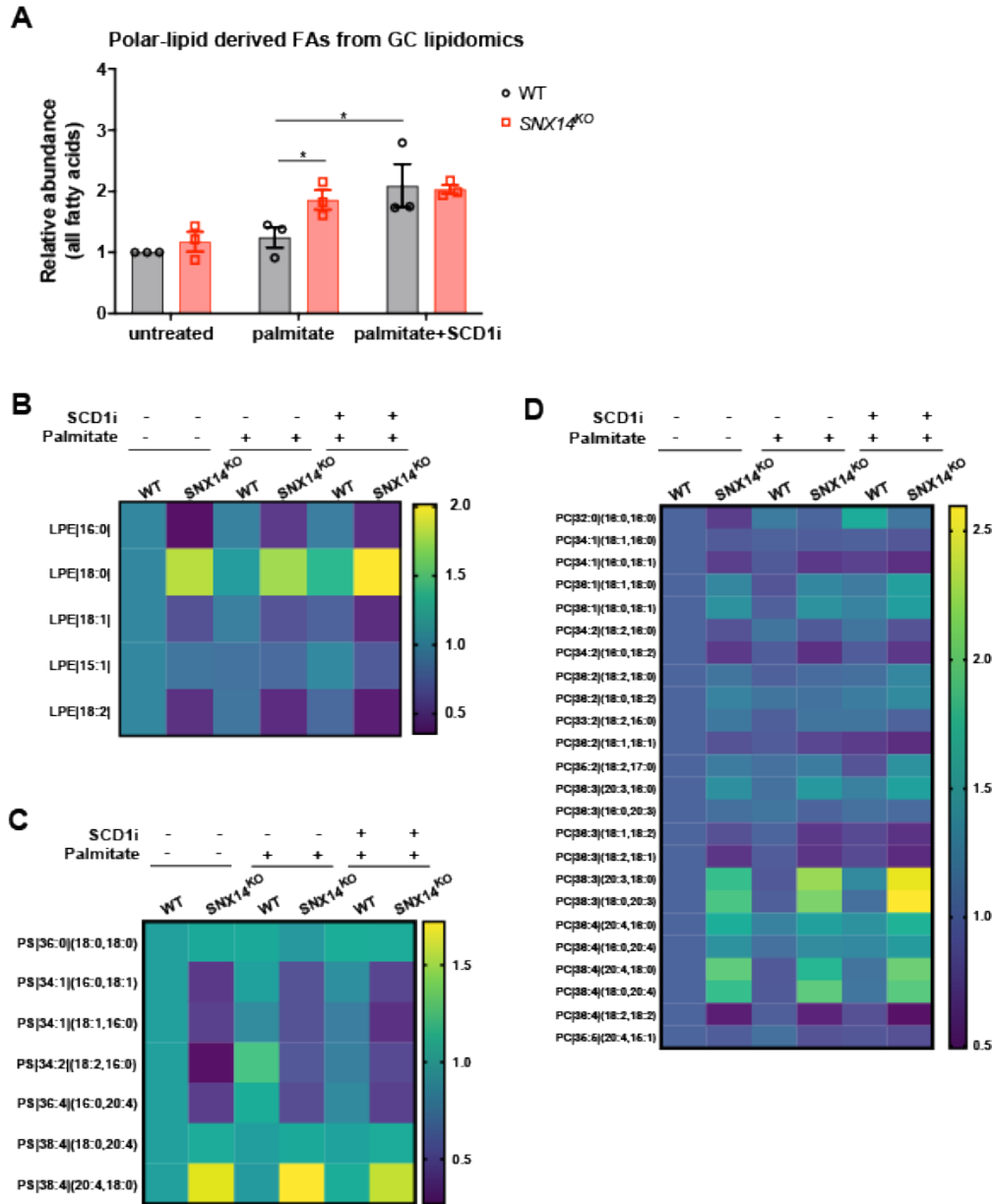
**Supplementary Figure 4.4**

A. Abundance of all fatty acids derived from polar lipids of WT and *SNX14-KO* cells relative to untreated WT under the following conditions – no treatment, palmitate treatment or treatment with palmitate and SCD1i. Values represent mean±SEM (n=3, *p<0.01, multiple t-test by Holm-Sidak method with alpha = 0.05).

B. Heatmap indicating the relative change in abundance of 5 different LPE species of WT and *SNX14-KO* cells relative to untreated WT. These cells were either untreated or treated with palmitate or palmitate in presence of SCD1i.

C. Heatmap indicating the relative change in abundance of 7 different PS species of WT and *SNX14-KO* cells relative to untreated WT. These cells were either untreated or treated with palmitate or palmitate in presence of SCD1i.

D. Heatmap indicating the relative change in abundance of 24 different PC species of WT and *SNX14-KO* cells relative to untreated WT. These cells were either untreated or treated with palmitate or palmitate in presence of SCD1i.

followed by SCD1 inhibition (**Supplementary Figure 4.4D**). PS lipid profiles were similarly altered in *SNX14-KO*, with increases in PS species containing 18:0 saturated fatty acyl groups, and a corresponding decrease in PS with 18:1 or 18:2 acyl chains (**Supplementary Figure 4.4C**).

Collectively, LC-MS lipidomics suggests: 1) *SNX14-KO* cells exhibit elevated TAG species containing two or more saturated acyl chains, 2) *SNX14-KO* cells have increased levels of LPC and LPE lysolipids containing saturated fatty acyl chains, 3) *SNX14-KO* cells exhibit more PC and PS with an 18:0 saturated acyl chain and less with 18:1 or 18:2, and 4) for TAG and LPC, the lipid profiles of *SNX14-KO* cells exposed to palmitate closely mirror cells with inhibited SCD1 function.

**SCD1 activity can rescue *SNX14-KO* palmitate-induced lipotoxicity**

Given the increased lipid saturation profiles of *SNX14-KO* cells, we next examined SCD1 protein levels in the context of Snx14 loss. SCD1 protein abundance was similar in WT and *SNX14-KO* cells under ambient conditions, but became elevated in both cell lines when exposed to 500μM palmitate. Notably, SCD1 protein levels were significantly more elevated in *SNX14-KO* cells exposed to palmitate. Snx14-Flag over-expressing cells returned SCD1 protein levels to WT levels, implying that *SNX14-KO* cells may further elevate SCD1 protein expression to compensate for Snx14 loss (**Figure 4.5A,B**).

Since *SNX14-KO* cells exhibited slightly elevated SCD1 levels, we queried whether ectopic SCD1 over-expression could reduce *SNX14-KO* cell palmitate hyper-sensitivity. Strikingly, SCD1 over-expression rescued *SNX14-KO* cell viability, and *SNX14-KO* cells now responded similarly to WT cells exposed to dose-dependent palmitate treatment (**Figure 4.5C**). *SNX14-KO* cells were also rescued by exposure to mixtures of palmitate and oleate, the MUFA and product of SCD1 enzymatic activity (**Supplementary Figure 4.5A**). Since *SNX14-KO* cells also displayed defective LD morphology with palmitate, we tested whether SCD1 over-expression could restore LD levels. Indeed *SNX14-KO* cells over-expressing SCD1 manifested more LDs following palmitate exposure (**Supplementary Figure 4.2A,B**). Since LDs are lipid reservoirs, we determined whether

this SCD1-mediated rescue required the incorporation of FAs into TAG for LD storage. We exposed *SNX14-KO* cells to DGAT1/2 inhibitors (DGATi) in the presence of palmitate, and monitored cell viability. Surprisingly, SCD1 over-expression rescued *SNX14-KO* cells even with DGATi, suggesting this SCD1-mediated rescue functions upstream of TAG synthesis (**Supplementary Figure 4.5B**).

Since the *SNX14*[KO] lipidomics profile phenocopied inhibited SCD1 activity, and SCD1 over-expression mitigated palmitate-induced *SNX14*[KO] cell death, we hypothesized that *SNX14*[KO] cells had defects processing SFAs. To test this, we exposed WT and *SNX14*[KO] cells to 500μM palmitate for 0, 2, 4, 8, and 16 hr, extracted whole cell lipids and conducted thin layer chromatography (TLC) to monitor changes in free FAs (FFAs) and neutral lipids. As expected, both WT and *SNX14*[KO] cells exhibited elevated FFA levels following 2 and 4 hrs palmitate exposure, but *SNX14*[KO] exhibited significantly elevated FFAs compared to WT (**Fig 5D, S5C**). SCD1 over-expression reversed this FFA elevation at 4 hrs in *SNX14*[KO] cells, implying the elevated FFA pool was composed of SFAs that could be processed by SCD1 (**Figure 4.5E, Supplementary Figure 4.5D**). As a key control, we monitored uptake of radio-labeled ^{14}C-palmitate in WT and *SNX14*[KO] cells, to test whether elevated FFA accumulation in *SNX14*[KO] cells was due to increased FA uptake. We confirmed that FA uptake was not altered by Snx14 loss (**Supplementary Figure 4.5E**), indicating that *SNX14*[KO] cells accumulate FFAs following palmitate uptake, consistent with a defect in palmitate processing, and these effects can be reversed by SCD1 over-expression.

To understand whether the ER fragmentation observed in *SNX14*[KO] cells is associated with defects in palmitate processing, we examined ER morphology in SCD1 over-expressed *SNX14*[KO] cells following palmitate exposure. Remarkably, palmitate treated *SNX14*[KO] cells ectopically expressing SCD1 displayed ER morphologies similar to palmitate treated WT cells (**Figure 4.5F, G**). Collectively, this suggests that SCD1 over-expression can rescue *SNX14*[KO] elevated lipid saturation, LD morphology, and ER fragmentation which may together contribute to lipotoxicity and cell viability.
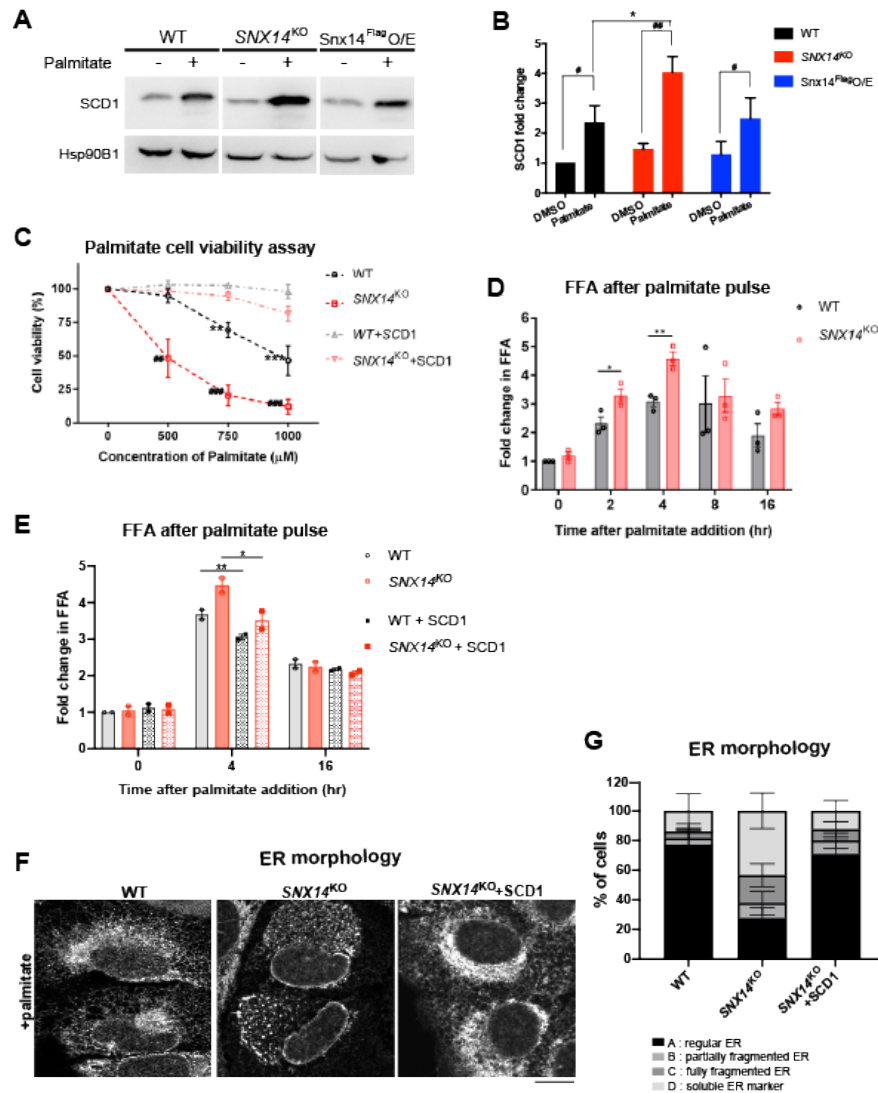
**Figure 4.5: SCD1 activity can rescue *SNX14-KO* palmitate-induced lipotoxicity**

**A.** WB of SCD1 and Hsp90B1 (ER marker) before and after overnight palmitate treatment in WT, *SNX14-KO* and Snx14FlagO/E.

**B.** Ratio of the intensity of the protein bands of SCD1 over Hsp90B1 from A, and plotted as fold change relative to untreated WT set as 1. Values represent mean ± SEM. Significance test between palmitate treatments denoted as # and between WT, *SNX14-KO* and Snx14FlagO/E is denoted as * (n=3, #p<0.1, ##p<0.001; *p<0.01); multiple t-test by Holm-Sidak method with alpha = 0.05)

**C.** Cell viability (%) of WT and *SNX14-KO* cells after SCD1 O/E following 2 day palmitate addition (0, 500, 750, 1000μM). Values represent mean±SEM. Significance test between WT and WT+SCD1 denoted as * and between *SNX14-KO* and *SNX14-KO*+SCD1 denoted as # (n=3, **p<0.001, ***p<0.0001; ##p<0.001, ## p<0.0001,multiple t-test by Holm-Sidak method with alpha = 0.05).

**D.** Fold change in FFAs relative to untreated WT (normalized to cell pellet weight) in WT and *SNX14-KO* cells treated with 500μM palmitate for 0, 2, 4, 8, 16 hours. Values represent mean±SEM (n=3, *p<0.01, multiple t-test by Holm-Sidak method, alpha = 0.05).

**E.** Fold change in FFAs relative to untreated WT (normalized to cell pellet weight) in WT and *SNX14-KO* cells before and after SCD1 O/E, treated with 500μM palmitate for 0,4,16 hrs. n=3, *p<0.01, **p<0.001, multiple t-test by Holm-Sidak method with alpha = 0.05.

**F.** Immunofluorescent (IF) labeling of the ER with α-HSP90B1 (ER marker) antibody in WT and *SNX14-KO* cells before and after overexpression of SCD1 following overnight palmitate treatment. Scale bar = 10μm.

**G.** Palmitate treated WT and *SNX14-KO* cells (%) quantified and grouped based on whether the ER morphology is regular (A), partially fragmented (B), fully fragmented (C) or completely soluble (D). n=~100 cells from 3 experiments. Values represent mean±SEM.
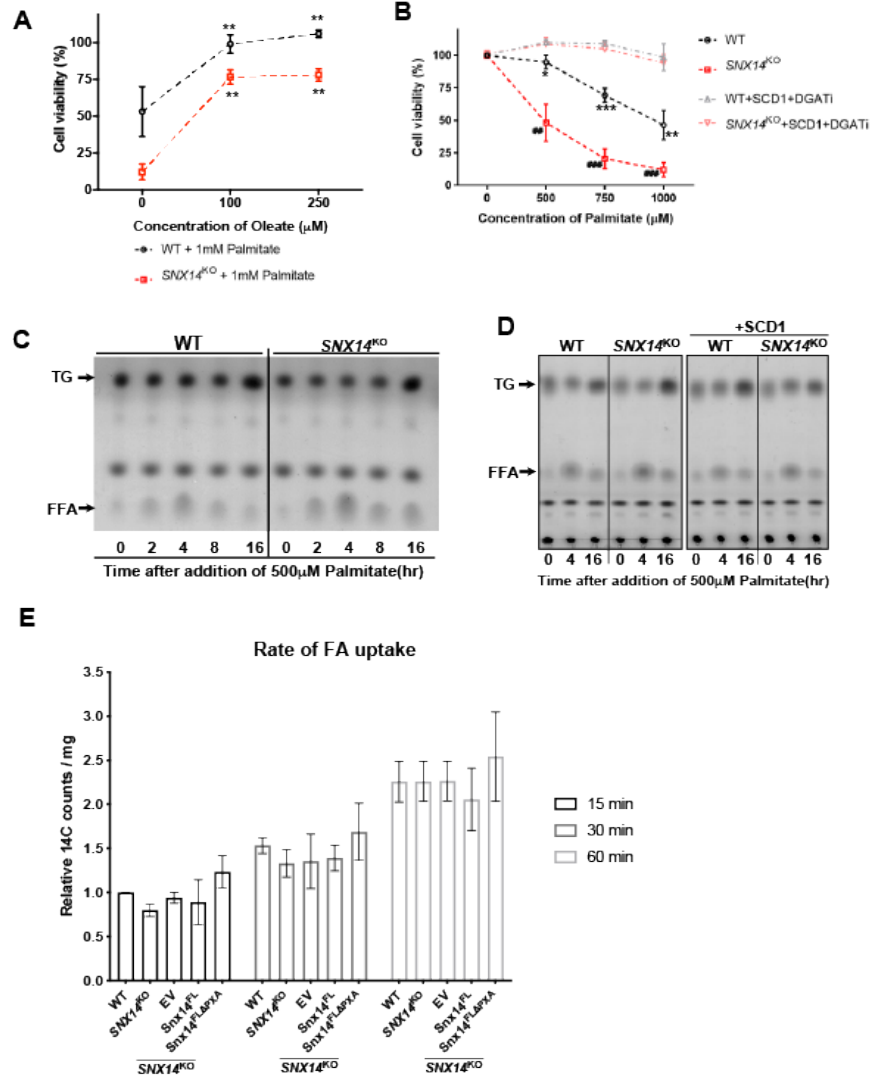
**Supplementary Figure 4.5**

A. Cell viability (%) shows increase in surviving WT and *SNX14-KO* cells when treatment with 1mM palmitate is supplemented with 100 and 200μM of oleate. The assay was repeated thrice in triplicates. Values represent mean±SEM (**$p<0.001$, multiple t-test by Holm-Sidak method with alpha = 0.05, significance test between oleate treatment with non-oleate treatment).

B. Cell viability (%) of WT and *SNX14-KO* cells after SCD1 O/E in presence of DGAT1/2 inhibitors (DGATi) following addition of palmitate (0, 500, 750, 1000μM) for 2 days. Values represent mean±SEM. Significance test between WT and WT+SCD1+DGATi denoted as * ; between *SNX14-KO* and *SNX14-KO*+SCD1+DGATi denoted as # (n=3, *$p<0.01$, **$p<0.001$, ***$p<0.0001$, ##$p<0.001$, ## $p<0.0001$, multiple t-test by Holm-Sidak method with alpha = 0.05).

C. TLC of neutral lipids and FFAs in WT and *SNX14-KO* cells treated with 500μM palmitate for 0, 2, 4, 8, 16 hours.

D. TLC of neutral lipids and FFAs performed in WT and *SNX14-KO* cells before and after overexpression of SCD1 following exposure to 500μM palmitate for 0, 4, 16 hours.

E. Fatty acid uptake in WT, *SNX14-KO* cells and *SNX14-KO* cells expressing either EV, Snx14[FL], or Snx14[FL PXA] following exposure to ^{14}C palmitate for 15, 30, 60 mins quantified relative to WT treated with 15 min ^{14}C palmitate.

**Snx14 functionally interacts with SCD1 in the ER network**

The functional similarities in SFA processing observed between *SNX14-KO* and SCD1 inhibited cells indicated their possible interaction within the ER network, which we examined by co-immunoprecipitation (co-IP). We generated *U2OS* cell lines stably expressing either 3xFlag-tagged Snx14 or GFP, conducted anti-Flag immuno-precipitation, and Western blotted the IP lysates for endogenous SCD1. SCD1 was detected in the Snx14-Flag sample but not GFP-Flag (**Figure 4.6A**). Intriguingly, Snx14-Flag co-IPed SCD1 both with and without palmitate addition (**Figure 4.6A**). To determine whether this interaction was specific, we Western blotted for PLIN3 which was highly enriched in the Snx14 APEX2-proteomics (**Figure 4.3D, Supplementary Figure 4.3A**). Notably, PLIN3 was not detected in the Snx14 co-IP lysate (**Supplementary Figure 4.6A**), suggesting Snx14 interaction with SCD1 was specific.

Next we dissected what regions of Snx14 were sufficient to co-IP SCD1. We used cell lines stably expressing Flag-tagged N-terminal half of Snx14 encoding the transmembrane (TM), PXA, and RGS domains (Snx14$^{N}$), or a C-terminal half with the PX and C-Nexin domains (Snx14$^{PXCN}$) (**Figure 4.6B**). Co-IP experiments revealed that Snx14$^{N}$, but not Snx14$^{PXCN}$, was sufficient to interact with SCD1 (**Figure 4.6C**). To test whether the Snx14:SCD1 interaction required SCD1 desaturase activity, we conducted a co-IP of SCD1 with full length Snx14 (Snx14$^{FL}$) in the presence of SCD1i (Uto et al. 2011). Inhibited SCD1 still co-IPed with Snx14$^{FL}$, indicating this interaction did not require SCD1 enzymatic activity (**Figure 4.6C**).

Given Snx14 could co-IP endogenous SCD1, we tested whether this interaction occurred in intact cells. We exploited the previous observation that Snx14 enriches at ER-LD contacts following oleate addition (Datta et al. 2019). Given this, we queried whether Snx14 over-expression was sufficient to drive the accumulation of SCD1 at ER-LD interfaces. Immunofluorescence (IF) labeling of endogenous SCD1 in non-oleate treated cells transfected with Snx14-EGFP revealed SCD1 co-localization with Snx14 throughout the ER network (**Figure 4.6D, Supplementary Figure 4.6B**). Moreover, following oleate addition, Snx14-EGFP accumulated at ER-LD contacts and co-localized with SCD1 foci also enriched at these sites (**Figure 4.6D**, **red arrows,**
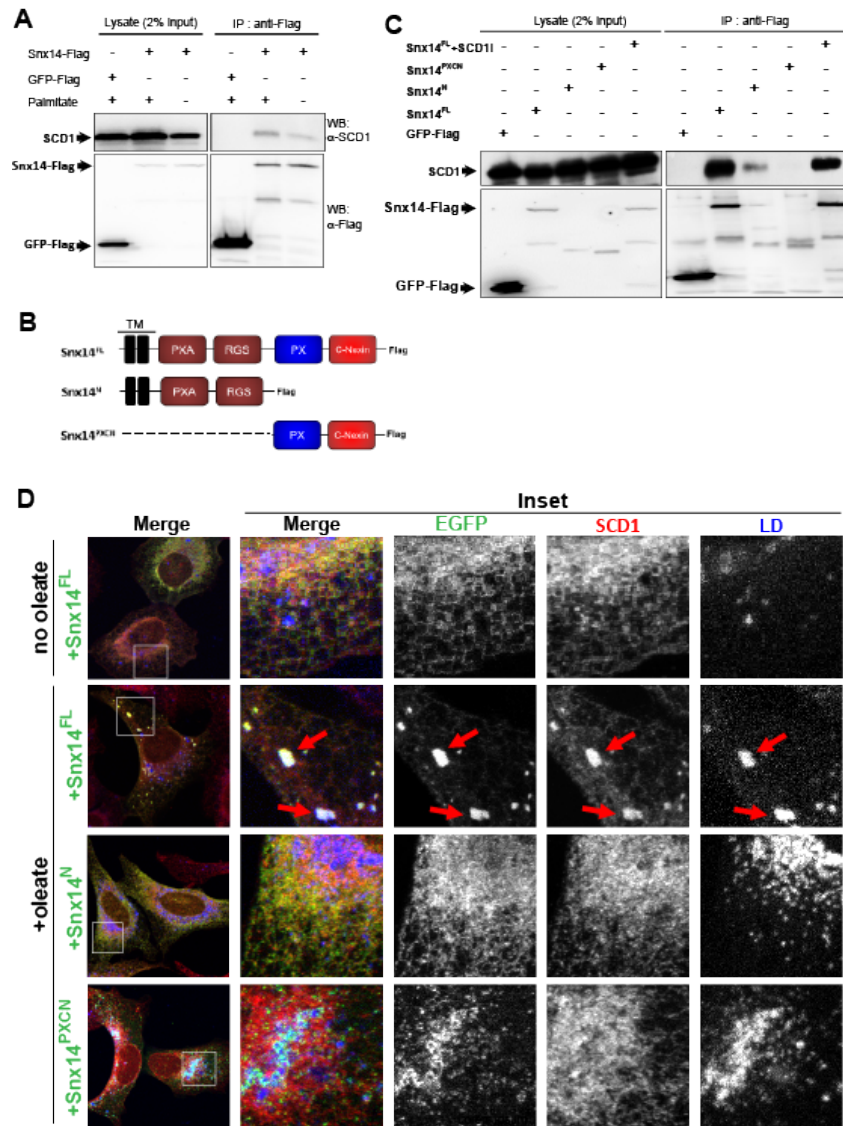
**Figure 4.6: Snx14 interacts with SCD1 in the ER network**

**A.** Western blotting with anti-Flag and anti-SCD1 antibody of 2% input lysate from GFP-Flag and Snx14-Flag expressing cells with and without palmitate treatment reveals relative expression of GFP-Flag, Snx14-Flag and SCD1. Co-immunoprecipitation (Co-IP) of SCD1 with Flag tagged constructs reveals presence of SCD1 in Snx14-Flag and not GFP-Flag enriched beads when western blotted with anti-Flag and anti-SCD1 antibody.

**B.** Schematic diagram of Snx14 fragments C-terminally tagged with either 3XFlag or EGFP. Snx14$^{FL}$ depicts the full length human Snx14. Snx14$^{N}$ is the N-terminal fragment that spans from the beginning and includes TM, PXA and RGS domains. Snx14$^{PXCN}$ is the C-terminal half including the PX domain and C-Nexin domains.

**C.** Lanes represent 2% input and IP from GFP-Flag, all 3XFlag tagged Snx14 constructs (Snx14$^{FL}$, Snx14$^{N}$, Snx14$^{PXCN}$) and SCD1i treated Snx14$^{FL}$-3XFlag expressing U2OS cells. Western blotting with anti-Flag and anti-SCD1 antibody reveals relative expression of all the Flag tagged constructs and SCD1 in all these samples.

**D.** IF staining of U2OS cells expressing Snx14$^{FL}$, Snx14$^{N}$, Snx14$^{PXCN}$ with anti-EGFP (green), anti-SCD1(red) antibody and imaged with confocal microscope. LDs were stained with MDH (blue). The cells were either untreated or treated with oleate. Scale bar = 10 μm.

**Supplementary Figure 4.6B**). In contrast, expression of Snx14$^{PXCN}$-EGFP, which accumulates around LDs (Datta et al. 2019), failed to colocalize with SCD1 foci, consistent with Snx14$^{PXCN}$ being insufficient to co-IP SCD1 (**Figure 4.6D, Supplementary Figure 4.6B**). Snx14$^{N}$-EGFP localized throughout the ER network following oleate, since it lacks the previously identified LD-targeting region in the CN domain (Datta et al. 2019), and this co-localized with SCD1 throughout the ER network but did not drive SCD1 foci at ER-LD contacts, consistent with co-IP results (**Figure 4.6D, Supplementary Figure 4.6B**). Collectively, this suggests that Snx14 and SCD1 interact in intact cells.
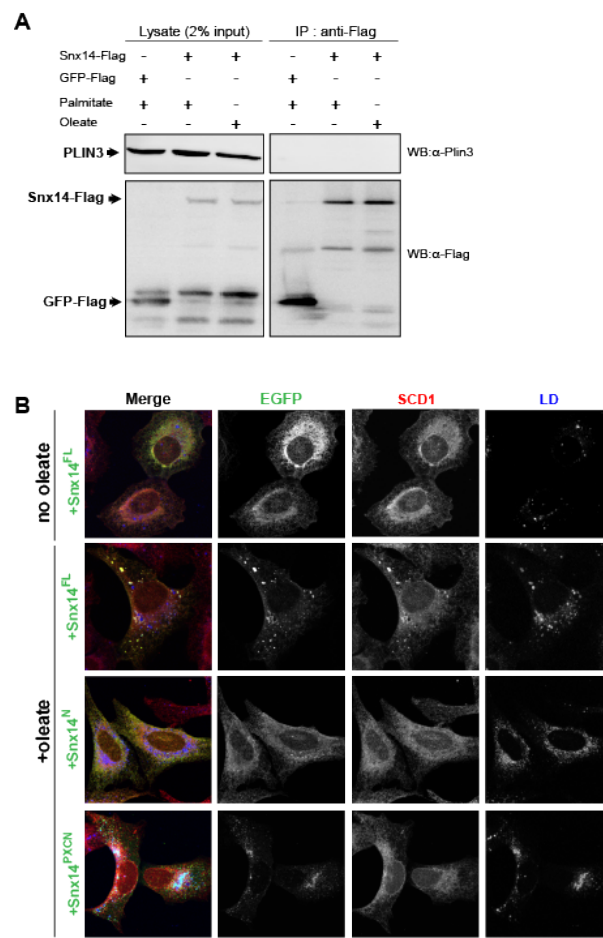


**Supplementary Figure 4.6**
A.  Lanes represent 2% input and IP from GFP-Flag and Snx14$^{FL}$-3XFlag expressing U2OS cells with either oleate or palmitate treatment. WB with anti-Flag and anti-PLIN3 antibody reveals relative expression of all the Flag tagged constructs and PLIN3 in all these samples. Snx14$^{FL}$-3XFlag similar to GFP-Flag could not co-IP PLIN3.
B.  IF staining of U2OS cells expressing Snx14$^{FL}$, Snx14$^{N}$, Snx14$^{PXCN}$ with anti-EGFP (green), anti-SCD1(red) antibody and imaged with confocal microscope. LDs were stained with MDH (blue). The cells were either untreated or treated with oleate.  Scale bar = 10 μm.

**Snx14 loss does not impact SCD1 enzymatic activity, but Snx14 requires FA-binding PXA domain for function**

To dissect how the Snx14-SCD1 interaction may contribute to SFA metabolism at the ER, we examined whether Snx14 regulates SCD1 enzymatic activity. We directly assayed SCD1 activity *in vitro* via a well-established radiolabel-based desaturase assay (Piccolis et al. 2019). We pulsed microsomal fractions isolated from WT and *SNX14-KO* cells with $(9,10\text{-}^3H)$-stearoyl-CoA, a SCD1 substrate. SCD1 activity releases free $^3H$ when stearoyl-CoA is mono-unsaturated, which can be directly detected by scintillation counting. As a positive control, we treated samples with SCD1i, and detected a significant decrease in free $^3H$ indicating reduced SCD1 activity (**Figure 4.7A**). Although better experimental techniques are needed to directly monitor SCD1 activity, initial experiments show no significant change in relative SCD1 activity in *SNX14-KO* cells, suggesting Snx14 may not be required for SCD1 activity.

Since Snx14 yeast ortholog Mdm1 had previously been shown to directly bind to FAs *in vitro* via its PXA domain (Hariri et al. 2019), we next interrogated whether Snx14 requires its PXA domain for function. We generated cell lines stably expressing Snx14 lacking its PXA domain (Snx14$^{FL\Delta PXA}$) (**Figure 4.7B**), and queried whether this construct could co-IP with SCD1 as well as process the accumulated FFAs in *SNX14-KO* cells following palmitate exposure. Intriguingly, Snx14$^{\Delta PXA}$ could co-IP with SCD1 (**Figure 4.7C**). However, in contrast to *SNX14-KO* cells expressing full length Snx14 (Snx14$^{FL}$) which could mitigate the FFA accumulation, *SNX14-KO* expressing Snx14$^{FL\Delta PXA}$ failed to do so, indicating that the PXA domain was required for FFA processing (**Figure 4.7D**). Here also we confirmed that FA uptake was not altered by expressing Snx14$^{FL}$ or Snx14$^{FL\Delta PXA}$ in *SNX14-KO* indicating that the elevated FFA accumulation in *SNX14-KO* cells expressing Snx14$^{FL\Delta PXA}$ was not associated with FA uptake (**Supplementary Figure 4.5E**). Next, we assayed whether the PXA domain was necessary to rescue *SNX14-KO* cell viability following palmitate exposure. Indeed, Snx14$^{FL\Delta PXA}$ failed to rescue *SNX14-KO* cells, indicating the PXA was required for Snx14-mediated protection from palmitate (**Figure 4.7E**).
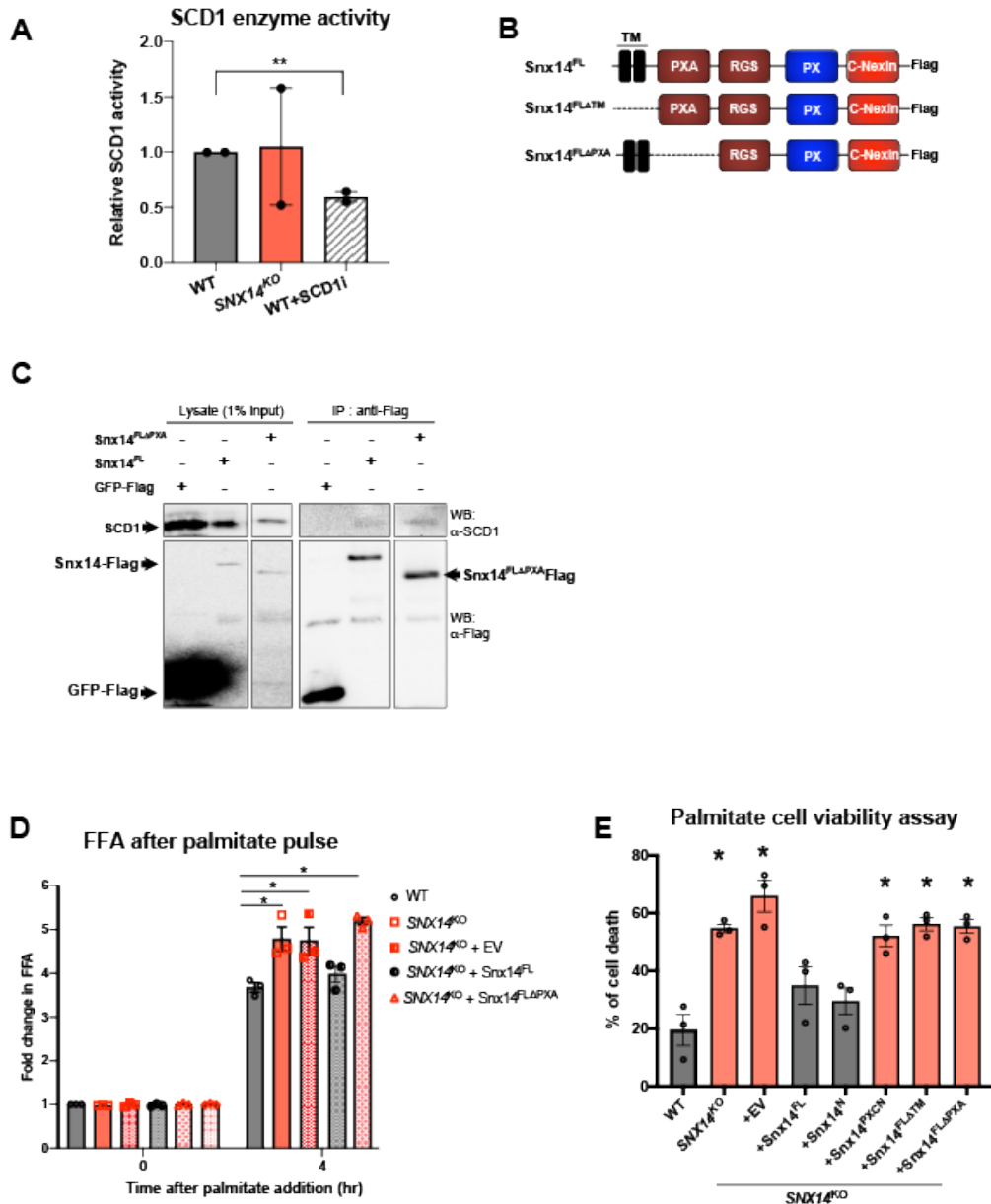
**Figure 4.7: Snx14 loss does not impact SCD1 enzymatic activity, but Snx14 requires FA-binding PXA domain for function**

**A.** SCD1 enzyme activity quantified in WT, *SNX14-KO* and SCD1i treated WT relative to WT cells. Values represent mean±SEM (n=2, \*\*p<0.001, multiple t-test by Holm-Sidak method with alpha = 0.05).

**B.** Schematic diagram of Snx14 fragments C-terminally tagged with 3X Flag. Snx14$^{FL}$ depicts the full length human Snx14. Snx14$^{FL\Delta PXA}$ and Snx14$^{FL\Delta TM}$ are the full length Snx14 excluding the PXA domain and TM domain respectively.

**C.** Lanes represent 1% input and IP from GFP-Flag, 3XFlag tagged Snx14 constructs (Snx14$^{FL}$, Snx14$^{FL\Delta PXA}$, Snx14$^{FL\Delta TM}$) expressing U2OS cells. Western blotting with anti-Flag and anti-SCD1 antibody reveals relative expression of all the Flag tagged constructs and SCD1 in all these samples. Snx14$^{FL\Delta PXA}$ could co-IP SCD1 similar to Snx14$^{FL}$ whereas Snx14$^{FL\Delta TM}$ could not pull down SCD1.

**D.** Quantification of fold change in FFA (normalized to cell pellet weight) relative to untreated WT from TLC of whole cell neutral lipids extracted from WT, *SNX14-KO*, *SNX14-KO* cells expressing either EV, Snx14$^{FL}$, or Snx14$^{FL\Delta PXA}$ which are either untreated or treated with palmitate for 4hr. Values represent mean±SEM (n=3, \*p<0.01, multiple t-test by Holm-Sidak method, alpha = 0.05).

**E.** Cell death (%) after exposure to 500µM of palmitate in WT, *SNX14-KO*, and on re-addition of empty vector (EV), Snx14$^{FL}$, Snx14$^{N}$, Snx14$^{PXCN}$, Snx14$^{FL\Delta TM}$, Snx14$^{FL\Delta PXA}$ to *SNX14-KO*. Values represent mean±SEM. Significance test compared with WT is denoted as \* (n=3, \*p<0.01, multiple t-test analysis by Holm-Sidak method with alpha = 0.05).

In line with this, *SNX14-KO* cells expressing Snx14$^N$ were also protected from palmitate, suggesting this minimal Snx14 fragment which contains a PXA domain is sufficient for palmitate protection.

However, a Snx14 construct which lacked the N-terminal TM domain but encoded all other domains (Snx14$^{FL\Delta TM}$) could not rescue the *SNX14-KO* cell viability, indicating that TM-mediated ER association is also required for Snx14 function (**Figure 4.7B, E**). Collectively, this suggests that Snx14 loss does not impact SCD1 enzymatic activity *in vitro*, but implies that the Snx14 PXA domain may interact with FAs at or near the ER network in a manner that promotes SCD1-mediated FA processing.

**Discussion**

FAs are essential cellular components that act as energy substrates, biomembrane components, and key signaling molecules. These functions are dependent on the chemical features of FAs such as their chain length and saturation degree, which influence membrane fluidity and impact organelle structure and function (Piccolis et al. 2019; Zhu et al. 2019). Lipid homeostasis depends on FA processing and channeling to specific organelle destinations. When cells experience elevated intracellular FA levels, they respond by increasing FA processing and storage. Excess FAs are incorporated into neutral lipids and stored in LDs, which protect cells from lipotoxicity (Olzmann and Carvalho 2019). Much of the machinery to achieve this resides at the ER, and proper ER-LD crosstalk by proteins such as Seipin and the FATP1-DGAT2 complex is essential to maintain lipid homeostasis (Szymanski et al. 2007; Salo et al. 2019; Xu et al. 2012). Our earlier work revealed a role for Snx14 in ER-LD crosstalk, the loss of which contributes to the cerebellar ataxia disease SCAR20 for unknown reasons (Datta et al. 2019). Here, we report major candidates that comprises the proteomic composition of Snx14-associated ER-LD contacts (**Supplementary Table 1**), and provide mechanistic insights into the function of Snx14 in FA metabolism. We find that Snx14 loss impacts the ability of cells to maintain proper lipid saturation profiles. In line with this, following SFA exposure *SNX14-KO* cells display defects in ER morphology, FFA

accumulation and elevated SFA incorporation into membrane glycerophospholipids, lyso-phospholipids, and TG, which ultimately impacts cell homeostasis.

Utilizing APEX2-based proteomics analysis, we reveal the protein composition of Snx14-positive ER-LD contacts formed during oleate treatment. Notably, these contacts contain proteins associated with the LD surface such as PLIN2, PLIN3, and PNPLAP2. We also detect numerous proteins involved in FA processing (ACSL4, SCD1) and lipid/sterol biosynthesis (LPCAT1, LPCAT3, SOAT1), indicating that ER-LD contacts act as lipogenic ER sub-domains for several lipid species, as well as hotspots for FA processing. These proteomics reveal many proteins previously identified through a similar APEX-based proteomics study which targeted APEX to the LD surface, providing consistency in the method, as well as underscoring the tight functional association between LDs and the ER network (Bersuker et al. 2018). Among these proteins, we focused on investigating the functional interplay between Snx14 and SCD1-associated SFA metabolism, which provided important insights in understanding the hypersensitivity of *SNX14-KO* cells to palmitate exposure.

Through lipidomic analysis and biochemistry, we show that Snx14 loss phenotypically mimics aspects of the enzymatic inhibition of Δ-9-FA desaturase SCD1, which catalyzes the oxidization of SFAs to MUFAs (**Figure 4.8**) (Paton and Ntambi 2009). In line with this, SCD1 over-expression can rescue palmitate sensitivity in Snx14-deficient cells. We also show by co-IP that SCD1 and Snx14 can interact, and that Snx14 over-expression can promote SCD1 enrichment at ER-LD contacts under distinct metabolic conditions. While we cannot conclusively say that Snx14 and SCD1 directly interact at the ER, the data presented are consistent with a model where Snx14 may promote SCD1 function to maintain ER homeostasis. One possibility is that Snx14 acts as an organizational scaffold for SCD1 within the ER network, enabling SCD1 to make contact with FA substrates. In agreement with this, Snx14 requires its FA-binding PXA domain to function, implying that Snx14 could bind FA substrates and present them to SCD1 during periods of elevated FA influx. Initial results with existing technique showed no change in SCD1 enzymatic activity with loss of Snx14, though more study is required to completely rule out the role of Snx14 in

directly regulating SCD1 activity. We also cannot rule out the possibility that Snx14 may interact or present FAs to other enzymes in the ER network similar to SCD1, which could explain other alterations in the lipidomics profile of *SNX14-KO* cells.

Snx14 is highly conserved in evolution, and related studies of Snx14 orthologs provide mechanistic insights into Snx14's role in lipid homeostasis. *Drosophila* ortholog Snz functionally interacts with SCD1 ortholog DESAT1 in the adipocyte cell periphery, a sub-cellular region rich in FA processing (Ugrankar et al. 2019). Similarly, yeast ortholog Mdm1 functions in FA activation and LD biogenesis near the yeast vacuole (Hariri et al. 2018; Hariri et al. 2019). As such, Mdm1-deficient yeast are sensitive to high dosages of exogenous FAs. Studies of both Snz and Mdm1 also reveal these proteins localize to specific sub-regions of the ER network, and thereby help to demarcate ER sub-domains through their inter-organelle tethering capabilities. Thus, an emerging possibility is that Snx14 family proteins act as organizational scaffolds within the ER network, and recruit enzymes into ER sub-domains to more efficiently process lipids.

Collectively, our observations provide a framework for understanding how Snx14 loss contributes to the cerebellar ataxia disease SCAR20. A growing number of neurological diseases are attributed to loss of proteins that function in ER-localized lipid metabolism or in the maintenance of ER architecture (Blackstone, O'Kane, and Reid 2011; Yamanaka and Nukina 2018; Adibhatla and Hatcher 2008). Our data are consistent with a model where Snx14 loss perturbs the ability of cells to maintain FA metabolism and membrane lipid composition, ultimately elevating SFA levels and saturated fatty acyl chain incorporation in membrane lipids. Such alterations will ultimately effect membrane fluidity, organelle function, and contribute to cellular lipotoxicity and the progressive death of cells like neurons, a pervasive symptom of SCAR20 disease (Thomas et al. 2014; Akizu et al. 2015). Additionally, although we focused our analysis here on the interplay between Snx14 and SFA metabolism, the APEX2-based proteomics and lipidomics analysis will provide insights into understanding proteins and lipogenic reactions at ER-LD contacts.
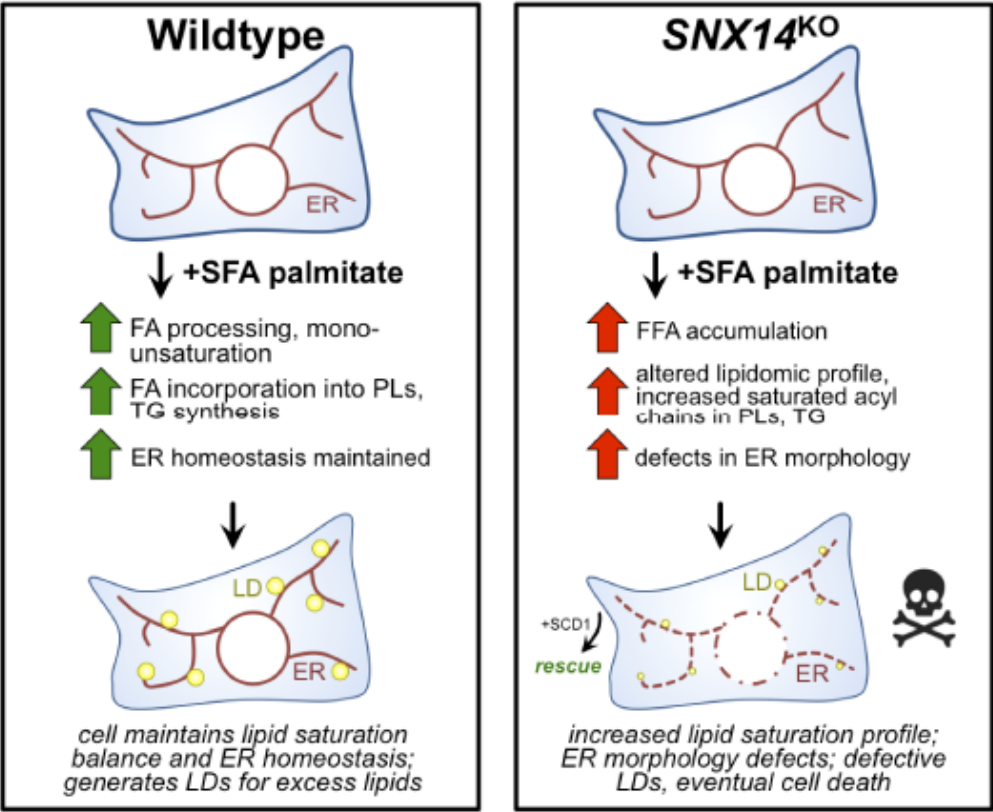
**Figure 4.8:** Working model for Snx14 in maintaining ER lipid homeostasis when treated with excessive SFAs.

# CHAPTER FIVE

# Materials and Methods

## Cell culture

U2OS cells were cultured in DMEM (Corning, 10-013-CV) media supplemented with 10% Cosmic Calf Serum (Hyclone, SH30087.04) and 1% Penicillin Streptomycin Solution (100X, Corning, 30-002-Cl). The cells were passaged when they reached 80%-90% confluency with 0.25% Trypsin-EDTA (Corning, 25-053-Cl). To promote LD biogenesis, cells incubated with 500 μM of OA, and for all other FFA treatment, the cells were incubated with 500 μM of either oleate or palmitate for the indicated period of time. For the cell viability assay, cells were treated with different concentration of FFA (250, 500, 750, 1000 μM) for 48 hours. In all the experiments the FFAs were conjugated with fatty acid free BSA (Sigma, A3803) in the ratio of 6:1.

## Chemicals and reagents

For cell treatments, the following reagents were used for indicated periods of time – (1) SCD inhibitor (Abcam, ab142089) – 4 μM in DMSO (2) Myriocin (Sigma, M1177) – 50 μM in DMSO (3) Tunicamycin (Sigma) – 5 μg/ml in DMSO for 6hr (4) Etomoxir (Cayman chemical, 11969) – 10 μM in DMSO (5) DGAT inhibitors include DGAT1 inhibitor (A-922500, Cayman chemical ,10012708) – 10 μM in DMSO, and DGAT2 inhibitor (PF-06424439, Sigma, PZ0233)– 10 μM in $H_2O$ (6) IRE1 inhibitor 48c (Sigma, SML0949) – 64 μM in DMSO (7) PERK inhibitor I, GSK2606414 (EMD Millipore, 516535) - 30 nM in DMSO (c) Caspase 6/8 inhibitor (Sigma, SCP0094) – 40 μM in DMSO.

## Cloning and transient transfection

All the Snx14 constructs i.e. SNX14$^{FL}$, SNX14$^{N}$ and SNX14$^{PXCN}$, Snx14$^{PX}$, Snx14$^{CN}$, Snx14$^{PXCN\Delta H}$, Snx14$^{FL\Delta H}$ tagged with EGFP at their C-termini were generated after PCR amplification of fragments of interest from Snx14 generated from cDNA library and cloning them into pEGFP-N2. Seipin$^{mcherry}$ was PCR amplified from cDNA library and was then cloned into

pEGFP-N2 vector with a mCherry tag at the C-terminal and insertion of a stop codon before EGFP. Snx14-EGFP-APEX2 was cloned in pCMV vector for transient transfection. The plasmids resuspended in optimem (gibco, 31985-070) were transiently transfected into U2OS cells using either PolyFect Transfection reagent (Qiagen, 301105) or PEI-Max Transfection reagent (Polysciences, 24765) for 48 hours prior to experiments.

## Generation of stable cell lines

All the C-terminally 3X Flag-tagged constructs i.e., $SNX14^{FL}$, $SNX14^{N}$ and $SNX14^{PXCN}$ were generated following PCR amplification of Snx14 from cDNA library and cloning into the pMXs-3-FLAG vector. U2OS cells were transformed with retroviral vectors expressing Puromycin-expressing plasmids. Cells expressing the plasmid of interest were selected via Puromycin-resistance, and expanded to generate stable cell lines.

### Lentiviral transduction

$Snx14^{FLΔTM}$ and $Snx14^{FLΔPXA}$, with 3XFlag tag at the C-terminal, were generated following PCR amplification using $Snx14^{FL}$-3XFlag and cloning into the plvx lentiviral vector with puromycin (puro) resistance cassette. Similarly GFP-Flag plasmid was cloned into plvx-puro vector. The cloned plasmids and lentiviral packaging plasmids were transfected together into 293T cells to generate lentivirus which were transduced into U2OS cells. Puromycin was used to select and expand the transduced cells expressing the plasmid. The generated stable cell lines were stored in liquid nitrogen before their use in experiments.

### Generation of APEX2 tagged cell lines

$Snx14^{EGFP}$-APEX2 was generated by first PCR amplifying full length Snx14 from cDNA library, EGFP-APEX2 from pcDNA3-Connexin43$^{EGFP-APEX2}$ (Addgene plasmid – 49385) and then cloning into one of the lentiviral vectors, plvx with puromycin resistance cassette to perform lentiviral transduction as described above. Similarly, EGFP-APEX2-Sec61 and cyto-APEX2 which are also puromycin resistant was generated. cDNA library was used for PCR amplification of Sec61.

## Cell viability assay

The cell viability assay protocol was adapted from (Feoktistova, Geserick, and Leverkus 2016; Chu et al. 2015). Cells were seeded at ~40% confluency and maintained in cell culture media overnight in a 12 well plate. On the following day, the cells were treated with indicated concentration of FFA for 2 days. Then the cells were washed with PBS, fixed with 4% PFA, stained with 0.1% crystal violet (Sigma) for 30 mins, excess stain was washed, and then the stain from the surviving cells were extracted with 10% acetic acid, whose optical density (OD) was measured at 600 nm. The percentage of survival cells (cell viability) were quantified relative to the untreated cells whose OD measurement is set at 100% survival. The assay was performed thrice in triplicates.

## Immunofluorescent (IF) staining

Cells were fixed with 4% PFA solution in PBS for 15 mins at room temperature (RT). For immunofluorescent staining, fixed cells were washed with PBS, permeabilized with 0.2% NP40 in PBS at RT for 3 mins and then blocked in IF buffer (PBS containing 3% BSA, 0.1% NP40 and 0.02% sodium azide) for 40 mins. The cells were then incubated with primary antibody in IF buffer for 1 hour, washed thrice with PBS, next incubated with secondary antibody in IF buffer for 30 mins, given three washes with PBS and then mounted, which were then used for microscopic studies. The primary antibodies used are mouse anti-Hsp90B1 (1:300; Sigma, AMAb91019), rabbit anti-Snx14 (HPA017639), rabbit anti-EGFP (1:300), rabbit anti-Flag (1:200; Sigma, F7425), mouse anti-ACSL3 (1:200; Novus biologicals, H00002181-B01P). The secondary antibodies are donkey anti-mouse AF488 (Thermo Fisher, A21202) and donkey anti-rabbit AF594 (Thermo Fisher, A21207) used at a dilution of 1: 1000. LDs were visualized by staining the cells with MDH (1:1000; Abgent, SM1000a) for 15 mins. Nucleus was stained with 5 µM Syto® 85 orange fluorescent stain (Molecular Probes, S-11366).

## Confocal microscopy and image analysis

The images of the cells were taken using a 63X oil immersion objective in a Zeiss LSM 780 Confocal Microscope. Approx. 4 Z-sections of each image were taken.

ImageJ was used for the representation and quantification of images. The merged images were generated by max z-projection. For others one plane was shown. The MDH-stained blue LDs were grayscaled, inverted and the cell boundary was drawn with freehand line tool.

*Analysis of area covered by LDs*

The area covered by LDs were calculated using ImageJ (Fiji). Using ImageJ, the images with MDH stained LDs were grayscaled and inverted (Supplementary Figure 3.2A). The cell boundary was traced by a freehand line tool. To analyse the average area covered by LDs per cell, the following steps in ImageJ were used – 1) LDs were processed by using 'Subtract background' in 'Process'. Next in 'Process', we used 'Filter' to apply 'Gaussian blur'. To get rid of the background, we then subtracted the blurred image from the original in 'image calculator' in 'Process'. 2) We 'threshold'-ed the modified image and then applied 'analyse particles'. On treatment of WT and *SNX14-KO* cells overnight with exogenous FA (oleate/palmitate), the LDs in WT showed perinuclear clustering and was hard to distinguish one from the other. So, we quantified the average area covered by LDs which is an estimation of both size and numbers of LDs. For the rescue experiments, the cells which were transfected were selected, then the area covered by LDs in that cell was calculated and plotted.

*Analysis of LDs numbers*

The quantification of number of LDs was adapted from (Kassan et al. 2013). Again 'analyze particles' plugin of Image-J was used to calculate number of LDs below $5\mu m^2$. Due to the limitation of resolution and clustering effect of LDs, the number of LDs whose area was greater than $5\ \mu m^2$ were calculated from the sum total area covered by all the LDs divided by the mean area of LDs (i.e., $0.5\ \mu m^2$).

*Fluorescence colocalization analysis*

Pearson's coefficient (r) was quantified for all the z-stacks of the image after chosing a threshold value to exclude the background signal using Imaris Image Analysis software.

*Analysis of ER-LD contacts from TEM images*

The length of each detected contact made by an ER membrane with the LD (marked in blue in **Figure 3.4**) was calculated and normalized to the perimeter of the LD. These lengths were then plotted as dot plots.

*Analysis of ER morphology*

We quantified the ER morphology from 3 sets of experiments, imaging approx. 6 cells in one field of view and six fields of view in each experiment. This gave us ~100 cells to quantify the ER morphology which is grouped into four classes – (A) regular and intact ER (B) ER with partial fragmentation where the nucleus is still intact (C) fully fragmented ER, with distinct bulges where the nuclear envelope also disappeared, (D) the ER stain is soluble. Examples of A,B,C,D is shown in **Figure 4.2 A**. For each set of experiment, the percentage of cells of each class of ER morphology is quantified and plotted.

## DAB labeling of Snx14EGFP-APEX2

Cells stably expressing Snx14$^{EGFP-APEX2}$ were fixed with 2.5% glutaraldehyde in 'cacodylate buffer' (100 mM sodium cacodylate with 2mM Cacl2, pH 7.4) for 30 mins. DAB tablets (Sigma, D5905) were dissolved in PBS to a final concentration of 0.5 mg/ml DAB and 10mM of 30% H2O2 was added. The fixed cells were incubated with the DAB solution for 30 mins at RT. The cells were then washed thrice with PBS, then they were imaged by brightfield microscope to test expression and activity of APEX2. Then the cells were processed to be imaged by electron microscope.

## Electron Microscopy

The cell lines of interest were cultured under desired condition and processed in the UT Southwestern Electron Microscopy Core Facility. Cells were fixed on MatTek dishes with 2.5% (v/v) glutaraldehyde in 0.1M sodium cacodylate buffer. After three rinses in 0.1 M sodium cacodylate buffer, they were post-fixed in 1% osmium tetroxide and 0.8 % $K_3[Fe(CN_6)]$ in 0.1 M

sodium cacodylate buffer for 1 h at room temperature. Cells were rinsed with water and en bloc stained with 2% aqueous uranyl acetate overnight. Next, they were rinsed in buffer and dehydrated with increasing concentration of ethanol, infiltrated with Embed-812 resin and polymerized in a 60°C oven overnight. Blocks were sectioned with a diamond knife (Diatome) on a Leica Ultracut UCT (7) ultramicrotome (Leica Microsystems) and collected onto copper grids, post stained with 2% aqueous uranyl acetate and lead citrate. Images were acquired on a Tecnai $G^2$ spirit transmission electron microscope (FEI) equipped with a $LaB_6$ source using a voltage of 120 kV. The APEX tagged samples were processed for EM as described above except that they were not post stained and the methods used were based on the protocol from (Martell et al. 2012).

## Generation of *SNX14-KO* U2OS cell lines using CRISPR-Cas9

In U2OS cells, the Snx14 gene was targeted with the guide RNA 5' – GAAGCAGAACAGCGGGTACTGG-3' using CRISPR-Cas9 system. Single cells were then seeded in one well of a 96 well plate and colonies were expanded and loss of Snx14 was validated using Western blot. These clones were next sequenced and the one which generates a very short peptide of 25 residues was selected for experiments.

## Neutral lipid analysis by thin layer chromatography (TLC)

Lipids were extracted from cultured cells using a protocol adapted from Bligh and Dyer (1959) (20). Cells cultured in complete media were washed twice in PBS and then scraped and collected and their weights were measured. The cell pellets were lysed by vortexing in the presence of chloroform, followed by methanol, 500 mM NaCl in 0.5% acetic acid to the final concentration such that the ratio of chloroform: methanol: water was 2:2:1.8. The suspension was centrifuged at 4000 rpm for 15 min at 4°C and the bottom chloroform layer, comprising of the lipids, was collected. This lipid layer was dried and then again resuspended in chloroform to a final concentration normalized to the initial cell pellet weight. Thin layer chromatography (TLC) was used to separate the extracted lipids. Hexane: diethyl ether: acetic acid (80:20:1) was used as a solvent to separate neutral lipids extracted from the cells. The bands in the TLC plates were

developed by spray-staining with 3% copper acetate prepared in 8% phosphoric acid and incubating in the oven at 135°C for ~1hr. Plates were resprayed and reheated as needed to visualize lipids. Developed TLC plates were scanned and then processed for quantification using Fiji (ImageJ). On each plate we ran a serial dilution of standard neutral lipid mixture of known concentrations to create a standard curve between the lipid mass vs. the band intensity to estimate the lipid mass from the samples of interest.

**Fluorescent acyltransferase activity assay**

This fluorescent based assay to measure DGAT activity invitro was based on the protocol adapted from (McFie and Stone 2011). In short, total membranes were isolated from cells, 80 μg of which was used with NBD-palmitoyl CoA as substrate to react with DAG added externally to produce NBD-TAG. The fluorescent neutral lipids were then detected by TLC where cyclohexane:ethylacetate (1:2) was used as solvent and quantified using BioRad fluorescent imaging system.

**Lipid droplet isolation**

Total LDs were isolated from U2OS cells treated with OA overnight according to the protocol adapted from (Ding et al. 2013) . In brief, cells from eight 150 mm dishes were washed twice with ice-cold PBS and were then collected by scraping them into ice-cold PBS. The cells were pelleted by centrifugation at $1000\,g$ for 5 min at 4°C, resuspended in Buffer A (20 mM tricine, 250 mM sucrose, pH 7.8) containing 0.2M PMSF and protease inhibitor cocktail (ThermoFisher, A32965) and kept on ice for 20 min. The cells were disrupted using Nitrogen bomb at a pressure of 35 bar $N_2$ on ice for 15 minutes. The homogenate was centrifuged at $3000\,g$ for 10 min at 4 °C and the supernatant which is the PNS (Post-nuclear supernatant) fraction was transferred into SW 40 Ti tubes. 1% was retained for gel loading control and the rest was resuspended in 10ml of Buffer A. Then 2 ml of Buffer B (20 mM HEPES, 100 mM KCl, 2 mM MgCl2, pH 7.4) was loaded onto the top of the PNS and the gradient was centrifuged at $182{,}000\,g$ for 1 hr at 4 °C. The topmost white layer which consists of lipid droplets was collected to a 1.5 ml microcentrifuge tube. The middle

part which is the cytosol and the pellet that is the membrane fraction were also collected. The LD and membrane fractions collected were diluted respectively in 200 µl and 500 µl of buffer B containing protease inhibitor cocktail (ThermoFisher, 78430) and 0.2 µM PMSF. For Western Blotting (Figure 3.2 A, C), 1% PNS, 1% cytosol, 10% membrane (50 µl) and 25% LD fraction (50 µl) were loaded.

For quantitative densitometry, relative protein expression was quantified by analyzing band intensities using ImageJ (Fiji). For determining LD/membrane protein ratios (as in Supplementary Figure 3.2B, Figure 3.2C), equal volumes of total membrane (10%) and LD fractions (25%) were loaded onto the gel. To correct for their dilutions, the membrane fraction signals were multiplied by 2.5.

## Western blot

Samples were prepared in 2X Laemmli Sample Buffer (Bio-Rad, 161-0737) supplemented with 5% -mercaptoethanol and heated at $95^0$C for 10 mins and then run on a polyacrylamide gel. The proteins were then transferred onto a PVDF membrane. Next the membrane containing proteins were blocked with 5% milk in TBS-0.1%Tween (TBST) buffer for 1 hr at RT, incubated overnight with primary antibodies, washed thrice with TBST and then incubated with HRP conjugated secondary antibodies (1:5000) and developed with Clarity™ Western ECL blotting substrate (Bio-Rad, 1705061) and imaging with X-ray film. The primary antibodies used for western blot were Rab anti-EGFP (1:2000), Mouse anti-Hsp90B1(1:1000), Rab anti-actin(1:1000), Mouse anti-ADRP(1:50; Fitzergald), Mouse anti-Flag(1:1000), Rab anti-Snx14(1:400; Sigma-Aldrich HPA017639), Rab anti-SCD1 (1:500), guinea-pig PLIN3 (Progen, GP32), streptavidin-HRP (1:1000; Thermo Scientific, S911). For company sources of antibodies, please refer to above IF section.

**siRNA transfection**

Cells were transfected with Neg siRNA (Ambion, cat# AM4611), Snx14 siRNA (Ambion cat# 4392420, ID# s32927) and ACSL3 siRNA (Ambion, cat# 4390824, ID# s4999, s4997) using Lipofectamine 2000 (Invitrogen, 11668-019) in optimem (gibco, 31985-070). After 6 hours, the transfected media was changed to complete media for another 48 hours prior to any experiments.

**RNA extraction and qRT-PCR**

To extract RNA, tissue culture cells were solubilized in TRIzol and collected from dishes, then treated with chloroform and centrifuged at 12000g for 15mins. To precipitate RNA, the upper colorless aqueous layer was collected, and isopropanol was added. Next, the supernatant was discarded and the RNA precipitate was washed by ethanol, air-dried and resuspended in RNase-free water. This RNA was used to generate cDNA using Bio-Rad commercial kit (iScript cDNA synthesis kit 1708891). The cDNA was used for qPCR reaction to analyse spliced xbp1 (s-xbp1) mRNA level which is an indicator of UPR activity that results from ER stress. Cells treated with tunicamycin (5 μg/ml) for 6 hr was used as a control for UPR activity. The internal control used for the qPCR reaction was β-actin (actb). The primers used for qPCR were Kicq predesigned primers (Sigma-Aldrich).

**Analysis of rate of FA uptake**

Cells were treated with a mix of 200 μM non-radiolabeled palmitate (BSA conjugated at 6:1) and 0.15Ci [1-$^{14}$C] palmitic acid (American Radiolabeled Chemicals, ARC 0172A) conjugated with 10M BSA for 15, 30, 60 mins. Following the treatment, the cells were solubilized with RIPA lysis buffer. The $^{14}$C counts per min of each sample was calculated in a scintillation counter. The radioactive counts was normalized to protein concentration of the samples quantified by Bradford assay.

## Microsome isolation

The cell pellets were dissolved in 1ml cell lysis buffer (20 mM tricine and 250 mM sucrose, 1mM EDTA, pH 7.8) containing protease inihibitor cocktail (ThermoFisher, 78430). The resuspended cells were then dounce homogenized and centrifuged for 10 mins at 8000 g. The supernatant was collected and centrifuged for 1 hr at 100,000 g. The resultant microsomal pellet was resuspended in 0.1 M PK buffer (0.1 M K2HPO4 buffer set at pH 7.2 with NaH2PO4 solution).

## SCD1 enzyme activity

The protocol was provided by Dr. James Ntambi's lab and was also adapted from (Piccolis et al. 2019). In brief, we made a reaction mix consisting of 0.03 mM stearoyl-CoA (Sigma, S0802), 1 Ci/ml radiolabelled [9,10-$^3$H] stearoyl-CoA (American Radiolabeled Chemicals, ART 0390), 2 mM NADH (Sigma, N8129) in 0.1 M PK buffer (0.1 M K2HPO4 buffer set at pH 7.2 with NaH2PO4 solution). 1.5 mM of stearoyl-CoA stock was prepared in cold and fresh everytime in 10 mM sodium acetate in 50% ethanol solution. The reaction assay consisted of 100 μg microsomes in 0.1 M PK buffer and 180 μl of premix. 4 μM SCDi was added as a control sample prior to the reaction. The reaction was done at 37°C for 30 mins, after which 200 μl of 6% perchloric acid was used to quench the reaction. Next 700 μl of 10% (w/v) charcoal dissolved in PBS was added to sediment the unused substrate. The sample was vigorously vortexed to mix and then centrifuged at 13000 rpm for 10 mins. The radioactive $^3$H following the SCD1 enzyme activity released in the aqueous phase which was counted in a scintillation counter. The results were quantified as $^3$H counts per min as fold change relative to WT microsomes.

## APEX2 dependent biotinylation

This protocol was modified from (Hung et al. 2016). In brief, U2OS and HEK293 cells expressing APEX2 tagged constructs and non-APEX2 construct (negative control) were incubated with 500 μM biotin-phenol (BP) (Adipogen, CDX-B0270-M100) for 30 mins and 1mM H2O2 was added for 1 min to biotinylate proteins proximal (labeling radius of ~20 nm) to the expression of APEX2 tagged construct. The biotinylation reaction was quenched after 1 min by washing the cells thrice

with a quencher solution (10 mM sodium ascorbate, 5 mM Trolox and 10 mM sodium azide solution in DPBS).

To visualize the biotinylated proteins, the cells were IF-stained with streptavidin-alexa 647 (Thermofisher Scientific, S21374) during incubation with secondary antibody and then imaged using confocal microscopy.

To identify the biotinylated proteins, immunoprecipitation and mass spectrometry techniques were used. After the labelling reaction, the cells were scraped in quencher solution and lysed in RIPA lysis buffer consisting of protease inhibitor cocktail (ThermoFisher, 78430), 1 mM PMSF and quenchers. The lysates were vortexed vigorously in cold for 30 mins and cleared by centrifuging at 10,000g for 10 mins at 4°C. The cell lysate was then dialysed using Slide-A-Lyzer dialysis cassette (3500 MWCO, ThermoFisher Scientific) to remove unreacted free BP. The protein concentration was then measured using Pierce 660nm assay. 2 mg protein was incubated with 80 µl streptavidin magnetic beads (Pierce, 88817) for 1 hour at room temperature on a rotator. The beads were pelleted using a magnetic rack. The pelleted beads were washed with a series of buffers - twice with RIPA lysis buffer, once with 1 M KCl, once with 0.1 M $Na_2CO$, once with 2 M urea solution in 10 mM Tris-HCl, pH 8.0, and twice with RIPA lysis buffer. To elute the biotinylated proteins , the beads were boiled in 80 µl of 2X Laemmli Sample Buffer (Bio-Rad, 161-0737) supplemented with 2 mM biotin and 20 mM DTT. Some of the eluate was run in SDS page gel and Coomassie stained to visualize the amount of enriched protein. Some eluate was western blotted with streptavidin-HRP antibody to visualize protein biotinylation. The rest was processed for gel digestion and mass spectrometry (MS) analysis to identify the enriched biotinylated proteins.

**Immunoprecipitation (IP)**

To test co-IP of SCD1 with Snx14 constructs tagged with 3XFlag at the C-terminal, the cells expressing those Snx14 constructs were lysed in IPLB buffer (20mM HEPES, pH7.4, 150mM KOAc, 2mM Mg(Ac)2, 1mM EGTA, 0.6M Sorbitol,) supplemented with 1% w/v digitonin and protease inhibitor cocktail (PIC) (ThermoFisher, 78430), followed by pulse sonication. The lysate

is clarified by centrifugation at 10,000g for 10 mins. 2% of the supernatant was saved as the input. The rest of the supernatant was incubated with Flag M2 affinity gel (Sigma, A2220) for 2hrs at 4°C. The beads were then washed thrice with IPLB wash buffer (IPLB, 0.1% digitonin, PIC) and twice with IPLB without digitonin. The IPed proteins are eluted from the beads by incubating the beads with 400 μg/ml 3X Flag peptide in IPLB buffer for 30mins. The beads were spun down and the supernatant was collected. The supernatant and the input fraction was run in a SDS-page gel and western blotted for Flag constructs and SCD1.

## Lipidomic profiling methods

All the samples for lipidomic were processed by Dr. Jeff McDonald's group.

### Lipid analysis

All solvents were either HPLC or LC/MS grade and purchased from Sigma-Aldrich. All lipid extractions were performed in 16×100 mm glass tubes with PTFE-lined caps (Fisher Scientific). Glass Pasteur pipettes and solvent-resistant plasticware pipette tips (Mettler-Toledo) were used to minimize leaching of polymers and plasticizers. Fatty acid (FA) standards (FA(16:0($^2$H$_{31}$), FA(20:4ω6($^2$H$_8$)) and FA(22:6ω3($^2$H$_5$)) were purchased from Cayman Chemical, and used as internal standards for total fatty acid analysis by GC-MS. SPLASH Lipidomix (Avanti Polar Lipids, Alabaster, AL, USA) was used as internal standards for lipidomic analysis by LC-MS/MS.

### Total Fatty Acid Analysis by GC-MS

Aliquots equivalent to 200k cells were transferred to fresh glass tubes for liquid-liquid extraction (LLE). The lipids were extracted by a three phase lipid extraction (3PLE) (Vale et al. 2019). Briefly, 1mL of hexane, 1mL of methyl acetate, 0.75mL of acetonitrile, and 1mL of water was added to the glass tube containing the sample. The mixture was vortexed for 5 seconds and then centrifuged at 2671 $\times g$ for 5 min, resulting in separation of three distinct liquid phases. The upper (UP) and middle (MID) organic phases layers were collected into separate glass tubes and dried under N$_2$. The dried extracts were resuspended in 1mL of 0.5M potassium hydroxide solution prepared in methanol, spiked with fatty acid internal standards, and hydrolyzed at 80°C during 60

minutes. Hydrolyzed fatty acids were extracted by adding 1mL each of dichloromethane and water to the sample in hydrolysis solution. The mixture was vortexed and centrifuged at 2671 ×$g$ for 5 minutes, and the organic phase was collected to a fresh glass tube and dried under $N_2$. Total fatty acid profiles were generated by a modified GC-MS method previously described by *(Quehenberger, Armando, and Dennis 2011)*. Briefly, dried extracts were resuspendend in 50µL of 1% triethylamine in acetone, and derivatized with 50µL of 1% pentafluorobenzyl bromide (PFBBr) in acetone at room temperature for 25 min in capped glass tubes. Solvents were dried under $N_2$, and samples were resuspended in 500µL of isooctane. Samples were analyzed using an Agilent 7890/5975C (Santa Clara, CA, USA) by electron capture negative ionization (ECNI) equipped with a DB-5MS column (40m x 0.180mm with 0.18µm film thickness) from Agilent. Hydrogen was used as carrier gas and injection port temperature were set at 300°C. Fatty acids were analyzed in selected ion monotoring (SIM) mode. The FA data was normalized to the internal standards. Fatty acid with carbon length; C ≤ 18 were normalized to FA(16:0($^2H_{31}$)), C = 20 were normalized to FA(20:4 ω6($^2H_8$)), and C = 22 were normalized to FA(22:6 ω3($^2H_5$)). Data was processed using MassHunter software (Agilent). Abundance of lipids in each of the samples are normalized to cell number.

*Lipidomic analysis by LC-MS/MS*

Aliquots equivalent to 200k cells were transferred to fresh glass tubes for LLE. Samples were dried under $N_2$ and extracted by Bligh/Dyer (Blight and Dyer 1959); 1mL each of dichloromethane, methanol, and water were added to a glass tube containing the sample. The mixture was vortexed and centrifuged at 2671 ×$g$ for 5 min, resulting in two distinct liquid phases. The organic phase was collected to a fresh glass tube, spiked with internal standards and dried under $N_2$. Samples were resuspendend in Hexane.

Lipids were analyzed by LC-MS/MS using a SCIEX QTRAP 6500$^+$ equipped with a Shimadzu LC-30AD (Kyoto, Japan) HPLC system and a 150 × 2.1 mm, 5µm Supelco Ascentis silica column (Bellefonte, PA, USA). Samples were injected at a flow rate of 0.3 ml/min at 2.5% solvent B (methyl tert-butyl ether) and 97.5% Solvent A (hexane). Solvent B is increased to 5% during 3

minutes and then to 60% over 6 minutes. Solvent B is decreased to 0% during 30 seconds while Solvent C (90:10 (v/v) Isopropanol-water) is set at 20% and increased to 40% during the following 11 minutes. Solvent C is increased to 44% for 6 minutes and then to 60% during 50 seconds. The system was held at 60% of solvent C during 1 minutes prior to re-equilibration at 2.5% of solvent B for 5 minutes at a 1.2mL/min flow rate. Solvent D (95:5 (v/v) Acetonitrile-water with 10mM Ammonium acetate) was infused post-column at 0.03ml/min. Column oven temperature was 25°C. Data was acquired in positive and negative ionization mode using multiple reaction monitoring (MRM). Each lipid class was normalized to its correspondent internal standard. The LC-MS data was analyzed using MultiQuant software (SCIEX). Abundance of lipids in each of the samples are normalized to cell number.

# CHAPTER SIX

# Discussion

## Significance

Neurological diseases are associated with numerous defects in cellular function including synaptic vesicle fusion, cargo trafficking, intracellular metabolite distribution, synaptic connections, cell cycle and cell junction function. Defects in any one of these molecular events can have a profound impact on organelle function and homeostasis. Some examples are - (1) ER morphology disruption either due to defects in ER shaping proteins or alterations in lipid metabolism or membrane fatty acyl chain properties, which affect both structure and membrane fluidity of the ER (Blackstone, O'Kane, and Reid 2011) (2) mitochondrial dysfunction resulting in ROS species production, improper lipid consumption and defects in energy production (3) failure in recycling of metabolites efficiently by lysosomes (4) defects in plasma membrane derived vesicle trafficking or (5) failure in signaling or cross-communication between the ER with other organelles – all of which can contribute to neurological diseases. **The aim of my research was to investigate the mechanism underlying one such recently recognized autosomal recessive neuronal disorder called SCAR20.** The characteristic symptoms of this disease include cerebellar ataxia, macrocephaly, reduced cerebellum volume, defective speech and motor skills. The SCAR20 patients suffer loss of Purkinje neurons and their fibroblasts exhibit increased vacuolation and lysosomes filled with electron dense cellular debris. The nature of existing ataxias are variable and hence their treatment depends largely on their underlying cause. SCAR20 is attributed to mutations in the protein coding region of Snx14 which belongs to sorting nexin family of proteins. Analysis of weighted gene coexpression network implicates Snx14 coexpresses with genes in vesicle transport and protein metabolism.

## Snx14 and SCAR20 disease

Initial studies on SCAR20 patient derived cells showed autophagosome accumulation under nutrient stress (Akizu et al. 2015). Similar phenotypic increases in autophagosomes were observed

in a zebrafish model where Snx14 was knocked down (Akizu et al. 2015). The mutations in Snx14 associated with SCAR20 either results in complete protein loss or include deletions in the phosphoinositide lipid binding PX domain (Akizu et al. 2015; Thomas et al. 2014). Consistent with this, Snx14 was detected as one of the candidates in a siRNA screen targeting PX domain containing proteins involved in autophagy regulation, although after careful dissection precise role of Snx14 in autophagy could not be validated (Holland et al. 2016; Knaevelsrud et al. 2013). Subsequently, a study by (Bryant et al. 2018) determined that Snx14 loss does not cause defects in autophagosome-lysosome fusion, rather shows enhanced autophagic response due to reasons still unknown. Such electron dense lysosome structures are also exhibited by NPC1 patient cells since NPC1 mediates cholesterol efflux from the lysosomes, suggesting Snx14 might also be involved in cholesterol transport pathway. However, cholesterol trafficking was intact in absence of Snx14 (Chu et al. 2015).

**Snx14 homolog in yeast - Mdm1**

Simultaneous investigation in yeast revealed that Snx14 homolog Mdm1 is an ER-lysosome tether (Henne et al. 2015). Under nutrient stress when metabolic remodeling occurs in yeast, LD biogenesis is upregulated and spatially LD budding is clustered at a ER-lysosome contact site also known as the NVJ (Hariri et al. 2018). The LD biogenesis sites at the NVJ are governed by Mdm1. Subsequent structure-function analysis of Mdm1 revealed that it localizes to tri-organelle junctions of the ER, LD and vacuole where Mdm1 interacts with FA-CoA ligase Faa1 to promote the esterification of FFAs, and thus promote LD production (Hariri et al. 2019). As a consequence, Mdm1 loss is associated with defects activating FFAs and causes FFA accumulation similar to deletion of Faa1. FFA accumulation can perturb ER function, which ultimately distorts ER morphology following treatment with exogenous FAs. Morphologically, Mdm1 is anchored to the nuclear surface (part of the ER) via its TM domain at its N terminus, and interacts with PI3P lipids enriched on vacuole membrane via its C-terminal PX domain. Mdm1 is architecturally conserved with Snx14, and since Snx14 loss is associated with defects in lysosome homeostasis, we dissected whether Snx14 was also an ER-lysosome tether similar to yeast Mdm1.

**Snx14 domain analysis**

Protein domain analysis of Snx14 by homology revealed that Snx14 contains, from the N-terminus, a transmembrane (TM) domain, a PXA domain, an RGS domain, a PX domain and a C-Nexin domain. Though the RGS and PX domains are well characterized from other studies, their functions in Snx14 appears to be non-canonical. For example, alignment data indicates that the RGS domain lacks residues required for G-protein signaling and extensive biochemical experiments confirm that it does not function as a traditional RGS domain (Mas et al. 2014)(also study by Brett Collins' group at Univ of Queensland). Surprisingly, both structural, biochemical and imaging studies on the Snx14 PX domain confirmed that it does not directly interact with phosphoinositide phospholipids; there are natural mutations in the canonical phosphoinositide binding pocket which attenuates PIP lipid binding (Mas et al. 2014). In line with this, intracellular cell biology experiments could not detect Snx14 enriched at ER-lysosome contacts, and expression of the Snx14 PX domain in yeast confirmed its localization to the cytoplasm, and not to PI3P containing organelles (Chandra et al. 2019). However, like Mdm1, I find that Snx14 does contribute to cellular lipid metabolism. Specifically, Snx14 loss affects neutral lipid metabolism (Bryant et al. 2018). Additionally, organelle fractionation and imaging analysis reveals that Snx14 is anchored at the primary lipid synthesizing organelle (the ER), but translocates and enriches at ER-LD interfaces when LD biogenesis is induced by oleate treatment. I discovered that topologically, Snx14 anchors at the ER membrane via its predicted double pass TM domain and interacts with the LD surface via an amphipathic helical region in its C-Nexin domain, thus maintaining ER-LD crosstalk and promoting proper LD maturation from the ER (Datta et al. 2019). In line with this, Snx14 overexpression expands ER-LD contact sites, and drives LD biogenesis whereas Snx14 loss perturbs oleate-induced LD morphology. Snx14 also features a PXA domain, which is still not very well characterized. Recent studies in yeast showed that the PXA domain in yeast is very hydrophobic and binds FAs *in vitro*. Indeed, my study (Chapter 4) of Snx14 showed that when the PXA domain is deleted from the full length protein, cells manifest FFA accumulation and hypersensitivity towards SFAs similar to *SNX14-KO* cells, indicating that PXA domain is required for FA homeostasis. Overall, my research indicates that Snx14 and its homologs are hydrophobic proteins that directly bind to LDs and behave as scaffolds to promote

FA processing and conversation into TAG for storage in LDs. It suggests a model where Snx14 functions in spatially compartmentalizing FA processing in the ER network to maintain ER and cell lipid homeostasis.

**Snx14 homolog in *Drosophila* – Snazarus (Snz)**

Snx14 functional conservation in lipid metabolism is reflected in its orthologs in other model systems such as zebrafish and *Drosophila,* which are useful models to study tissue specific lipid metabolism, and inter-tissue crosstalk or lipid trafficking. Additionally, Snx14 mutations in canines such as Hungarian Vizla dogs also manifested Purkinje neuron loss and delayed development and ataxia. Interestingly, when Snx14 was knocked down in zebrafish, autophagosomes accumulated and the cellular lipid profile was altered according to lipidomic assessment (Akizu et al. 2015; Bryant et al. 2020). In other studies, the Snx14 homolog in *Drosophila* called Snz was discovered as a fly longevity gene (Suh et al. 2008). Mechanistic analysis in the Henne lab further showed that Snz drives TAG synthesis and LD biogenesis in *Drosophila* adipose tissue, thus promoting starvation resistance and extending organismal lifespan by supporting nutrient storage as TG. Intriguingly, Snz localizes to ER-PM-LD triorganelle contacts in adipose cells. This is due to the non-canonical PX domain of Snz, which binds to PIP lipids such as PI(4,5)P2 at the PM, but not to PI3P at endosomes or lysosomes (Ugrankar et al. 2019). This unexpected polar localization of Snz at tri-organelle contacts of ER, PM and LDs led to the discovery of two LD sub-populations in fly adipose tissue – the median LDs regulated by FASN-mediated *de novo* lipogenesis and the peripheral small LDs potentially regulated by lipophorin-mediated extracellular lipid uptake. Fly Snz is a typical example suggesting how the SNX PX domain of the human Snx14 homologs functionally diverged as it bound to distinct PIP lipids, which are enriched on different cellular organelles. In this model, the PX domain essentially sets the sub-cellular region where the Snx14 homolog localizes: Snz PX domain interacts with PM membrane lipids such as PI4P and PI4,5P2 whereas Mdm1 PX domain binds PI3P lipids enriched on vacuole. During LD biogenesis Snx14 localizes to ER-LD contacts but appears not to bind to a third organelle.

**Conclusion**

Altogether from all the Snx14 homolog studies in different model systems, coupled with my studies on the mechanism of Snx14 function in mammalian tissue culture cells elaborated in Chapters 2,3, and 4, the following conclusions can be made –(1) Snx14, like yeast Mdm1 and fly Snz, has a function in lipid metabolism, driving TAG synthesis and LD formation (2) Similar to yeast Mdm1 which localizes at ER-lysosome-LD tri-organelle contacts and fly Snz localizing at ER-PM-LD contacts spatially regulating LD biogenesis, ER-resident Snx14 enriches at ER-LD contacts independent of another ER-LD tether Seipin, and promotes LD biogenesis under oleate treated conditions (3) APEX2 proximity-based labeling revealed that at ER-LD junctions, Snx14 associates with key lipid synthesizing and LD formation enzymes such as PLINs, DGAT2, FA elongases like ELOVL1, and FA desaturases like FADS1, FADS2, and SCD1  (4) *SNX14-KO* cells are hypersensitive to high dosages of SFAs and accumulate saturated fatty acyl chains in the phospholipids, but KO cells can be rescued by over-expressing the FA desaturase SCD1 (5) Snx14 functionally interacts with SCD1 and Snx14 loss mimics the altered lipid profile of reduced SCD1 activity, suggesting that both Snx14 and SCD1 collaborate on same lipid modifying pathway. (6) When treated with exogenous FAs, *SNX14-KO* cells exhibits accumulation of FFAs and progressively perturbed ER morphology which can be the major cause behind the enhanced lipotoxic cell death observed in *SNX14-KO* cells.

**Working model**

Based on all the evidence, my working model on how Snx14 is involved in maintaining lipid homeostasis and neuronal health is as follows – Snx14 family proteins spatially organize lipid metabolism by acting as ER scaffolds and recruiting key lipid synthesizing enzymes at specific FA-enriched processing sites at the ER membrane. Being a hydrophobic protein due to its TM and PXA domains, I propose that Snx14 potentially binds FAs directly at the ER and presents FFAs to key enzymes like SCD1 and fatty acyl-CoA ligases detected by APEX2-labeled Snx14, all of which is involved in synthesizing complex lipids. This is consistent with the altered lipid profile of *SNX14-KO* cells, which will consequently impact organelle homeostasis and ultimately

contribute to cell death. These lipid changes and perturbed organelle morphology in *SNX14-KO* are mostly observed under different stresses such as starvation or high dosages of exogenous FAs, suggesting that Snx14 functions in adaptive stress responses. In line with this, Snx14 appears to be a "metabolically controlled tether", localizing throughout the ER network under ambient conditions, but translocating to LDs following oleate addition to aid in the processing of oleate into TAG for LD storage.

Our results show that during OA-induced LD biogenesis, Snx14 maintains proper LD maturation from the ER and LD morphology. Although we propose in Chapter 3 that the tethering of LDs to ER by Snx14 might help in proper LD emergence from the ER and define the homogeneity in LD size, there can be other possibilities of how Snx14 determines LD size. In Chapter 4, APEX-labeling shows the enrichment of many lipid-metabolizing enzymes at ER-LD contacts, some of which can interact with Snx14 to mediate LD budding and determine LD size. Besides, *SNX14-KO* cells exhibit an altered lipid profile, which can also contribute to the change in FA composition at ER-LD contact and consequently result in perturbed LD budding and LD sizes that we observe upon Snx14 loss.

Snx14 endogenous expression is very low in all cells we have examined, and database mRNA datasets also indicate it is a low expression protein, suggesting that cells strategically express low levels of this protein to finely regulate lipid metabolism. Our model suggests that loss of Snx14 causes defects in the ability to spatially recruit and/or organize key lipid enzymes to their destined functioning sites in ER subdomains, which alters downstream lipid processing, and results in a changed cellular lipid profile. For example, when treated with exogenous SFAs like palmitate, *SNX14-KO* cells likely fail to efficiently present FAs to the desaturase SCD1 for further processing, which results in overall increase saturation in key lipid species that ultimately perturbs ER morphology and contributes to lipotoxic cell death. This mechanism can be a potential reason behind the Purkinje neuron loss that we observe in SCAR20 patients, but further research is of course needed. To study how lipid metabolism is affected in brains can be very challenging. Here, I utilized a biochemically and genetically enabling tissue culture system, as well as related studies

of Snx14 orthologs in yeast and flies, all of which have been very helpful in providing valuable insights regarding Snx14 function.

## Future directions

*Main question*

Lipid metabolism defects are major causes of neuropathogenesis. In response to exogenous FAs, I find that cells lacking Snx14 showed defective lipid homeostasis, which ultimately contributes to their cell death. When treated with oleate, cellular LD biogenesis in absence of Snx14 was perturbed. However, when treated with high dosage of palmitate, *SNX14-KO* cells became hypersensitive. The current model suggests that Snx14 enriches at FA processing ER subdomains and recruits key enzymes for FA and lipid processing, which ultimately support LD biogenesis. Interestingly, despite Snx14 expression being ubiquitous in all tissues examined, Snx14 loss in humans primarily affects neuronal functioning. Why Snx14 mutations impact neuronal health in particular will be important to dissect.

Although LD synthesis and LD budding factors such as FA synthases, DAG, and Seipin express in neurons, not much is known about LD biogenesis and its role in these cell types. Studies suggest that LD formation by the supporting cells, such as the glial cells, and the astrocytes can protect neurons from environmental stress such as inflammation or ROS generation during hyperactivity. Interestingly, electron microscope studies of frontal cortical neurons of patients with AD show dendrites containing LDs. NPC type-C patients also exhibit similar LD accumulation in the neurons as revealed by brain biopsies. Excess LD production is associated with neuronal loss in PD. Many such studies in different cell types in the brain underscore lipids and LD role in neuronal function (Farmer et al. 2020).

The function of Snx14 in LD production and maintaining lipid homeostasis in different cell types in brain and the CNS can explain the SCAR20 disease symptoms. Thus, the future steps will include generating a *SNX14-KO* mouse model to study the physiological relevance of Snx14

function. However, global *SNX14-KO* mice are embryonically lethal (Bryant et al. 2020) and so generating neuron-specific and astrocyte-specific *SNX14-KO* mice to determine if our studies in tissue culture recapitulates in a mouse model will be important.

*Next steps to study*

The following studies can be done to test if lipid metabolism is altered in the brain of a cell type-specific *SNX14-KO* mouse: – (1) To test our working model, all the tissue culture-based experiments on neuronal cells cultured from mice with Snx14 deleted neurons can be repeated. For example, using these neurons, we can determine its endogenous Snx14 localization, and whether Snx14 spatially organizes metabolism by localizing to ER subdomains and potentially to ER-LD contacts. We can also test if the lipidomic lipid profile is altered upon Snx14 deletion (2) We can test if neuron – astrocyte crosstalk is disrupted when Snx14 is deleted from either cell-type. Neurological disorders such as Alzheimer's disease has been shown to be associated with FA deposits in the brain. Thus, monitoring changes in LD biogenesis, mitochondrial FA oxidation, ROS species generation, and morphological alteration of the ER, mitochondria or lysosomes due to changes in membrane lipids in *SNX14-KO* neurons/astrocytes will provide insights behind SCAR20. (3) Lipidomics profiling from patient brain tissue, or using mouse model to determine if the lipid profile is altered in the neuron or the astrocytes will be useful. (4) In tissue culture cells, production of more MUFAs by SCD1 OE was able to rescue *SNX14-KO* mediated hypersensitivity in response to palmitate overdose. It will be next be interesting to test if SCD1 OE can reverse Purkinje neuronal loss or the altered lipid profile in mouse model, and this test will then ensure a very promising therapeutic strategy to combat this neurological disorder. The effect of modifying the mouse diet by introducing more MUFAs and less SFAs can also be an interesting approach to test rescue of *SNX14-KO* phenotype. (5) Further structural studies and in vitro biochemical studies are important to understand the molecular mechanism of the proposed model of how Snx14 spatially localizes and activates FAs for incorporation into complex lipids. (6) APEX2-based proteomics of Snx14 associated ER-LD contacts revealed a list of several lipid metabolism enzymes, which can be further investigated to dissect their functional relation with

Snx14 in maintaining lipid homeostasis. For example, SCD1 has been shown to affect FA elongation in adipocytes (Ralston et al. 2016), and we observe changes in FA chain length from our lipidomics data as well as presence of ELOVL1 in APEX2 proteomics. Additionally, according to (Man et al. 2006) SCD1 interacts with DGAT2 which implicates the possibility of substrate channeling for TAG synthesis. Indeed, in our Snx14 APEX2 proteomics we also found DGAT1 as a highly enriched candidate. Other than that, our APEX2 proteomics suggest the enrichment of many other fatty acid desaturases such as FADS1, FADS2 which act downstream of SCD1 and are involved in PUFA synthesis. Related to this, Seipin associated with ER-LD crosstalk independent of Snx14, and requires PUFAs for its enrichment at lipid enriched microdomains (Cao et al. 2019) (7) Determining the function of the other three mammalian Snx14 homologs, and whether function is redundant or related to Snx14 function, is important to understand the nature of the SCAR20 disease. In particular our biochemical data indicate that Snx14 and Snx13 may interact, suggesting their function in lipid metabolism can be redundant. Furthermore, among the Snx14 homologs only the Snx19 PX domain has strong affinity towards lysosome PI3P membrane lipids. Since we observe most structural change in lysosome of SCAR20 patients, studying Snx19 function will be beneficial. The Snx14 homolog Snx25 shares most homology with fly Snz, and hence determining whether it has any role in regulating a LD subpopulation in the cell periphery similar to *Drosophila* Snz will be interesting. Different organ and tissue types such as adipose tissue or hepatocytes have different LD morphology with specific LD proteome. Studying Snx25 function in these specific tissues can provide insight in not only understanding neurodisorders but also cardiovascular and associated metabolic disorders.

*Proposed model for Snx14 in autophagosomal accumulation*

How Snx14 loss causes increases in autophagic structures in patient fibroblasts is still not clear. Whether such electron dense lysosome-phagosome structures are direct or indirect consequences of Snx14 loss needs to be further dissected. One model is that since *SNX14-KO* cells have perturbed ER homeostasis, the ER may activate autophagosome biogenesis or even ER-phagy specifically, which upregulates autophagosome accumulation in cells. ER-phagy has been implicated in the cause of many neurodisorders. Moreover, if Snx14 functions in recruiting key

lipid synthesizing enzymes which cannot otherwise localize at their proper destinations, that can cause altered lipid profiles, whose incorporation into complex lipids and membrane structures may result in accumulation of lipid degenerative species in lysosome.

*In closing ...*

Overall, investigating how Snx14 spatially organizes lipid metabolism and how this impacts homeostasis on different levels of biological organization ranging from within cells to between tissues and organs, is important to understand Snx14's role in human health and disease. In line with this, generating mouse models with Snx14 deletion in different tissues to determine how these tissues contribute to metabolism will aid in the physiological dissection of Snx14 function. Additionally, dissecting the molecular mechanism by solving structures of parts of or the entire Snx14 protein will be beneficial to further understand the molecular basis for Snx14 function and its role in human health and disease, which may reveal further therapeutic strategies to treat SCAR20 disease.

# APPENDIX A

## Supplementary Table from Chapter Four

The following is a list of 60 proteins which are well characterized LD-associated proteins (Krahmer et al. 2013; Beller et al. 2006; Ding et al. 2012; Beller et al. 2008; Bersuker et al. 2018) and also detected in Snx14 associated ER-LD contact sites via our APEX2-proximity labeling technique.

**Supplementary Table 1.**

| Protein | purified with LDs in other studies | in Bersuker LD protenome | cyto-APEX/Sxn14-EA | ER-APEX/Snx14-EA | U2OS Snx14EA | HEK Snx14-EA |
|---|---|---|---|---|---|---|
| Calumenin | * | | n.d. | n.d. | 7.6913 | 7.0337 |
| Perilipin 3 | * | * | -9.0933 | -7.4033 | 6.2829 | 5.9208 |
| Snx14 | | | -12.4545 | -11.9901 | 6.0471 | 6.3133 |
| VCP | * | * | -8.3483 | -6.0737 | 5.7007 | 7.2535 |
| GAPDH | | * | -7.7946 | -6.6729 | 4.8516 | 5.1567 |
| OSBPL9 | * | | -7.3485 | -4.9163 | 4.1970 | 5.0402 |
| CYB5R3 | | * | -9.6087 | -6.9682 | 4.1540 | 3.8558 |
| Rab7a | * | * | -7.7042 | -4.7066 | 4.0670 | 4.9204 |
| Perilipin 2 | * | * | -10.8154 | -7.8164 | 3.9707 | 3.5895 |
| Diacyl kinase epsilon (DGKE) | | | n.d. | n.d. | 3.8330 | 4.3623 |
| VPS13C | * | * | -10.428 | -7.2189 | 3.7419 | 3.1956 |
| Rab10 | | * | n.d. | -6.2126 | 3.6243 | 4.2164 |
| PNPLA2 | * | * | n.d. | -6.6101 | 3.6095 | 4.0910 |
| LPCAT1 | | * | -6.09321 | -3.6509 | 3.4162 | 3.9146 |
| FDFT1 (squalene synthease) | | | n.d. | -6.4501 | 3.2477 | 5.1376 |
| Aup1 | | * | -7.7135 | -4.8960 | 3.1242 | 1.5762 |
| ACSL4 | * | * | -6.9389 | -4.8677 | 3.0581 | 4.7867 |
| OSBP10 | | | -8.6856 | -6.5618 | 3.0050 | 4.5446 |
| FADS1 | | | -9.2296 | -5.9529 | 2.9948 | 2.9758 |
| OSBPL3 | | | -7.8052 | -5.4713 | 2.9504 | 3.2710 |
| WFS1 | | | -9.1799 | -7.9721 | 2.9217 | 7.3380 |
| VPS13A | * | * | n.d. | -5.6081 | 2.8849 | 3.1616 |
| NSDHL | | * | -9.0047 | -5.9334 | 2.8429 | 2.5277 |
| Rab8a | * | | n.d. | n.d. | 2.8330 | 6.2584 |

| | | | | | | |
|---|---|---|---|---|---|---|
| PKMyt1 | | * | -9.6354 | -4.2807 | 2.7279 | 2.9877 |
| SOAT1 | | | -8.0467 | -9.7564 | 2.6581 | 3.4542 |
| SCD1 | * | | -8.5059 | -3.5433 | 2.6507 | 2.8995 |
| LPGAT1 | | | n.d. | n.d. | 2.5924 | 3.2808 |
| ACAT1 | | | -8.6770 | -5.8805 | 2.5775 | 2.7745 |
| FASN | | | -5.1447 | -3.3725 | 2.5669 | 2.8717 |
| Mgst3 | * | | n.d. | n.d. | 2.5604 | 4.4387 |
| Rab11b | * | * | -9.9137 | -4.9863 | 2.5531 | 5.3361 |
| Faf2 | | * | -7.6618 | -5.2244 | 2.5110 | 2.6048 |
| Atlastin-2 | * | | -9.3515 | -6.0257 | 2.4397 | 3.7082 |
| Atlastin-3 | * | | -10.2057 | -8.4803 | 2.4329 | 3.1935 |
| ELOVL1 | | | n.d. | -7.2442 | 2.4055 | 3.2845 |
| PITPNB | | * | n.d. | n.d. | 2.3719 | 3.3977 |
| SQLE | | * | -11.1974 | -9.3916 | 2.3495 | 4.7505 |
| OSBP1 | | | -4.9703 | -2.8911 | 2.3050 | 4.3712 |
| Rab1a | * | * | -6.6988 | -5.8984 | 2.2972 | 4.1672 |
| RDH14 | | | -4.9966 | -4.2293 | 2.2423 | 3.9371 |
| Cfl1 | | * | -7.0771 | -3.7561 | 2.1841 | 1.6133 |
| Vigilin | | | -6.2180 | -4.3742 | 2.1735 | 3.4976 |
| ACADVL | | | -12.0543 | -10.9619 | 2.1637 | 1.3879 |
| FADS2 | | | n.d. | -10.2466 | 2.1522 | 2.4318 |
| Rab5b | * | * | -8.5828 | -5.4895 | 2.0070 | 5.2201 |
| Rab14 | | * | -7.6181 | -5.6886 | 1.9710 | 3.4487 |
| APOOL | | * | n.d. | -6.4681 | 1.8913 | 3.2276 |
| TUBA1C | | * | -7.7134 | -6.2398 | 1.8774 | 2.8759 |
| Rab34 | | * | -10.2415 | -7.1737 | 1.8581 | 2.1458 |
| Rab5c | | * | -6.4977 | -3.8582 | 1.7916 | 4.1117 |
| LPCAT3 | * | | n.d. | -9.5025 | 1.7782 | 3.1873 |
| Rab21 | | * | n.d. | -5.8649 | 1.7513 | 4.5057 |
| Rab18 | | * | n.d. | -6.8534 | 1.7215 | 2.4933 |
| ELOVL5 | | | n.d. | n.d. | 1.6348 | 1.7113 |
| HSD17B11 | * | * | -8.0291 | -6.6520 | 1.5084 | 2.3537 |
| Rab13 | | * | -4.2415 | -3.3675 | 1.4673 | 2.5340 |
| Acox1 | | | n.d. | n.d. | 1.4245 | 4.2455 |
| SLC27A4 | | | -10.068 | -5.7508 | 1.3316 | 1.7282 |
| Rab5a | * | * | -7.361 | -4.3453 | 1.1473 | 2.3621 |

Importantly, this is a shortened list from a list of ~2000 proteins that were processed according to Figure 4.E to finalize our investigation on the interaction between Snx14 and desaturase SCD1.

# APPENDIX B

## Featured publications and Co-author contributions

1. Most of the data and figures in Chapter two was produced in collaboration with Dale Bryant from Phil Stanier's group in UCL, London, UK, which was published (Bryant et al. 2018)

2. Chapter three was reproduced in whole from my first author publication in Journal of Cell Biology (Datta et al. 2019)

3. Chapter four is my first author contribution which is accepted by *PNAS* and can currently be accessed in *BioArxiv* – Datta, S., J. Bowerman, H. Hariri, R. Ugrankar, K. M. Eckert, C. Corley, G. Vale, J. G. Mcdonald,W. M. Henne. 2019. 'Snx14 proximity labeling reveals a role in saturated fatty acid metabolism and ER homeostasis defective in SCAR20 disease' , *bioArxiv*, doi: https://doi.org/10.1101/2020.05.31.126441

# Bibliography

Adibhatla, R. M., and J. F. Hatcher. 2008. 'Altered lipid metabolism in brain injury and disorders', *Subcell Biochem*, 49: 241-68.

Akizu, N., V. Cantagrel, M. S. Zaki, L. Al-Gazali, X. Wang, R. O. Rosti, E. Dikoglu, A. B. Gelot, B. Rosti, K. K. Vaux, E. M. Scott, J. L. Silhavy, J. Schroth, B. Copeland, A. E. Schaffer, P. L. Gordts, J. D. Esko, M. D. Buschman, S. J. Field, G. Napolitano, G. M. Abdel-Salam, R. K. Ozgul, M. S. Sagiroglu, M. Azam, S. Ismail, M. Aglan, L. Selim, I. G. Mahmoud, S. Abdel-Hadi, A. E. Badawy, A. A. Sadek, F. Mojahedi, H. Kayserili, A. Masri, L. Bastaki, S. Temtamy, U. Muller, I. Desguerre, J. L. Casanova, A. Dursun, M. Gunel, S. B. Gabriel, P. de Lonlay, and J. G. Gleeson. 2015. 'Biallelic mutations in SNX14 cause a syndromic form of cerebellar atrophy and lysosome-autophagosome dysfunction', *Nat Genet*, 47: 528-34.

Antonsson, B. 1997. 'Phosphatidylinositol synthase from mammalian tissues', *Biochim Biophys Acta*, 1348: 179-86.

Ariyama, H., N. Kono, S. Matsuda, T. Inoue, and H. Arai. 2010. 'Decrease in membrane phospholipid unsaturation induces unfolded protein response', *J Biol Chem*, 285: 22027-35.

Athenstaedt, K., and G. Daum. 2006. 'The life cycle of neutral lipids: synthesis, storage and degradation', *Cell Mol Life Sci*, 63: 1355-69.

Barbosa, A. D., H. Sembongi, W. M. Su, S. Abreu, F. Reggiori, G. M. Carman, and S. Siniossoglou. 2015. 'Lipid partitioning at the nuclear envelope controls membrane biogenesis', *Mol Biol Cell*, 26: 3641-57.

Baumann, N. A., D. P. Sullivan, H. Ohvo-Rekila, C. Simonot, A. Pottekat, Z. Klaassen, C. T. Beh, and A. K. Menon. 2005. 'Transport of newly synthesized sterol to the sterol-enriched plasma membrane occurs via nonvesicular equilibration', *Biochemistry*, 44: 5816-26.

Bell, R. M., and R. A. Coleman. 1980. 'Enzymes of glycerolipid synthesis in eukaryotes', *Annu Rev Biochem*, 49: 459-87.

Beller, M., D. Riedel, L. Jansch, G. Dieterich, J. Wehland, H. Jackle, and R. P. Kuhnlein. 2006. 'Characterization of the *Drosophila* lipid droplet subproteome', *Mol Cell Proteomics*, 5: 1082-94.

Beller, M., C. Sztalryd, N. Southall, M. Bell, H. Jackle, D. S. Auld, and B. Oliver. 2008. 'COPI complex is a regulator of lipid homeostasis', *PLoS Biol*, 6: e292.

Bersuker, K., C. W. H. Peterson, M. To, S. J. Sahl, V. Savikhin, E. A. Grossman, D. K. Nomura, and J. A. Olzmann. 2018. 'A Proximity Labeling Strategy Provides Insights into the Composition and Dynamics of Lipid Droplet Proteomes', *Dev Cell*, 44: 97-112 e7.

Blackstone, C., C. J. O'Kane, and E. Reid. 2011. 'Hereditary spastic paraplegias: membrane traffic and the motor pathway', *Nat Rev Neurosci*, 12: 31-42.

Blight, E. G., and W. J. Dyer. 1959. 'A rapid method of total lipid extraction and purification', *Canadian Journal of Biochemistry and Physiology*, 37: 911-17.

Bloch, K. 1965. 'The biological synthesis of cholesterol', *Science*, 150: 19-28.

Blom, T., P. Somerharju, and E. Ikonen. 2011. 'Synthesis and biosynthetic trafficking of membrane lipids', *Cold Spring Harb Perspect Biol*, 3: a004713.

Bohnert, M. 2020. 'Tether Me, Tether Me Not-Dynamic Organelle Contact Sites in Metabolic Rewiring', *Dev Cell*, 54: 212-25.

Borradaile, N. M., X. Han, J. D. Harp, S. E. Gale, D. S. Ory, and J. E. Schaffer. 2006a. 'Disruption of endoplasmic reticulum structure and integrity in lipotoxic cell death', *J Lipid Res*, 47: 2726-37.

Borradaile, N. M., X. L. Han, J. D. Harp, S. E. Gale, D. S. Ory, and J. E. Schaffer. 2006b. 'Disruption of endoplasmic reticulum structure and integrity in lipotoxic cell death', *Journal of Lipid Research*, 47: 2726-37.

Borradaile, N. M., J. D. Harp, and J. E. Schaffer. 2006. 'Palmitate-induced changes in endoplasmic reticulum structure and function: A central role for the ER in lipotoxicity', *Arteriosclerosis Thrombosis and Vascular Biology*, 26: E49-E49.

Borradaile, N. M., and J. E. Schaffer. 2005. 'Lipotoxicity in the heart', *Curr Hypertens Rep*, 7: 412-7.

Bouchard, L., G. Faucher, A. Tchernof, Y. Deshaies, S. Marceau, O. Lescelleur, S. Biron, C. Bouchard, L. Perusse, and M. C. Vohl. 2009. 'Association of OSBPL11 gene polymorphisms with cardiovascular disease risk factors in obesity', *Obesity (Silver Spring)*, 17: 1466-72.

Brown, D. A. 2001. 'Lipid droplets: proteins floating on a pool of fat', *Curr Biol*, 11: R446-9.

Brown, M. S., and J. L. Goldstein. 1986. 'A receptor-mediated pathway for cholesterol homeostasis', *Science*, 232: 34-47.

———. 2009. 'Cholesterol feedback: from Schoenheimer's bottle to Scap's MELADL', *J Lipid Res*, 50 Suppl: S15-27.

Bruce, K. D., A. Zsombok, and R. H. Eckel. 2017. 'Lipid Processing in the Brain: A Key Regulator of Systemic Metabolism', *Front Endocrinol (Lausanne)*, 8: 60.

Bryant, D., Y. Liu, S. Datta, H. Hariri, M. Seda, G. Anderson, E. Peskett, C. Demetriou, S. Sousa, D. Jenkins, P. Clayton, M. Bitner-Glindzicz, G. E. Moore, W. M. Henne, and P. Stanier. 2018. 'SNX14 mutations affect endoplasmic reticulum-associated neutral lipid metabolism in autosomal recessive spinocerebellar ataxia 20', *Hum Mol Genet*, 27: 1927-40.

Bryant, D., M. Seda, E. Peskett, C. Maurer, G. Pomeranz, M. Ghosh, T. A. Hawkins, J. Cleak, S. Datta, H. Hariri, K. M. Eckert, D. J. Jafree, C. Walsh, C. Demetriou, M. Ishida, C. Aleman-Charlet, L. Vestito, R. Seselgyte, J. G. McDonald, M. Bitner-Glindzicz, M. Hemberger, J. Rihel, L. Teboul, W. M. Henne, D. Jenkins, G. E. Moore, and P. Stanier. 2020. 'Diverse species-specific phenotypic consequences of loss of function sorting nexin 14 mutations', *Sci Rep*, 10: 13763.

Cao, Z., Y. Hao, C. W. Fung, Y. Y. Lee, P. Wang, X. Li, K. Xie, W. J. Lam, Y. Qiu, B. Z. Tang, G. Shui, P. Liu, J. Qu, B. H. Kang, and H. Y. Mak. 2019. 'Dietary fatty acids promote lipid droplet diversity through seipin enrichment in an ER subdomain', *Nat Commun*, 10: 2902.

Cartwright, B. R., D. D. Binns, C. L. Hilton, S. Han, Q. Gao, and J. M. Goodman. 2015. 'Seipin performs dissectible functions in promoting lipid droplet biogenesis and regulating droplet morphology', *Mol Biol Cell*, 26: 726-39.

Chandra, M., Y. K. Chin, C. Mas, J. R. Feathers, B. Paul, S. Datta, K. E. Chen, X. Jia, Z. Yang, S. J. Norwood, B. Mohanty, A. Bugarcic, R. D. Teasdale, W. M. Henne, M. Mobli, and B. M. Collins. 2019. 'Classification of the human phox homology (PX) domains based on their phosphoinositide binding specificities', *Nat Commun*, 10: 1528.

Chang, T. Y., B. L. Li, C. C. Chang, and Y. Urano. 2009. 'Acyl-coenzyme A:cholesterol acyltransferases', *Am J Physiol Endocrinol Metab*, 297: E1-9.

Chirala, S. S., A. Jayakumar, Z. W. Gu, and S. J. Wakil. 2001. 'Human fatty acid synthase: role of interdomain in the formation of catalytically active synthase dimer', *Proc Natl Acad Sci U S A*, 98: 3104-8.

Chu, B. B., Y. C. Liao, W. Qi, C. Xie, X. Du, J. Wang, H. Yang, H. H. Miao, B. L. Li, and B. L. Song. 2015. 'Cholesterol transport through lysosome-peroxisome membrane contacts', *Cell*, 161: 291-306.

Chung, J., F. Torta, K. Masai, L. Lucast, H. Czapla, L. B. Tanner, P. Narayanaswamy, M. R. Wenk, F. Nakatsu, and P. De Camilli. 2015. 'INTRACELLULAR TRANSPORT. PI4P/phosphatidylserine countertransport at ORP5- and ORP8-mediated ER-plasma membrane contacts', *Science*, 349: 428-32.

Coleman, R. A., and D. P. Lee. 2004. 'Enzymes of triacylglycerol synthesis and their regulation', *Prog Lipid Res*, 43: 134-76.

D'Angelo, G., T. Uemura, C. C. Chuang, E. Polishchuk, M. Santoro, H. Ohvo-Rekila, T. Sato, G. Di Tullio, A. Varriale, S. D'Auria, T. Daniele, F. Capuani, L. Johannes, P. Mattjus, M. Monti, P. Pucci, R. L. Williams, J. E. Burke, F. M. Platt, A. Harada, and M. A. De Matteis. 2013. 'Vesicular and non-vesicular transport feed distinct glycosylation pathways in the Golgi', *Nature*, 501: 116-20.

Datta, S., Y. Liu, H. Hariri, J. Bowerman, and W. M. Henne. 2019. 'Cerebellar ataxia disease-associated Snx14 promotes lipid droplet growth at ER-droplet contacts', *J Cell Biol*, 218: 1335-51.

Ding, Y., Y. Wu, R. Zeng, and K. Liao. 2012. 'Proteomic profiling of lipid droplet-associated proteins in primary adipocytes of normal and obese mouse', *Acta Biochim Biophys Sin (Shanghai)*, 44: 394-406.

Ding, Y., S. Zhang, L. Yang, H. Na, P. Zhang, H. Zhang, Y. Wang, Y. Chen, J. Yu, C. Huo, S. Xu, M. Garaiova, Y. Cong, and P. Liu. 2013. 'Isolating lipid droplets from multiple species', *Nat Protoc*, 8: 43-51.

Du, X., L. Zhou, Y. C. Aw, H. Y. Mak, Y. Xu, J. Rae, W. Wang, A. Zadoorian, S. E. Hancock, B. Osborne, X. Chen, J. W. Wu, N. Turner, R. G. Parton, P. Li, and H. Yang. 2020. 'ORP5 localizes to ER-lipid droplet contacts and regulates the level of PI(4)P on lipid droplets', *J Cell Biol*, 219.

Elbaz, Y., and M. Schuldiner. 2011. 'Staying in touch: the molecular era of organelle contact sites', *Trends Biochem Sci*, 36: 616-23.

Elbaz-Alon, Y., M. Eisenberg-Bord, V. Shinder, S. B. Stiller, E. Shimoni, N. Wiedemann, T. Geiger, and M. Schuldiner. 2015. 'Lam6 Regulates the Extent of Contacts between Organelles', *Cell Rep*, 12: 7-14.

Ellingson, J. S., E. E. Hill, and W. E. Lands. 1970. 'The control of fatty acid composition in glycerolipids of the endoplasmic reticulum', *Biochim Biophys Acta*, 196: 176-92.

Ertunc, M. E., and G. S. Hotamisligil. 2016. 'Lipid signaling and lipotoxicity in metaflammation: indications for metabolic disease pathogenesis and treatment', *J Lipid Res*, 57: 2099-114.

Estadella, D., C. M. da Penha Oller do Nascimento, L. M. Oyama, E. B. Ribeiro, A. R. Damaso, and A. de Piano. 2013. 'Lipotoxicity: effects of dietary saturated and transfatty acids', *Mediators Inflamm*, 2013: 137579.

Farmer, B. C., A. E. Walsh, J. C. Kluemper, and L. A. Johnson. 2020. 'Lipid Droplets in Neurodegenerative Disorders', *Front Neurosci*, 14: 742.

Fei, W., G. Shui, B. Gaeta, X. Du, L. Kuerschner, P. Li, A. J. Brown, M. R. Wenk, R. G. Parton, and H. Yang. 2008. 'Fld1p, a functional homologue of human seipin, regulates the size of lipid droplets in yeast', *J Cell Biol*, 180: 473-82.

Fenn, J., M. Boursnell, R. J. Hitti, C. A. Jenkins, R. L. Terry, S. L. Priestnall, P. J. Kenny, C. S. Mellersh, and O. P. Forman. 2016. 'Genome sequencing reveals a splice donor site mutation in the SNX14 gene associated with a novel cerebellar cortical degeneration in the Hungarian Vizsla dog breed', *BMC Genet*, 17: 123.

Feoktistova, M., P. Geserick, and M. Leverkus. 2016. 'Crystal Violet Assay for Determining Viability of Cultured Cells', *Cold Spring Harb Protoc*, 2016: pdb prot087379.

Friedman, J. R., J. R. Dibenedetto, M. West, A. A. Rowland, and G. K. Voeltz. 2013. 'Endoplasmic reticulum-endosome contact increases as endosomes traffic and mature', *Mol Biol Cell*, 24: 1030-40.

Fu, S., S. M. Watkins, and G. S. Hotamisligil. 2012. 'The role of endoplasmic reticulum in hepatic lipid homeostasis and stress signaling', *Cell Metab*, 15: 623-34.

Fu, S., L. Yang, P. Li, O. Hofmann, L. Dicker, W. Hide, X. Lin, S. M. Watkins, A. R. Ivanov, and G. S. Hotamisligil. 2011. 'Aberrant lipid metabolism disrupts calcium homeostasis causing liver endoplasmic reticulum stress in obesity', *Nature*, 473: 528-31.

Fujimoto, T., and R. G. Parton. 2011. 'Not just fat: the structure and function of the lipid droplet', *Cold Spring Harb Perspect Biol*, 3.

Gallegos, A. M., B. P. Atshaves, S. M. Storey, A. L. McIntosh, A. D. Petrescu, and F. Schroeder. 2001. 'Sterol carrier protein-2 expression alters plasma membrane lipid distribution and cholesterol dynamics', *Biochemistry*, 40: 6493-506.

Galmes, R., A. Houcine, A. R. van Vliet, P. Agostinis, C. L. Jackson, and F. Giordano. 2016. 'ORP5/ORP8 localize to endoplasmic reticulum-mitochondria contacts and are involved in mitochondrial function', *EMBO Rep*, 17: 800-10.

Gao, D., S. Nong, X. Huang, Y. Lu, H. Zhao, Y. Lin, Y. Man, S. Wang, J. Yang, and J. Li. 2010. 'The effects of palmitate on hepatic insulin resistance are mediated by NADPH Oxidase 3-derived reactive oxygen species through JNK and p38MAPK pathways', *J Biol Chem*, 285: 29965-73.

Gao, Q., D. D. Binns, L. N. Kinch, N. V. Grishin, N. Ortiz, X. Chen, and J. M. Goodman. 2017. 'Pet10p is a yeast perilipin that stabilizes lipid droplets and promotes their assembly', *J Cell Biol*, 216: 3199-217.

Gatta, A. T., L. H. Wong, Y. Y. Sere, D. M. Calderon-Norena, S. Cockcroft, A. K. Menon, and T. P. Levine. 2015. 'A new family of StART domain proteins at membrane contact sites has a role in ER-PM sterol transport', *Elife*, 4.

Giordano, F., Y. Saheki, O. Idevall-Hagren, S. F. Colombo, M. Pirruccello, I. Milosevic, E. O. Gracheva, S. N. Bagriantsev, N. Borgese, and P. De Camilli. 2013. 'PI(4,5)P(2)-dependent and Ca(2+)-regulated ER-PM interactions mediated by the extended synaptotagmins', *Cell*, 153: 1494-509.

Glaser, C., J. Heinrich, and B. Koletzko. 2010. 'Role of FADS1 and FADS2 polymorphisms in polyunsaturated fatty acid metabolism', *Metabolism*, 59: 993-9.

Guillou, H., D. Zadravec, P. G. Martin, and A. Jacobsson. 2010. 'The key roles of elongases and desaturases in mammalian fatty acid metabolism: Insights from transgenic mice', *Prog Lipid Res*, 49: 186-99.

Guo, Y., K. R. Cordes, R. V. Farese, Jr., and T. C. Walther. 2009. 'Lipid droplets at a glance', *J Cell Sci*, 122: 749-52.

Ha, C. M., D. Park, Y. Kim, M. Na, S. Panda, S. Won, H. Kim, H. Ryu, Z. Y. Park, M. M. Rasenick, and S. Chang. 2015. 'SNX14 is a bifunctional negative regulator for neuronal 5-HT6 receptor signaling', *J Cell Sci*, 128: 1848-61.

Haffar, T., F. Berube-Simard, and N. Bousette. 2015. 'Impaired fatty acid oxidation as a cause for lipotoxicity in cardiomyocytes', *Biochem Biophys Res Commun*, 468: 73-8.

Hanada, K., K. Kumagai, S. Yasuda, Y. Miura, M. Kawano, M. Fukasawa, and M. Nishijima. 2003. 'Molecular machinery for non-vesicular trafficking of ceramide', *Nature*, 426: 803-9.

Hariri, H., S. Rogers, R. Ugrankar, Y. L. Liu, J. R. Feathers, and W. M. Henne. 2018. 'Lipid droplet biogenesis is spatially coordinated at ER-vacuole contacts under nutritional stress', *EMBO Rep*, 19: 57-72.

Hariri, H., N. Speer, J. Bowerman, S. Rogers, G. Fu, E. Reetz, S. Datta, J. R. Feathers, R. Ugrankar, D. Nicastro, and W. M. Henne. 2019. 'Mdm1 maintains endoplasmic reticulum homeostasis by spatially regulating lipid droplet biogenesis', *J Cell Biol*, 218: 1319-34.

Hariri, H., R. Ugrankar, Y. Liu, and W. M. Henne. 2016. 'Inter-organelle ER-endolysosomal contact sites in metabolism and disease across evolution', *Commun Integr Biol*, 9: e1156278.

Hashimoto, Y., M. Shirane, F. Matsuzaki, S. Saita, T. Ohnishi, and K. I. Nakayama. 2014. 'Protrudin regulates endoplasmic reticulum morphology and function associated with the pathogenesis of hereditary spastic paraplegia', *J Biol Chem*, 289: 12946-61.

Hayashi, H. 2011. '[Lipid metabolism in the central nervous system and neurodegenerative diseases]', *Nihon Yakurigaku Zasshi*, 137: 227-31.

Helmkamp, G. M., Jr., M. S. Harvey, K. W. Wirtz, and L. L. Van Deenen. 1974. 'Phospholipid exchange between membranes. Purification of bovine brain proteins that preferentially catalyze the transfer of phosphatidylinositol', *J Biol Chem*, 249: 6382-9.

Henne, W. M., M. L. Reese, and J. M. Goodman. 2019. 'The assembly of lipid droplets and their roles in challenged cells', *EMBO J*, 38.

Henne, W. M., L. Zhu, Z. Balogi, C. Stefan, J. A. Pleiss, and S. D. Emr. 2015. 'Mdm1/Snx13 is a novel ER-endolysosomal interorganelle tethering protein', *J Cell Biol*, 210: 541-51.

Hetherington, A. M., C. G. Sawyez, E. Zilberman, A. M. Stoianov, D. L. Robson, and N. M. Borradaile. 2016. 'Differential Lipotoxic Effects of Palmitate and Oleate in Activated

Human Hepatic Stellate Cells and Epithelial Hepatoma Cells', *Cell Physiol Biochem*, 39: 1648-62.

Holland, P., H. Knaevelsrud, K. Soreng, B. J. Mathai, A. H. Lystad, S. Pankiv, G. T. Bjorndal, S. W. Schultz, V. H. Lobert, R. B. Chan, B. Zhou, K. Liestol, S. R. Carlsson, T. J. Melia, G. Di Paolo, and A. Simonsen. 2016. 'HS1BP3 negatively regulates autophagy by modulation of phosphatidic acid levels', *Nat Commun*, 7: 13889.

Hu, F. B., R. M. van Dam, and S. Liu. 2001. 'Diet and risk of Type II diabetes: the role of types of fat and carbohydrate', *Diabetologia*, 44: 805-17.

Hung, V., N. D. Udeshi, S. S. Lam, K. H. Loh, K. J. Cox, K. Pedram, S. A. Carr, and A. Y. Ting. 2016. 'Spatially resolved proteomic mapping in living cells with the engineered peroxidase APEX2', *Nat Protoc*, 11: 456-75.

Ioannou, M. S., J. Jackson, S. H. Sheu, C. L. Chang, A. V. Weigel, H. Liu, H. A. Pasolli, C. S. Xu, S. Pang, D. Matthies, H. F. Hess, J. Lippincott-Schwartz, and Z. Liu. 2019. 'Neuron-Astrocyte Metabolic Coupling Protects against Activity-Induced Fatty Acid Toxicity', *Cell*, 177: 1522-35 e14.

Jackson, R. L., J. D. Morrisett, and A. M. Gotto, Jr. 1976. 'Lipoprotein structure and metabolism', *Physiol Rev*, 56: 259-316.

Jarc, E., and T. Petan. 2019. 'Lipid Droplets and the Management of Cellular Stress', *Yale J Biol Med*, 92: 435-52.

Jump, D. B. 2009. 'Mammalian fatty acid elongases', *Methods Mol Biol*, 579: 375-89.

Kanno, K., M. K. Wu, E. F. Scapa, S. L. Roderick, and D. E. Cohen. 2007. 'Structure and function of phosphatidylcholine transfer protein (PC-TP)/StarD2', *Biochim Biophys Acta*, 1771: 654-62.

Kassan, A., A. Herms, A. Fernandez-Vidal, M. Bosch, N. L. Schieber, B. J. Reddy, A. Fajardo, M. Gelabert-Baldrich, F. Tebar, C. Enrich, S. P. Gross, R. G. Parton, and A. Pol. 2013. 'Acyl-CoA synthetase 3 promotes lipid droplet biogenesis in ER microdomains', *J Cell Biol*, 203: 985-1001.

Kawasaki, K., O. Kuge, S. C. Chang, P. N. Heacock, M. Rho, K. Suzuki, M. Nishijima, and W. Dowhan. 1999. 'Isolation of a chinese hamster ovary (CHO) cDNA encoding phosphatidylglycerophosphate (PGP) synthase, expression of which corrects the mitochondrial abnormalities of a PGP synthase-defective mutant of CHO-K1 cells', *J Biol Chem*, 274: 1828-34.

Kawasaki, K., and M. Nishijima. 2003. 'Purification of phosphatidylglycerophosphate synthase from cultured mammalian cells', *Methods Mol Biol*, 228: 175-86.

Kennedy, E. P., and S. B. Weiss. 1956. 'The function of cytidine coenzymes in the biosynthesis of phospholipids', *J Biol Chem*, 222: 193-214.

Kim, Y. J., M. L. Guzman-Hernandez, and T. Balla. 2011. 'A highly dynamic ER-derived phosphatidylinositol-synthesizing organelle supplies phosphoinositides to cellular membranes', *Dev Cell*, 21: 813-24.

Knaevelsrud, H., K. Soreng, C. Raiborg, K. Haberg, F. Rasmuson, A. Brech, K. Liestol, T. E. Rusten, H. Stenmark, T. P. Neufeld, S. R. Carlsson, and A. Simonsen. 2013. 'Membrane remodeling by the PX-BAR protein SNX18 promotes autophagosome formation', *J Cell Biol*, 202: 331-49.

Kohlwein, S. D., S. Eder, C. S. Oh, C. E. Martin, K. Gable, D. Bacikova, and T. Dunn. 2001. 'Tsc13p is required for fatty acid elongation and localizes to a novel structure at the nuclear-vacuolar interface in Saccharomyces cerevisiae', *Mol Cell Biol*, 21: 109-25.

Kondo, I., A. Shimizu, S. Asakawa, K. Miyamoto, H. Yamagata, Y. Tabara, and N. Shimizu. 2005. 'COH1 analysis and linkage study in two Japanese families with Cohen syndrome', *Clin Genet*, 67: 270-2.

Krahmer, N., Y. Guo, F. Wilfling, M. Hilger, S. Lingrell, K. Heger, H. W. Newman, M. Schmidt-Supprian, D. E. Vance, M. Mann, R. V. Farese, Jr., and T. C. Walther. 2011. 'Phosphatidylcholine synthesis for lipid droplet expansion is mediated by localized activation of CTP:phosphocholine cytidylyltransferase', *Cell Metab*, 14: 504-15.

Krahmer, N., M. Hilger, N. Kory, F. Wilfling, G. Stoehr, M. Mann, R. V. Farese, Jr., and T. C. Walther. 2013. 'Protein correlation profiles identify lipid droplet proteins with high confidence', *Mol Cell Proteomics*, 12: 1115-26.

Kuge, O., M. Nishijima, and Y. Akamatsu. 1986. 'Phosphatidylserine biosynthesis in cultured Chinese hamster ovary cells. III. Genetic evidence for utilization of phosphatidylcholine and phosphatidylethanolamine as precursors', *J Biol Chem*, 261: 5795-8.

Kumar, N., M. Leonzino, W. Hancock-Cerutti, F. A. Horenkamp, P. Li, J. A. Lees, H. Wheeler, K. M. Reinisch, and P. De Camilli. 2018. 'VPS13A and VPS13C are lipid transport proteins differentially localized at ER contact sites', *J Cell Biol*, 217: 3625-39.

Kusminski, C. M., S. Shetty, L. Orci, R. H. Unger, and P. E. Scherer. 2009. 'Diabetes and apoptosis: lipotoxicity', *Apoptosis*, 14: 1484-95.

Lam, S. S., J. D. Martell, K. J. Kamer, T. J. Deerinck, M. H. Ellisman, V. K. Mootha, and A. Y. Ting. 2015. 'Directed evolution of APEX2 for electron microscopy and proximity labeling', *Nat Methods*, 12: 51-4.

Lang, A. B., A. T. John Peter, P. Walter, and B. Kornmann. 2015. 'ER-mitochondrial junctions can be bypassed by dominant mutations in the endosomal protein Vps13', *J Cell Biol*, 210: 883-90.

Langdon, R. G., and K. Bloch. 1953. 'The utilization of squalene in the biosynthesis of cholesterol', *J Biol Chem*, 200: 135-44.

Lee, J. N., H. Kim, H. Yao, Y. Chen, K. Weng, and J. Ye. 2010. 'Identification of Ubxd8 protein as a sensor for unsaturated fatty acids and regulator of triglyceride synthesis', *Proc Natl Acad Sci U S A*, 107: 21424-9.

Lehner, R., and A. Kuksis. 1996. 'Biosynthesis of triacylglycerols', *Prog Lipid Res*, 35: 169-201.

Lelliott, C., and A. J. Vidal-Puig. 2004. 'Lipotoxicity, an imbalance between lipogenesis de novo and fatty acid oxidation', *Int J Obes Relat Metab Disord*, 28 Suppl 4: S22-8.

Lesage, S., V. Drouet, E. Majounie, V. Deramecourt, M. Jacoupy, A. Nicolas, F. Cormier-Dequaire, S. M. Hassoun, C. Pujol, S. Ciura, Z. Erpapazoglou, T. Usenko, C. A. Maurage, M. Sahbatou, S. Liebau, J. Ding, B. Bilgic, M. Emre, N. Erginel-Unaltuna, G. Guven, F. Tison, C. Tranchant, M. Vidailhet, J. C. Corvol, P. Krack, A. L. Leutenegger, M. A. Nalls, D. G. Hernandez, P. Heutink, J. R. Gibbs, J. Hardy, N. W. Wood, T. Gasser, A. Durr, J. F. Deleuze, M. Tazir, A. Destee, E. Lohmann, E. Kabashi, A. Singleton, O. Corti, A. Brice, Study French Parkinson's Disease Genetics, and Consortium International Parkinson's Disease Genomics. 2016. 'Loss of VPS13C Function in

Autosomal-Recessive Parkinsonism Causes Mitochondrial Dysfunction and Increases PINK1/Parkin-Dependent Mitophagy', *Am J Hum Genet*, 98: 500-13.

Lev, S., D. Ben Halevy, D. Peretti, and N. Dahan. 2008. 'The VAP protein family: from cellular functions to motor neuron disease', *Trends Cell Biol*, 18: 282-90.

Levine, T., and C. Loewen. 2006. 'Inter-organelle membrane contact sites: through a glass, darkly', *Curr Opin Cell Biol*, 18: 371-8.

Levine, T. P., and S. Munro. 2001. 'Dual targeting of Osh1p, a yeast homologue of oxysterol-binding protein, to both the Golgi and the nucleus-vacuole junction', *Mol Biol Cell*, 12: 1633-44.

Liesa, M., and O. S. Shirihai. 2013. 'Mitochondrial dynamics in the regulation of nutrient utilization and energy expenditure', *Cell Metab*, 17: 491-506.

Liou, J., M. Fivaz, T. Inoue, and T. Meyer. 2007. 'Live-cell imaging reveals sequential oligomerization and local plasma membrane targeting of stromal interaction molecule 1 after Ca2+ store depletion', *Proc Natl Acad Sci U S A*, 104: 9301-6.

Listenberger, L. L., X. Han, S. E. Lewis, S. Cases, R. V. Farese, Jr., D. S. Ory, and J. E. Schaffer. 2003. 'Triglyceride accumulation protects against fatty acid-induced lipotoxicity', *Proc Natl Acad Sci U S A*, 100: 3077-82.

Liu, L. K., V. Choudhary, A. Toulmay, and W. A. Prinz. 2017. 'An inducible ER-Golgi tether facilitates ceramide transport to alleviate lipotoxicity', *J Cell Biol*, 216: 131-47.

Man, W. C., M. Miyazaki, K. Chu, and J. Ntambi. 2006. 'Colocalization of SCD1 and DGAT2: implying preference for endogenous monounsaturated fatty acids in triglyceride synthesis', *J Lipid Res*, 47: 1928-39.

Martell, J. D., T. J. Deerinck, Y. Sancak, T. L. Poulos, V. K. Mootha, G. E. Sosinsky, M. H. Ellisman, and A. Y. Ting. 2012. 'Engineered ascorbate peroxidase as a genetically encoded reporter for electron microscopy', *Nat Biotechnol*, 30: 1143-8.

Mas, C., S. J. Norwood, A. Bugarcic, G. Kinna, N. Leneva, O. Kovtun, R. Ghai, L. E. Ona Yanez, J. L. Davis, R. D. Teasdale, and B. M. Collins. 2014. 'Structural basis for different phosphoinositide specificities of the PX domains of sorting nexins regulating G-protein signaling', *J Biol Chem*, 289: 28554-68.

McFie, P. J., and S. J. Stone. 2011. 'A fluorescent assay to quantitatively measure in vitro acyl CoA:diacylglycerol acyltransferase activity', *J Lipid Res*, 52: 1760-4.

Mitchell, R. W., and G. M. Hatch. 2011. 'Fatty acid transport into the brain: of fatty acid fables and lipid tails', *Prostaglandins Leukot Essent Fatty Acids*, 85: 293-302.

Miyazaki, M., Y. C. Kim, M. P. Gray-Keller, A. D. Attie, and J. M. Ntambi. 2000. 'The biosynthesis of hepatic cholesterol esters and triglycerides is impaired in mice with a disruption of the gene for stearoyl-CoA desaturase 1', *J Biol Chem*, 275: 30132-8.

Miyazaki, M., Y. C. Kim, and J. M. Ntambi. 2001. 'A lipogenic diet in mice with a disruption of the stearoyl-CoA desaturase 1 gene reveals a stringent requirement of endogenous monounsaturated fatty acids for triglyceride synthesis', *J Lipid Res*, 42: 1018-24.

Murley, A., R. D. Sarsam, A. Toulmay, J. Yamada, W. A. Prinz, and J. Nunnari. 2015. 'Ltc1 is an ER-localized sterol transporter and a component of ER-mitochondria and ER-vacuole contacts', *J Cell Biol*, 209: 539-48.

Ngo, M., and N. D. Ridgway. 2009. 'Oxysterol binding protein-related Protein 9 (ORP9) is a cholesterol transfer protein that regulates Golgi structure and function', *Mol Biol Cell*, 20: 1388-99.

Olzmann, J. A., and P. Carvalho. 2019. 'Dynamics and functions of lipid droplets', *Nat Rev Mol Cell Biol*, 20: 137-55.

Pagac, M., D. E. Cooper, Y. Qi, I. E. Lukmantara, H. Y. Mak, Z. Wu, Y. Tian, Z. Liu, M. Lei, X. Du, C. Ferguson, D. Kotevski, P. Sadowski, W. Chen, S. Boroda, T. E. Harris, G. Liu, R. G. Parton, X. Huang, R. A. Coleman, and H. Yang. 2016. 'SEIPIN Regulates Lipid Droplet Expansion and Adipocyte Development by Modulating the Activity of Glycerol-3-phosphate Acyltransferase', *Cell Rep*, 17: 1546-59.

Pan, X., P. Roberts, Y. Chen, E. Kvam, N. Shulga, K. Huang, S. Lemmon, and D. S. Goldfarb. 2000. 'Nucleus-vacuole junctions in Saccharomyces cerevisiae are formed through the direct interaction of Vac8p with Nvj1p', *Mol Biol Cell*, 11: 2445-57.

Paton, C. M., and J. M. Ntambi. 2009. 'Biochemical and physiological function of stearoyl-CoA desaturase', *Am J Physiol Endocrinol Metab*, 297: E28-37.

Piccolis, M., L. M. Bond, M. Kampmann, P. Pulimeno, C. Chitraju, C. B. K. Jayson, L. P. Vaites, S. Boland, Z. W. Lai, K. R. Gabriel, S. D. Elliott, J. A. Paulo, J. W. Harper, J. S. Weissman, T. C. Walther, and R. V. Farese, Jr. 2019. 'Probing the Global Cellular Responses to Lipotoxicity Caused by Saturated Fatty Acids', *Mol Cell*, 74: 32-44 e8.

Plotz, T., M. Hartmann, S. Lenzen, and M. Elsner. 2016. 'The role of lipid droplet formation in the protection of unsaturated fatty acids against palmitic acid induced lipotoxicity to rat insulin-producing cells', *Nutr Metab (Lond)*, 13: 16.

Pol, A., S. P. Gross, and R. G. Parton. 2014. 'Review: biogenesis of the multifunctional lipid droplet: lipids, proteins, and sites', *J Cell Biol*, 204: 635-46.

Prevost, C., M. E. Sharp, N. Kory, Q. Lin, G. A. Voth, R. V. Farese, Jr., and T. C. Walther. 2018. 'Mechanism and Determinants of Amphipathic Helix-Containing Protein Targeting to Lipid Droplets', *Dev Cell*, 44: 73-86 e4.

Puglielli, L., A. Rigotti, A. V. Greco, M. J. Santos, and F. Nervi. 1995. 'Sterol carrier protein-2 is involved in cholesterol transfer from the endoplasmic reticulum to the plasma membrane in human fibroblasts', *J Biol Chem*, 270: 18723-6.

Quehenberger, O., A. M. Armando, and E. A. Dennis. 2011. 'High sensitivity quantitative lipidomics analysis of fatty acids in biological samples by gas chromatography-mass spectrometry', *Biochim Biophys Acta*, 1811: 648-56.

Raiborg, C., E. M. Wenzel, and H. Stenmark. 2015. 'ER-endosome contact sites: molecular compositions and functions', *EMBO J*, 34: 1848-58.

Ralston, J. C., S. Matravadia, N. Gaudio, G. P. Holloway, and D. M. Mutch. 2015. 'Polyunsaturated fatty acid regulation of adipocyte FADS1 and FADS2 expression and function', *Obesity (Silver Spring)*, 23: 725-8.

Ralston, J. C., A. H. Metherel, K. D. Stark, and D. M. Mutch. 2016. 'SCD1 mediates the influence of exogenous saturated and monounsaturated fatty acids in adipocytes: Effects on cellular stress, inflammatory markers and fatty acid elongation', *J Nutr Biochem*, 27: 241-8.

Raychaudhuri, S., Y. J. Im, J. H. Hurley, and W. A. Prinz. 2006. 'Nonvesicular sterol movement from plasma membrane to ER requires oxysterol-binding protein-related proteins and phosphoinositides', *J Cell Biol*, 173: 107-19.

Rocha, N., C. Kuijl, R. van der Kant, L. Janssen, D. Houben, H. Janssen, W. Zwart, and J. Neefjes. 2009. 'Cholesterol sensor ORP1L contacts the ER protein VAP to control Rab7-RILP-p150 Glued and late endosome positioning', *J Cell Biol*, 185: 1209-25.

Saheki, Y., and P. De Camilli. 2017. 'Endoplasmic Reticulum-Plasma Membrane Contact Sites', *Annu Rev Biochem*, 86: 659-84.

Salo, V. T., I. Belevich, S. Li, L. Karhinen, H. Vihinen, C. Vigouroux, J. Magre, C. Thiele, M. Holtta-Vuori, E. Jokitalo, and E. Ikonen. 2016. 'Seipin regulates ER-lipid droplet contacts and cargo delivery', *EMBO J*, 35: 2699-716.

Salo, V. T., S. Li, H. Vihinen, M. Holtta-Vuori, A. Szkalisity, P. Horvath, I. Belevich, J. Peranen, C. Thiele, P. Somerharju, H. Zhao, A. Santinho, A. R. Thiam, E. Jokitalo, and E. Ikonen. 2019. 'Seipin Facilitates Triglyceride Flow to Lipid Droplet and Counteracts Droplet Ripening via Endoplasmic Reticulum Contact', *Dev Cell*, 50: 478-93 e9.

Schaffer, J. E. 2003. 'Lipotoxicity: when tissues overeat', *Curr Opin Lipidol*, 14: 281-7.

———. 2016. 'Lipotoxicity: Many Roads to Cell Dysfunction and Cell Death: Introduction to a Thematic Review Series', *J Lipid Res*, 57: 1327-8.

Schlame, M., S. Brody, and K. Y. Hostetler. 1993. 'Mitochondrial cardiolipin in diverse eukaryotes. Comparison of biosynthetic reactions and molecular acyl species', *Eur J Biochem*, 212: 727-35.

Schrauwen, P., V. Schrauwen-Hinderling, J. Hoeks, and M. K. Hesselink. 2010. 'Mitochondrial dysfunction and lipotoxicity', *Biochim Biophys Acta*, 1801: 266-71.

Segrest, J. P., M. K. Jones, H. De Loof, and N. Dashti. 2001. 'Structure of apolipoprotein B-100 in low density lipoproteins', *J Lipid Res*, 42: 1346-67.

Settembre, C., and A. Ballabio. 2014. 'Lysosome: regulator of lipid degradation pathways', *Trends Cell Biol*, 24: 743-50.

Settembre, C., R. Zoncu, D. L. Medina, F. Vetrini, S. Erdin, S. Erdin, T. Huynh, M. Ferron, G. Karsenty, M. C. Vellard, V. Facchinetti, D. M. Sabatini, and A. Ballabio. 2012. 'A lysosome-to-nucleus signalling mechanism senses and regulates the lysosome via mTOR and TFEB', *EMBO J*, 31: 1095-108.

Shen, Y., Z. Zhao, L. Zhang, L. Shi, S. Shahriar, R. B. Chan, G. Di Paolo, and W. Min. 2017. 'Metabolic activity induces membrane phase separation in endoplasmic reticulum', *Proc Natl Acad Sci U S A*, 114: 13394-99.

Shukla, A., P. Upadhyai, J. Shah, K. Neethukrishna, S. Bielas, and K. M. Girisha. 2017. 'Autosomal recessive spinocerebellar ataxia 20: Report of a new patient and review of literature', *Eur J Med Genet*, 60: 118-23.

Smith, S. 1994. 'The animal fatty acid synthase: one gene, one polypeptide, seven enzymes', *FASEB J*, 8: 1248-59.

Spigoni, V., F. Fantuzzi, A. Fontana, M. Cito, E. Derlindati, I. Zavaroni, M. Cnop, R. C. Bonadonna, and A. Dei Cas. 2017. 'Stearic acid at physiologic concentrations induces in vitro lipotoxicity in circulating angiogenic cells', *Atherosclerosis*, 265: 162-71.

Spitzer, J. J. 1973. 'CNS and fatty acid metabolism', *Physiologist*, 16: 55-68.

Suh, J. M., D. Stenesen, J. M. Peters, A. Inoue, A. Cade, and J. M. Graff. 2008. 'An RGS-containing sorting nexin controls *Drosophila* lifespan', *PLoS One*, 3: e2152.

Sui, X., H. Arlt, K. P. Brock, Z. W. Lai, F. DiMaio, D. S. Marks, M. Liao, R. V. Farese, Jr., and T. C. Walther. 2018. 'Cryo-electron microscopy structure of the lipid droplet-formation protein seipin', *J Cell Biol*, 217: 4080-91.

Szymanski, K. M., D. Binns, R. Bartz, N. V. Grishin, W. P. Li, A. K. Agarwal, A. Garg, R. G. Anderson, and J. M. Goodman. 2007. 'The lipodystrophy protein seipin is found at endoplasmic reticulum lipid droplet junctions and is important for droplet morphology', *Proc Natl Acad Sci U S A*, 104: 20890-5.

Teuling, E., S. Ahmed, E. Haasdijk, J. Demmers, M. O. Steinmetz, A. Akhmanova, D. Jaarsma, and C. C. Hoogenraad. 2007. 'Motor neuron disease-associated mutant vesicle-associated membrane protein-associated protein (VAP) B recruits wild-type VAPs into endoplasmic reticulum-derived tubular aggregates', *J Neurosci*, 27: 9801-15.

Thomas, A. C., H. Williams, N. Seto-Salvia, C. Bacchelli, D. Jenkins, M. O'Sullivan, K. Mengrelis, M. Ishida, L. Ocaka, E. Chanudet, C. James, F. Lescai, G. Anderson, D. Morrogh, M. Ryten, A. J. Duncan, Y. J. Pai, J. M. Saraiva, F. Ramos, B. Farren, D. Saunders, B. Vernay, P. Gissen, A. Straatmaan-Iwanowska, F. Baas, N. W. Wood, J. Hersheson, H. Houlden, J. Hurst, R. Scott, M. Bitner-Glindzicz, G. E. Moore, S. B. Sousa, and P. Stanier. 2014. 'Mutations in SNX14 cause a distinctive autosomal-recessive cerebellar ataxia and intellectual disability syndrome', *Am J Hum Genet*, 95: 611-21.

Tidhar, R., and A. H. Futerman. 2013. 'The complexity of sphingolipid biosynthesis in the endoplasmic reticulum', *Biochim Biophys Acta*, 1833: 2511-8.

Toulmay, A., and W. A. Prinz. 2012. 'A conserved membrane-binding domain targets proteins to organelle contact sites', *J Cell Sci*, 125: 49-58.

Turpin, S. M., G. I. Lancaster, I. Darby, M. A. Febbraio, and M. J. Watt. 2006. 'Apoptosis in skeletal muscle myotubes is induced by ceramides and is positively related to insulin resistance', *Am J Physiol Endocrinol Metab*, 291: E1341-50.

Ueno, S., Y. Maruki, M. Nakamura, Y. Tomemori, K. Kamae, H. Tanabe, Y. Yamashita, S. Matsuda, S. Kaneko, and A. Sano. 2001. 'The gene encoding a newly discovered protein, chorein, is mutated in chorea-acanthocytosis', *Nat Genet*, 28: 121-2.

Ugrankar, R., J. Bowerman, H. Hariri, M. Chandra, K. Chen, M. F. Bossanyi, S. Datta, S. Rogers, K. M. Eckert, G. Vale, A. Victoria, J. Fresquez, J. G. McDonald, S. Jean, B. M. Collins, and W. M. Henne. 2019. '*Drosophila* Snazarus Regulates a Lipid Droplet Population at Plasma Membrane-Droplet Contacts in Adipocytes', *Dev Cell*, 50: 557-72 e5.

Uto, Y., Y. Ueno, Y. Kiyotsuka, Y. Miyazawa, H. Kurata, T. Ogata, T. Takagi, S. Wakimoto, and J. Ohsumi. 2011. 'Discovery of novel SCD1 inhibitors: 5-alkyl-4,5-dihydro-3H-spiro[1,5-benzoxazepine-2,4'-piperidine] analogs', *Eur J Med Chem*, 46: 1892-6.

Vale, G., S. A. Martin, M. A. Mitsche, B. M. Thompson, K. M. Eckert, and J. G. McDonald. 2019. 'Three-phase liquid extraction: a simple and fast method for lipidomic workflows', *J Lipid Res*, 60: 694-706.

Vance, J. E. 2015. 'Phospholipid synthesis and transport in mammalian cells', *Traffic*, 16: 1-18.

Wakil, S. J., J. K. Stoops, and V. C. Joshi. 1983. 'Fatty acid synthesis and its regulation', *Annu Rev Biochem*, 52: 537-79.

Walter, P., and D. Ron. 2011. 'The unfolded protein response: from stress pathway to homeostatic regulation', *Science*, 334: 1081-6.

Walther, T. C., J. Chung, and R. V. Farese, Jr. 2017. 'Lipid Droplet Biogenesis', *Annu Rev Cell Dev Biol*, 33: 491-510.

Wang, H., M. Becuwe, B. E. Housden, C. Chitraju, A. J. Porras, M. M. Graham, X. N. Liu, A. R. Thiam, D. B. Savage, A. K. Agarwal, A. Garg, M. J. Olarte, Q. Lin, F. Frohlich, H. K. Hannibal-Bach, S. Upadhyayula, N. Perrimon, T. Kirchhausen, C. S. Ejsing, T. C. Walther, and R. V. Farese. 2016. 'Seipin is required for converting nascent to mature lipid droplets', *Elife*, 5.

Wang, L., A. R. Folsom, and J. H. Eckfeldt. 2003. 'Plasma fatty acid composition and incidence of coronary heart disease in middle aged adults: the Atherosclerosis Risk in Communities (ARIC) Study', *Nutr Metab Cardiovasc Dis*, 13: 256-66.

Weiss, S. B., E. P. Kennedy, and J. Y. Kiyasu. 1960. 'The enzymatic synthesis of triglycerides', *J Biol Chem*, 235: 40-4.

Wilfling, F., A. R. Thiam, M. J. Olarte, J. Wang, R. Beck, T. J. Gould, E. S. Allgeyer, F. Pincet, J. Bewersdorf, R. V. Farese, Jr., and T. C. Walther. 2014. 'Arf1/COPI machinery acts directly on lipid droplets and enables their connection to the ER for protein targeting', *Elife*, 3: e01607.

Wilfling, F., H. Wang, J. T. Haas, N. Krahmer, T. J. Gould, A. Uchida, J. X. Cheng, M. Graham, R. Christiano, F. Frohlich, X. Liu, K. K. Buhman, R. A. Coleman, J. Bewersdorf, R. V. Farese, Jr., and T. C. Walther. 2013. 'Triacylglycerol synthesis enzymes mediate lipid droplet growth by relocalizing from the ER to lipid droplets', *Dev Cell*, 24: 384-99.

Wright, M. M., and C. R. McMaster. 2002. 'PC and PE synthesis: mixed micellar analysis of the cholinephosphotransferase and ethanolaminephosphotransferase activities of human choline/ethanolamine phosphotransferase 1 (CEPT1)', *Lipids*, 37: 663-72.

Xiao, C., A. Giacca, A. Carpentier, and G. F. Lewis. 2006. 'Differential effects of monounsaturated, polyunsaturated and saturated fat ingestion on glucose-stimulated insulin secretion, sensitivity and clearance in overweight and obese, non-diabetic humans', *Diabetologia*, 49: 1371-9.

Xu, D., Y. Li, L. Wu, Y. Li, D. Zhao, J. Yu, T. Huang, C. Ferguson, R. G. Parton, H. Yang, and P. Li. 2018. 'Rab18 promotes lipid droplet (LD) growth by tethering the ER to LDs through SNARE and NRZ interactions', *J Cell Biol*, 217: 975-95.

Xu, N., S. O. Zhang, R. A. Cole, S. A. McKinney, F. Guo, J. T. Haas, S. Bobba, R. V. Farese, Jr., and H. Y. Mak. 2012. 'The FATP1-DGAT2 complex facilitates lipid droplet expansion at the ER-lipid droplet interface', *J Cell Biol*, 198: 895-911.

Yamanaka, T., and N. Nukina. 2018. 'ER Dynamics and Derangement in Neurological Diseases', *Front Neurosci*, 12: 91.

Yan, R., H. Qian, I. Lukmantara, M. Gao, X. Du, N. Yan, and H. Yang. 2018. 'Human SEIPIN Binds Anionic Phospholipids', *Dev Cell*, 47: 248-56 e4.

Ye, J., and R. A. DeBose-Boyd. 2011. 'Regulation of cholesterol and fatty acid synthesis', *Cold Spring Harb Perspect Biol*, 3.

Ye, R., T. Onodera, and P. E. Scherer. 2019. 'Lipotoxicity and beta Cell Maintenance in Obesity and Type 2 Diabetes', *J Endocr Soc*, 3: 617-31.

Zhao, K., and N. D. Ridgway. 2017. 'Oxysterol-Binding Protein-Related Protein 1L Regulates Cholesterol Egress from the Endo-Lysosomal System', *Cell Rep*, 19: 1807-18.

Zheng, B., T. Tang, N. Tang, K. Kudlicka, K. Ohtsubo, P. Ma, J. D. Marth, M. G. Farquhar, and E. Lehtonen. 2006. 'Essential role of RGS-PX1/sorting nexin 13 in mouse development and regulation of endocytosis dynamics', *Proc Natl Acad Sci U S A*, 103: 16776-81.

Zhu, X. G., S. Nicholson Puthenveedu, Y. Shen, K. La, C. Ozlu, T. Wang, D. Klompstra, Y. Gultekin, J. Chi, J. Fidelin, T. Peng, H. Molina, H. C. Hang, W. Min, and K. Birsoy. 2019. 'CHP1 Regulates Compartmentalized Glycerolipid Synthesis by Activating GPAT4', *Mol Cell*, 74: 45-58 e7.

Zilversmit, D. B. 1967. 'Formation and transport of chylomicrons', *Fed Proc*, 26: 1599-605.

Zimmermann, R., J. G. Strauss, G. Haemmerle, G. Schoiswohl, R. Birner-Gruenberger, M. Riederer, A. Lass, G. Neuberger, F. Eisenhaber, A. Hermetter, and R. Zechner. 2004. 'Fat mobilization in adipose tissue is promoted by adipose triglyceride lipase', *Science*, 306: 1383-6.